DISSERTATION

CLIMATE MODEL ERROR IN THE EVOLUTION OF SEA SURFACE TEMPERATURE PATTERNS AFFECTS RADIATION AND PRECIPITATION PROJECTIONS

Submitted by

Marc J. Alessi

Department of Atmospheric Science

In partial fulfillment of the requirements

For the Degree of Doctor of Philosophy

Colorado State University

Fort Collins, Colorado

Summer 2024

Doctoral Committee:

Advisor: Maria A. A. Rugenstein

Elizabeth A. Barnes
Eric D. Maloney
Megan D. Willis

ABSTRACT

CLIMATE MODEL ERROR IN THE EVOLUTION OF SEA SURFACE TEMPERATURE PATTERNS AFFECTS RADIATION AND PRECIPITATION PROJECTIONS

Atmosphere-ocean general circulation models (AOGCMs) are the primary tool climate scientists use in predicting the effects of climate change. While they have skill in reproducing global-mean temperature over the historical period, they struggle to replicate recently observed sea surface temperature (SST) trend patterns. In this dissertation, we quantify the impact of potential future model error in SST pattern trends on projections of global-mean temperature and Southwest U.S. (SWUS) precipitation. We primarily use a Green's function (GF) approach to identify which SST regions are most relevant for changes in these variables. Our findings demonstrate significant sensitivity of both global-mean temperature and SWUS precipitation to the pattern of sea surface warming, meaning that a continuation of AOGCM error in SST trend patterns adds uncertainty to climate projections which are currently not accounted for.

In Chapter 1, we quantify the relevance of future model error in SST to global-mean temperature projections through convolving a GF with physically plausible SST pattern scenarios that differ from the ones AOGCMs produce by themselves. We find that future model error in the pattern of SST has a significant impact on projections, such as increasing total model uncertainty by 40% in a high-emissions scenario by 2085. A reversal of the current cooling trend in the East Pacific over the next few decades could lead to a period of global-mean warming with a 60% higher rate than currently projected. These SST pattern scenarios work through a destabilization of the shortwave cloud feedback to affect temperature projections.

In Chapter 2, we focus on near-term projections of precipitation in the SWUS. The observed decrease in SWUS precipitation since the 1980s and heightened drought conditions since the 2000s have been linked to a cooling sea surface temperature (SST) trend in the Equatorial Pacific. Notably, climate models fail to reproduce this observed SST trend, and they may continue doing so in the future. In this chapter, we assess the sensitivity of SWUS precipitation projections to future SST trends using a GF approach. Our findings reveal that a slight redistribution of SST leads to a wetting or drying of the SWUS. A reversal of the observed cooling trend in the Central and East Pacific over the next few decades would lead to a period of wetting in the SWUS.

In Chapter 3, we analyze SWUS precipitation sensitivity to SST patterns on long timescales (7+ years) according to a GF approach and a convolutional neural network (CNN) approach. The GF and CNN identify different SST regions as having greater influence on SWUS precipitation: the GF highlights the Central Pacific known from theory to be relevant, while the CNN highlights the South-Central Pacific. To determine if the South-Central Pacific has a physically meaningful and so far overlooked influence on SWUS precipitation, rather than just a statistical relationship, we force an atmosphere-only climate model with an SST anomaly inspired by an Explainable Artificial Intelligence (XAI) method. We find that SSTs in the South-Central Pacific influence SWUS precipitation through an atmospheric bridge dynamical pathway, justifying the CNN's sensitivity physically.

The fact that we cannot fully trust the evolution of SST patterns in AOGCMs has many implications for the field of climate science and for how the world's governments and organizations respond to global warming. It is critical for climate change adaptation and mitigation assessments to consider this previously unaccounted for uncertainty in climate

projections. Climate scientists can do this by developing SST pattern storylines based on theory, observations, and our understanding of the ocean-atmosphere system. If we fail to communicate known uncertainties for both global-mean and regional projections, the world could lose faith in the climate science community, resulting in less of a global response to climate change.

ACKNOWLEDGEMENTS

From a young age, I knew I would study the Earth's weather and climate. I think this was obvious to my parents as well, since, at the age of 5, I laid out my very clear plan to become a tornado chaser. Of course, it didn't exactly work out that way, but here I am about to get a PhD in atmospheric science at the age of 28. So, I guess you could say I'm achieving my childhood dream? The *real* conclusion from this dissertation is that none of this would have been possible without the incredible people around me who have supported me, inspired me, taught me, and encouraged me to chase this dream. And so, while I'm the one that's getting "PhD" after my name, I would like to stress that these people are the reason for it (with no apology for the length):

First, I would like to acknowledge the unwavering support from my parents, Terri and David. In 1998, two years after I was born, my dad was diagnosed with a progressive neurological disease called spinocerebellar ataxia. By 2002, he had to quit his job and was restricted to a wheelchair. He later passed in 2011 when I was 15. Watching one of your parents/guardians fight for their life while trying their best to provide you with a normal childhood impacted me in more ways than I can list. But I will say this: my dad inspired me to work hard and to go after my dreams. My family was forced to face the mortality of life early, and I knew to channel that knowledge and everything I learned from my dad into my work, which eventually got me here to my dream of attaining a PhD. The truth is, I cannot imagine waking up every morning knowing your ability to do basic daily tasks is slowly being taken away from you, especially at such a young age. But my dad really, honestly never gave up. He showed up to every music recital, every swim meet, every award ceremony. He instilled in me a

passion for learning and reading books. He knew what was important in life. And I will admit, getting a PhD is hard work, but it's nothing like fighting for your life. In some ways, I feel a bit selfish: I wish my dad could see me write the letters PhD after our last name for the first time, and I wish he could see that I did in fact go after my dream. But in the end, what truly matters is that I am carrying his legacy with me every day. I know how to pick myself up after failing or making mistakes. I know how to decide what's important and what is worth fighting for. And I'm getting a PhD! Because of him. So that's awesome. Thanks dad.

It sounds like I'm giving my dad all the credit, but really my mom deserves even more. After all, who was raising three boys (yikes! (full disclosure though, I think I was pretty well behaved during my teenage years)), while also taking care of their disabled husband, while also working a full-time job because that was our family's only income, while also making sure there was a meal cooked and ready to eat every night, while also providing a normal childhood for my brothers and me? I feel like people always say something along the lines of, "eventually, children will grow up and learn that their parents aren't superhuman and without mistakes." But I still believe my mom is a superhuman. There is no sugar coating the fact that my mom has been dealt one of the worst decks of cards in history—just 8 years ago, 5 years after her husband died, my brother, Alex, was diagnosed with the same ataxia my father had. I often think about this and how it must feel for her. What is it like to care for your husband and then go through it all again with your youngest son? And yet, she wakes up every morning and deals with life the way it is. She is both the strongest and most selfless person I've ever met. She tells me to face every day anew. She tells me—and shows me—to never give up, and that no matter how hard things seem to get, we will deal with it. And isn't that so true? To hear someone speak those words who you know deserves the whole world instead of what they've been given. And through all of it, I think

my mom has an unparalleled understanding of life. When we laugh, it's fuller. When we cry, it feels real. We mourn, but we don't hold onto it in a way that doesn't allow us to live. So, thank you mom for all that you've done for me and all that you've taught me (and of course for all the care packages you sent me). This PhD is for you as much as it is for me!

I also want to thank my brothers, Michael and Alex, for their support during my PhD. Michael always keeps me on my toes in any political argument, but it's great for my debate skills if I ever run for public office. And I suppose you could say he also became a sort of role model? Can't believe I actually wrote that down—he probably won't read this. And Alex (of course it's no open secret that we've always been closer than with Michael), your strength and humor are such a light in my life. Like Dad, you've been dealing with ataxia but continue to focus on the good things in life. I will never laugh as hard with anyone else as I do with you; it's a bond only we share.

I want to recognize the amazing community that I was raised in. I know my extended family would support me through anything, and I'm thankful for the many good times we've spent together. Thank you especially to all my many mentors, teachers, and professors who have left an impact on my life. My master's advisors, Dr. Toby Ault and Dr. Art DeGaetano, saw my vision and pushed me to achieve it. I would also like to give a shoutout to Sue, a lifelong friend and mentor, who spent hours editing my application essays to undergrad and grad school, while also providing guidance and advice on navigating life.

I am so fortunate to have lifelong friends (I'm looking at you Batsquad and Bumsteers of Atmospheric Science) from my time at Cornell who continue to support me. Specifically, I would like to recognize Vindhya, Clay, Bud, and Vivian. I know I can count on these four

individuals whenever and wherever. I always look forward to phone calls with them to laugh, complain, brag, cry, etc. Life is so much better with them.

And finally: my time at CSU! Moving to a new state not knowing anyone in the middle of a pandemic was a sort of nightmare, but I got through it thanks to an incredible group of friends. Specifically, thank you to Daniel, Ann Casey, Emily, Madison, Bee, Charles, Allie, Charlie, Siânin, Ellie, and Nick. It is truly shocking they never got sick of me complaining about the extreme latent heat flux from my skin (the dew point depression and the wind speed here are too high for me) or complaining about the lack of Italian food and good pizza. Being in Colorado was hard for me; they knew of my family's situation and how much my heart hurt constantly for my brother. But they provided a space for me to thrive here. I will remember the wine nights, the karaoke nights, the ATS parties, the smiling faces at my orchestra concerts, the weekly lunches, the Horsetooth beach days, the star gazing, and much more for the rest of my life. I'll miss you guys!

The CSU Department of Atmospheric Science has incredible staff; mainly I'd like to thank Sarah, Nate, and Dinara for their help in navigating a PhD.

I want to thank my PhD committee, Dr. Elizabeth Barnes, Dr. Eric Maloney, and Dr. Megan Willis, for their time and helpful comments. They all serve as excellent role models as professors (+ more) I one day hope to be like.

The Rugenstein group has grown exponentially during my 4 years here; it feels like yesterday it was just Maria and me. I have them to thank for making sure my science makes sense outside of the ideas Maria and I come up with. Especially to Yiyu who dealt with hearing me complain about all my coding mistakes… so good luck and thanks to Yiyu, Leif, Dhyey, Killian, Olivia, and Senne!

And finally, I saved the most important acknowledgement for last: my advisor, Dr. Maria Rugenstein. These last four years were a true test of my willpower. There were *so many times* I considered giving up. But I didn't, and I can say with 99% confidence (which is a very high confidence for a meteorologist) that I'm finishing my PhD because of Maria. There is not another advisor out there that would have gotten me through a PhD. Like many in academia, Maria is an incredible scientist and mentor, but she is also one of the most *human* humans I know. From the beginning, I told her about my brother's terminal illness and how it would impact my PhD. Over the last four years, I spent months at home helping my mom with my brother. And Maria encouraged this: not once did she mention I was working remotely too much or push me harder than I could have handled. And the months I was in Colorado, it was no secret that I pursued many extracurriculars: music, leadership roles, unionizing, etc. Again, not once did Maria mention these in a negative way. She knew the importance of both pursuing hobbies and being there for your family while doing a PhD. And you know what? I think we still did some pretty amazing science! It took 4 years, but we got here. So, I have Maria to thank for making my dream a reality. I am forever grateful she emailed me on January 10th, 2020 to meet about this position, and I'm so proud to be her first PhD graduate. I will miss our weekly meetings, but I'm also excited to see what we'll do in the future. Thank you, Maria, for making me into the scientist I am today.

DEDICATION

This dissertation is dedicated to my mother, Teresa A. Alessi, whose perseverance, strength, love, and optimism inspire me each day.

TABLE OF CONTENTS

CHAPTER 1: INTRODUCTION

The overall goal of the Earth's climate system is simple: it must maintain energy equilibrium between incoming solar radiation and outgoing longwave radiation. For thousands of years, an energy equilibrium was preserved in the long-term (30+ years) trend, allowing for the growth of human civilization in a fairly stable climate. However, starting in the 1800s, human civilization began industrializing, leading to a surge in emissions of CO_2 and other greenhouse gases (GHG), disrupting this energy equilibrium. While the incoming solar radiation has remained mostly constant, the addition of GHGs to the Earth's atmosphere has lowered the outgoing longwave radiation, forcing the Earth's climate system to warm and again increase its outgoing longwave radiation to re-achieve equilibrium.

For decades, climate scientists have attempted to model this global-mean warming that follows an increase in atmospheric GHGs. In the 1970s, these general circulation models were relatively simple, only modeling the atmosphere with prescribed ocean, land, and ice surfaces (AGCMs; Manabe and Wetherald 1975). Over time, ocean models, land surface models, and ice models were coupled to the atmospheric model, producing the complex atmosphere-ocean general circulation models (AOGCMs) used by climate scientists today as their main tool in studying global warming. These AOGCMs have always confirmed that an increase in CO_2 leads to an increase in global-mean temperature, with models accurately replicating the observed global-mean warming since the 1850s. However, the response of the Earth on a regional scale to global warming is less clear among climate models. In fact, AOGCMs cannot replicate the observed pattern of sea surface temperature (SST) evolution (Seager et al. 2022; Olonscheck et al. 2020; L'Heureux et al. 2022; Wills et al. 2022). For example, the SST gradient between the East and West Pacific has strengthened in observations, while in AOGCMs the gradient weakens

(Wills et al. 2022). Interestingly, it is not clear what the cause of the discrepancy between models and observations is: some studies suggest AOGCMs are incorrectly simulating the response to anthropogenic emissions (Heede et al. 2020; Heede and Fedorov 2021; Seager et al. 2019), while others claim models are misrepresenting the true range of the internal variability of the climate system (Olonscheck et al. 2020; Watanabe et al. 2021). Nevertheless, the fact that AOGCMs cannot replicate the observed SST trend pattern remains a major problem for climate scientists.

If AOGCMs are correctly reproducing the global-mean warming, why would we need to worry about climate models' replicability of the observed SST pattern? Previously, climate scientists assumed that the relationship between global-mean warming and an increase in atmospheric CO_2 was linear, i.e., a quadrupling of CO_2 would lead to double the global-mean warming following a doubling of CO_2. This linearity is reflected in the *constant* global-mean climate feedback parameter ($\lambda = \partial R/\partial T$); the planet must warm a certain amount (∂T) in response to a forcing applied to the climate system (∂R) such as an increase in atmospheric CO_2. In recent years, it has been established that the evolution of the SST pattern can influence λ (Dong et al. 2019; Stevens et al. 2016), meaning that λ is in reality *nonconstant*, demonstrating a nonlinearity of the climate system in which the amount of global warming is sensitive to the pattern of SST evolution. In fact, given that AOGCMs cannot replicate the observed SST pattern trend, they also fail to replicate λ over the historical period (Andrews et al. 2022, 2018). As proof that the SST trend pattern is responsible for this mismatch between the observed and modeled λ, scientists demonstrated that forcing an AGCM with the observed SST pattern reproduces the observed λ. In other words, if AOGCMs were able to correctly simulate the SST trend pattern, they would also correctly predict λ. Because AOGCMs cannot predict λ, they may also struggle to reproduce global-mean warming (see Chapter 1). This may not show in recent historical trends

of global-mean temperature due to changes in the global ocean heat uptake, though this area of research is new and still under investigation (Newsom et al. 2020; Andrews et al. 2022).

The inability of AGOCMs to reproduce the observed SST trend pattern also inhibits AOGCM skill in reproducing regional observed trends in other variables, not just global-mean λ. For example, it is well established that the pattern of SST in the Tropical Pacific is a driver of changes in Southwest U.S. (SWUS) precipitation. Since AOGCMs erroneously simulate the SST pattern evolution in the Tropical Pacific, they also fail to simulate SWUS precipitation trends. For example, since the beginning of the 21st century, a severe, multi-decadal drought event is ongoing in the SWUS (Williams et al. 2022) that is unpredicted by AOGCM projections of SWUS hydroclimate (Lehner et al. 2018). Likely the drought is caused by both the observed SST trend and its effect on SWUS precipitation and anthropogenic climate change, which leads to increased evaporative demand as the global-mean temperature increases (Diffenbaugh et al. 2015). However, since it is not clear what is causing the observed SST trend in the Tropical Pacific (Wills et al. 2022), it remains possible the drought is mostly caused by anthropogenic climate change if the observed SST trend is in fact a response to anthropogenic forcing (Heede and Fedorov 2021). Nevertheless, the cooling trend in the Central and East Pacific unpredicted by AOGCMs is contributing to the SWUS drought. Delworth et al. (2015) found that AOGCMs could replicate the observed SWUS hydroclimate trend when the East Pacific was forced with a cooling SST trend, one that matches the observed cooling trend, induced by adjusting the local wind stress. This drying of the SWUS from a cooler East Pacific corroborates our current understanding of the teleconnection between precipitation and SST in these two regions (e.g., Evans et al. 2022; Redmond and Koch 1991).

It remains possible that there are additional SST regions that drive SWUS precipitation. In recent decades, the correlation between the Central and East Pacific SST and SWUS precipitation has weakened on decadal timescales (Mamalakis et al. 2018). But why? If climate scientists are to make predictions of long-term trends (7+ years) in precipitation from the pattern of SST, we must first fully understand SWUS precipitation sensitivity to SST. Mamalakis et al. (2018) found a new teleconnection between SSTs off the coast of New Zealand and SWUS precipitation through a correlation analysis. Other recent students continue to highlight the importance of the Central and East Pacific (Hu et al. 2021). The problem is then two-fold: AOGCMs currently struggle to reproduce observed SST trend patterns, yes, but even if AOGCMs reproduced the observed SST trend, they may struggle to reproduce SWUS precipitation trends on long timescales, given the potential existence of SST teleconnections to SWUS precipitation that are not well understood or identified.

In this dissertation, we study the impact of potential, future model error in the evolution of the SST pattern on global-mean temperature and SWUS precipitation projections. AOGCMs fail to reproduce the observed SST trend, and they may continue doing so in the future. Given that λ, and therefore global-mean temperature, depend on the pattern of SST, any change in the observed SST pattern could affect the rate of global warming. In Chapter 2, we develop physically plausible SST scenarios that account for future model error in SST trends and find a significant impact of the SST pattern on temperature projections. In fact, if the East Pacific cooling trend reverses, which may have already started (Rugenstein et al. 2023; Andrews et al. 2022), a global-mean warming rate 60% higher than current projections will be observed. In Chapter 3, we apply these same SST scenarios to SWUS precipitation projections. We find that a reversal of the East and Central Pacific cooling trend will result in a wetting of the SWUS over

the next few decades. Finally, in Chapter 4, we further study the sensitivity of SWUS precipitation to the pattern of SST on long timescales (>7+ years). Through a convolutional neural network approach, we identify a new SST region, the South-Central Pacific, that influences SWUS precipitation.

CHAPTER 2: SURFACE TEMPERATURE PATTERN SCENARIOS SUGGEST HIGHER WARMING RATES THAN CURRENT PROJECTIONS[1]

2.1 Introduction

2.1.1 SST Pattern Uncertainty

In the face of anthropogenic climate change, global economic, political, and jurisdictional decision making relies on projections from fully-coupled atmosphere-ocean general circulation models (AOGCMs). Total model uncertainty of these projections originates in the forcing scenario, internal variability of the climate system, and structural differences between models (Eyring et al. 2016; Hawkins and Sutton 2009; Lehner et al. 2020; Maher et al. 2019; Zelinka et al. 2020). However, AOGCMs and their current range of total model uncertainty fail to replicate observed SST trend patterns, for example in the Southern Ocean and in the Equatorial Pacific (L'Heureux et al. 2022; Olonscheck et al. 2020; Seager et al. 2019, 2022; Wills et al. 2022), resulting in the erroneously simulated weakening of the Walker circulation (Chemke and Polvani 2019; Chung et al. 2019; Kociuba and Power 2015; Ma and Zhou 2016; Plesca et al. 2018). It is likely that AOGCMs also incorrectly simulate the SST pattern after a volcanic eruption (Gregory et al. 2020). The inability of AOGCMs to reproduce the observed warming trends could be due to an underestimation of the true range of internal variability by AOGCMs or due to *forcing response biases. Forcing response biases* may be caused by mean-state (climatological) biases, input forcing errors, or an erroneous representation of processes, e.g., coupling of the land and atmosphere. It is generally unknown how these *forcing response biases* are related within and

[1] Alessi, M. J., & Rugenstein, M. A. A. (2023). Surface temperature pattern scenarios suggest higher warming rates than current projections. *Geophysical Research Letters*, 50, e2023GL105795. https://doi.org/10.1029/2023GL105795

across models (Heede and Fedorov 2021; Huang and Ying 2015; Huber and Knutti 2014; Kajtar et al. 2021; Seager et al. 2019; Wang et al. 2014, 2017). We expect these *forcing response biases* and/or the possible underestimation of the true range of internal variability by AOGCMs to persist into the near future and define this uncertainty as *SST pattern uncertainty* (see Text A.1.1 for definitions). It is critical to separate the impact of *SST pattern uncertainty* on global-mean temperature projections from that of the classical uncertainties, since total model uncertainty as it was simulated over the last few decades did not include the observed SST trend pattern in large regions (Figure A.2.1; e.g., Wills et al. 2022).

Here, we assess the implications of *SST pattern uncertainty* on climate change projections. SST patterns are critical for calculating the Earth's radiation budget (Dong et al. 2019; Zhou et al. 2021, 2017) and their relevance for projections has been discussed qualitatively (e.g., Andrews et al. 2022; Dong et al. 2022; Frey et al. 2017; Watanabe et al. 2021; Zhou et al. 2021). However, *SST pattern uncertainty* has not been quantified since we do not know the SST pattern of the future. To circumvent this problem, we convolve Green's functions with "reasonable" SST pattern scenarios that differ from the ones AOGCMs produce by themselves (Section 2). We find that accounting for *SST pattern uncertainty* in projections increases the range of possible future global warming scenarios by the end of the century (Section 3.1). However, if our model is forced with temperature patterns starting from the currently observed SST pattern, global warming is more constrained than the standard projections (Section 3.2). We show that global warming rates are substantially higher than the ones projected by the standard AOGCM if the East Pacific and Southern Ocean switch from their current cooling trends to warming trends. *SST pattern uncertainty* must be considered in future climate projections if

AOGCMs simulate SST trend patterns as poorly in the future as they do over the historical period.

2.1.2 The Pattern Effect

We show that *SST pattern uncertainty* has a significant impact on temperature projections through the pattern effect, which states that the evolution of the spatial structure of surface warming affects the global-mean radiative feedback parameter (λ) (Murphy 1995; Stevens et al. 2016). For example, if the equatorial West Pacific warms, atmospheric deep convection strengthens, warming the tropical free troposphere which increases outgoing longwave radiation (OLR) at the top of the atmosphere (TOA) and strengthens the inversion above the tropical and subtropical East Pacific, which can increase coverage of the marine stratocumulus cloud deck (MSCD) that reflects sunlight (e.g., Andrews and Webb 2018; Ceppi et al. 2017; Dong et al. 2019; Zhou et al. 2017). These processes lead to a more negative λ; if a perturbation is applied to Earth's energy balance, the planet achieves re-equilibrium with a smaller change in global-mean temperature than a climate system with a less negative λ. In the Southern Ocean, a decrease in the MSCD due to a delayed warming of the Southern Ocean incites a more positive λ over time through changing SST and feedbacks in the tropical Pacific basin (e.g., Kim et al. 2022; Lin et al. 2021; Rugenstein et al. 2016; Senior and Mitchell 2000).

Over the last three decades, areas of atmospheric deep convection and more stabilizing feedbacks, such as in the equatorial West Pacific, warmed more than areas of destabilizing feedbacks, especially the subtropics, leading to a more stabilizing λ (Andrews et al. 2018, 2022; Fueglistaler and Silvers 2021; Seager et al. 2019). Weak warming or even cooling in the Southern Ocean, due partially to upwelling of deep water unaffected by climate change, may have also stabilized λ (Armour et al. 2013; Senior and Mitchell 2000). AOGCM simulations of

realistic historical forcing failed to reproduce this observed SST trend pattern that strongly influences λ through the pattern effect. Recent research on the evolution of the observed TOA radiative imbalance suggests that AOGCMs might underestimate the strength of the pattern effect (Ceppi et al. 2017; Loeb et al. 2021). *SST pattern uncertainty* will most likely work through the pattern effect to influence λ and global-mean temperature in projections of near- and long-term climate change.

2.2 Methods: Energy Balance and a Green's Function Approach

To analyze how model deficiencies in SST patterns impact climate change projections, we use the zero-order energy balance model (Armour 2017; Gregory et al. 2002, 2004; Zhou et al. 2021):

$$\Delta T = \frac{N - F}{\lambda}, \qquad (1)$$

where ΔT is the change in global-mean temperature from preindustrial control, N is the global-mean net TOA radiative imbalance relative to a preindustrial control climate, F is the global-mean radiative forcing, and λ is the global-mean radiative feedback parameter. Assessing a future ΔT is not a trivial problem, since N, F, and λ are unknown and we currently rely on AOGCMs to simulate them correctly. We posit that, since AOGCMs did not reproduce λ (and in some occasions ΔT and N) correctly over the last few decades, they also may not do so in projections.

To circumvent the AOGCM shortcomings in creating credible SST patterns, we use a Green's function (GF) approach of calculating the TOA radiation and surface temperature responses with constructed, physically plausible SST patterns (Barsugli and Sardeshmukh 2002; Dong et al. 2019; Zhou et al. 2017). A GF allows us to account for model deficiencies systematically and comprehensively by calculating the response of any atmospheric global

circulation model (AGCM) variable, such as near-surface temperature or TOA radiation, to any SST pattern. This assumes that given the correct SST pattern, an AGCM represents that variable reasonably well compared to observations, which is true for TOA radiative fluxes on interannual timescales (Loeb et al., 2020). We develop and verify a radiative response GF (GF_R) and surface temperature response GF (GF_T) from SST patch perturbations in the Max Planck Institute's (MPI) atmosphere-only model ECHAM6 (see Text A.1.2 and Figure A.2.2). Dividing GF_R by GF_T results in λ (Figure 2.1), which shows that some regions stabilize and others destabilize the global-mean λ. While we only use one GF developed from one AGCM in this study, the general pattern of λ is similar across models (Dong et al. 2019; Zhang et al. 2023; Zhou et al. 2017).

We calculate F by running an ECHAM6 simulation with constant preindustrial average (1850-1870) SST and sea ice concentration with time-dependent atmospheric and land forcings from historical and Representative Concentration Pathway (RCP) 8.5 simulations (Pincus et al. 2016). N is taken from the MPI-ESM grand ensemble output for each ensemble member for historical and RCP8.5 (N_{RCP}; Maher et al., 2019). We solve for ΔT with a variation of Eq. (1):

$$\lambda = \frac{\mathrm{GF_R} * \mathrm{SST_{pattern}}}{\mathrm{GF_T} * \mathrm{SST_{pattern}}} = \frac{N_{RCP} - F}{\Delta T}, \qquad (2)$$

where $\mathrm{GF_X} * \mathrm{SST_{pattern}}$ denotes an SST pattern convolved with a given GF (see Text A.1.3).

We use SST output from the 100-member initial condition MPI Grand Ensemble (MPI-GE; Maher et al., 2019) following the historical period, RCP8.5, and RCP4.5 (van Vuuren et al. 2011). The large ensemble allows us to compare the relevance of *SST pattern uncertainty* to uncertainty due to internal variability. We calculate the global- and annual-mean response of GF_R, GF_T, and λ to three types of SST patterns: observed SST from the past, simulated SST from AOGCMs in the past and future, and constructed SST scenarios for the future. We first explain the construction and impact of idealized SST pattern scenarios (Section 3.1) before we construct

and discuss the impact of "realistic" scenarios starting from the currently observed SST pattern (Section 3.2).

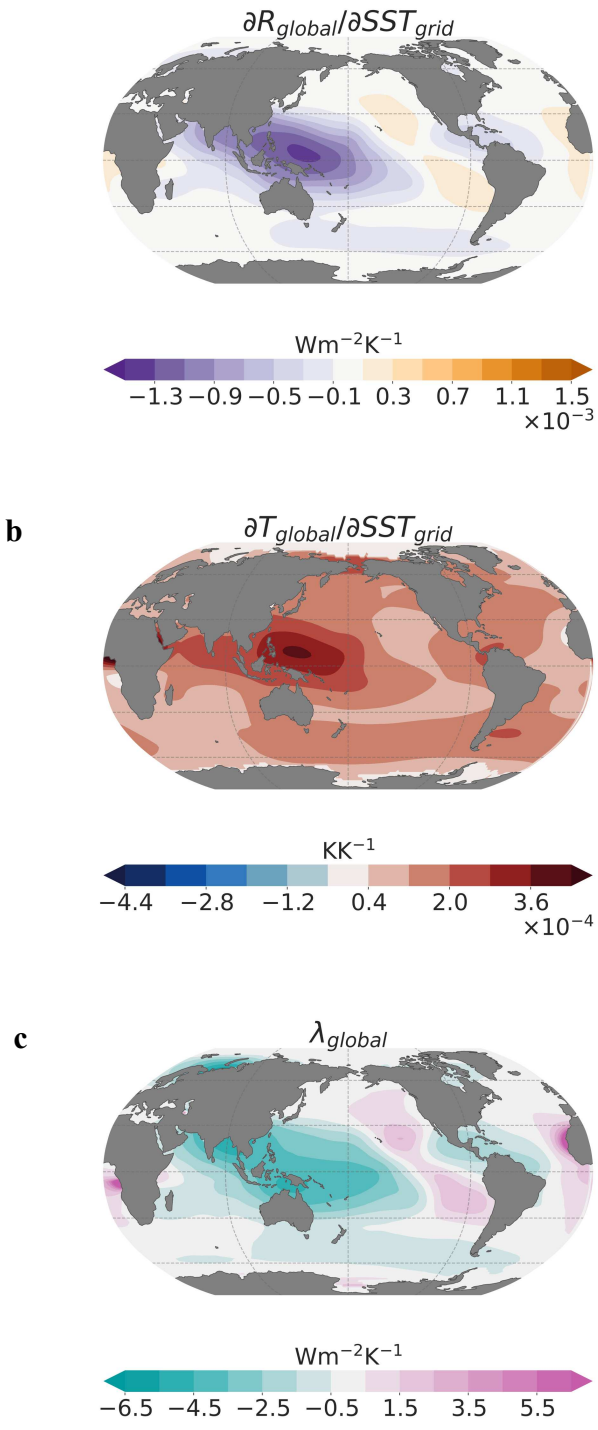

Figure 2.1. Global- and annual-mean top-of-atmosphere radiative response (**a**), temperature response (**b**), and radiative feedback (**c**) per unit SST warming in each grid box.

2.3 Results

2.3.1 Adjusting SST Patterns Based on Known AOGCM Deficiencies

The scenarios are inspired by *SST pattern uncertainty* in three regions (Table A.3.1). We analyze six idealized scenarios to assess the sensitivity of ΔT to changes in SST in these regions: a cooler and warmer WP (WP_{cool}, WP_{warm}), a cooler and warmer East Pacific (EP_{cool}, EP_{warm}), and a cooler and warmer SO (SO_{cool}, SO_{warm}) than the RCP8.5 projections (see additional details and sensitivity tests in Text A.1.4). In each region, an equally large SST area is warmed and cooled by 3% of the global-mean SST anomaly (ΔSST) in RCP8.5 compared to the pre-industrial control simulation for each year (on the order of 1.1K by 2085), while keeping ΔSST the same. Thus, the rest of the SST around the globe, outside the box of interest, is adjusted uniformly by area weight (on the order of 0.01K at each grid point by 2085). Note that the warming rate in a "cool" scenario is somewhat colder in the region of interest than the RCP reference but still warming with respect to present day values (global mean warming remains unchanged). We selected 3% of ΔSST since it is a similar magnitude as historical *SST pattern uncertainty* (e.g., Seager et al. 2022; Wills et al. 2022). Keeping ΔSST constant allows us to use the AOGCM N_{RCP} in Eq. (1), in the assumption that N_{RCP} predominantly depends on global mean warming and not the pattern of SST (Flynn and Mauritsen 2020; Gregory et al. 2015; Kuhlbrodt and Gregory 2012), which is currently debated and under investigation (Andrews et al. 2022; Newsom et al. 2020; see Text A.1.5 and Figure A.2.3). In summary, our rather conservative assumption is that the coupled MPI-GE is correctly simulating ΔSST and N_{RCP}, but it does not warm in the right places. This is similar to the recent past, in which the MPI-ESM AOGCM correctly simulates global-mean temperature trends, but not the warming pattern.

We find that these modest redistributions of SST are enough to change ΔT (Figure 2.2a), since λ is affected (Figure 2.2b). As expected, changes in SST in the equatorial West Pacific elicit the strongest response in λ (Dong et al., 2019), and hence ΔT (Figure 2.1). A warming of the equatorial West Pacific (WP_{warm}) results in the planet warming 0.5 K less by 2085 than the ΔT of the AOGCM ensemble-mean of the standard RCP8.5 scenario. This highlights the importance of the pattern effect for even small adjustments in the SST pattern that are on the same order of magnitude as historical *SST pattern uncertainty*. For WP_{cool}, the planet warms more because, by construction of the scenario, a cooler WP leads to a less negative and more destabilizing λ. For the tropical East Pacific, any ΔT response to a warming or cooling is weak because it is capped by the strong lower tropospheric inversion. A warmer EP of notably the same area and perturbation magnitude as WP_{warm} increases solar absorption due to a reduced MSCD from a weaker inversion (Text A.1.6 and Figure A.2.4), warming the planet more. The response of a warming and cooling in the Southern Ocean is similar to the East Pacific though more muted (Figure 2.2a). We highlight that these changes are dominated by the local and remote impact of the temperature perturbation in these three boxes and not by the response to the redistributed temperature elsewhere.

Importantly, warming in the equatorial West Pacific affects λ nearly 50% more than the same amount of warming in the tropical East Pacific (Figure A.2.4b). The more stabilizing radiative response to the equatorial West Pacific stems from a greater increase in the East Pacific MSCD (increased reflected radiation) than the same amount of warming in the tropical East Pacific would have locally on decreasing the MSCD (decreased reflection). In the Southern Ocean, a more positive lapse rate feedback is balanced by a more negative water vapor feedback,

with changes in clouds driving a more positive feedback through a weakened MSCD (Senior and Mitchell, 2000).

The range of internal variability, defined as two standard deviations of the MPI-ESM RCP8.5 grand ensemble after ΔT is calculated, is 1.1K in 2085 (Figure 2.2a). This uncertainty due to internal variability increases to 2.0K for RCP8.5 when also considering *SST pattern uncertainty* for the West Pacific scenarios ($WP_{cooling}$ and $WP_{warming}$) solely due to a redistribution of the SST. This corresponds to an 80% increase in uncertainty compared to the MPI-GE internal variability. However, *SST pattern uncertainty* does not just affect temperature projections from the MPI model; discrepancies between modeled and observed SST trend patterns exist across all models (Seager et al. 2022; Wills et al. 2022). The Coupled Model Intercomparison Project Phase 5 (CMIP5) total uncertainty spread for all models (structural uncertainty) and their ensemble members (uncertainty due to internal variability) for RCP8.5 is 2.3 K (2.2 K to 4.5 K) in 2085 (IPCC, 2014). Assuming MPI-ESM is representative of other models, we can apply the 0.9 K increase in uncertainty from *SST pattern uncertainty* to each model's ensemble. This increases total model uncertainty from 2.3 K to 3.4 K, which is a 40% increase in total model uncertainty considering two possible future scenarios (WP_{cool} and WP_{warm}). However, given that models have structural differences, *SST pattern uncertainty* may emerge differently across models, increasing or decreasing the effect on total model uncertainty.

Applying the same perturbations to RCP4.5 again widens the uncertainty through the end of our projections and hence extends the overlap between the RCP8.5 and RCP4.5 scenarios. In other words, if the world releases emissions akin to the RCP8.5 scenario, RCP4.5-like temperatures are possible for a longer time solely due to *SST pattern uncertainty* and the pattern effect. For example, the last overlap of internal variability for the RCP8.5 and RCP4.5 ensemble

members occurs before 2070, but with *SST pattern uncertainty* this shifts 15 years later (stars in Figure 2.2a).

It is unlikely that one region warms or cools in a linear manner (which would constitute a constant *forcing response bias* or a constant underestimation of the true range of internal variability in time) and that only one region experiences these response biases as illustrated here. Combinations of these idealized scenarios represent more plausible "storylines" of future climate states further discussed in the next section (Shepherd et al. 2018; Stevens et al. 2016). The net effect from *SST pattern uncertainty* could therefore be more or less significant than the 40% increase in total model uncertainty discussed above depending on how different actual SST trend patterns are from the simulated ones. For example, in the most extreme warming case, if WP_{cool}, SO_{warm}, and EP_{warm} coexist in 2085 with RCP8.5 forcing, MPI-GE uncertainty could increase by 1.3K instead of 0.9K. However, the opposite could also happen: if WP_{warm}, SO_{cool}, and EP_{cool} combined under RCP4.5 forcing, ΔT would be less than the purple shaded region of RCP4.5 (Figure 2.2a). In this case, the globe would warm 1K less than the RCP4.5 ensemble-mean by 2085, which is outside of the scope of uncertainty from internal variability for RCP4.5. The effects of *SST pattern uncertainty* could also cancel out itself: a stagnant or slightly warmer WP and significantly warmer EP than RCP8.5 projections would combine to have no effect on total model uncertainty by 2085. Furthermore, depending on internal variability and a combination of scenarios, ΔT could shift anywhere between the new tails of RCP8.5.

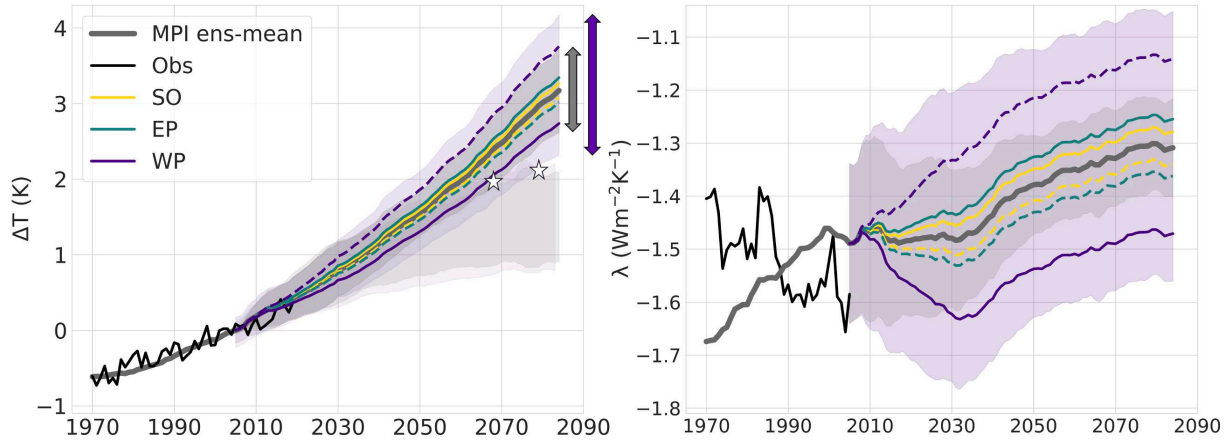

Figure 2.2. **a**, Global-mean surface temperature anomaly (ΔT) from the 2000-2010 average: HADCRUT5 observations (black), MPI-ESM historical (1970-2006) and RCP8.5 projection (2006-2085) ensemble-mean (dark gray), MPI-ESM RCP8.5 ensemble spread (+/- 2σ; top gray shading), WP_{cool} scenario (dashed purple), EP_{cool} scenario (dashed teal), SO_{cool} scenario (dashed gold), equivalent warming scenarios (same colors, solid lines), and associated model spread WP_{cool} and WP_{warm} when applied to each RCP8.5 ensemble member (top purple shading). The arrows represent the ensemble-mean spread of ΔT in 2085 without (gray, $1.1K$) and with (purple, $2.0K$) *SST pattern uncertainty* of the scenarios explored here. The MPI-ESM RCP4.5 ensemble spread (bottom gray shading) and spread of WP_{cool} and WP_{warm} when applied to each RCP4.5 ensemble member (bottom purple shading). The stars denote the last crossover year of RCP8.5 and RCP4.5 for internal variability without *SST pattern uncertainty* (left star; gray shadings) and for internal variability plus WP_{cool} and WP_{warm} (right star; purple shadings). **b**, Time series of the radiative feedback parameter (λ) with colors of lines and shading corresponding to those in (**a**) for RCP8.5, except the ensemble spread is +/- 1σ for visual clarity. λ based on observed SST patterns (black) ends in 2006 since it is calculated with a 30-year sliding linear regression of GF_R on GF_T (see Figure A.2.7).

2.3.2 Adjusted SST Patterns Based on Recent Observations

In a more realistic scenario, we discard the RCP projection as reference and start from the SST pattern observed over the recent decades. Given that there is already a discrepancy between observed and simulated SST trends (e.g., Seager et al. 2022; Wills et al. 2022), we suggest SST pattern scenarios that could play out as the real-world SST pattern evolves from where it is currently. While *SST pattern uncertainty* increases total model uncertainty (see above), we here *constrain* future projections to be consistent with both the currently observed SST pattern and theory. For example, the East Pacific is likely to warm in the future as GHG forcing continues to

increase and aerosol forcing decreases (Andrews et al. 2022; Intergovernmental Panel on Climate Change (IPCC) 2023; Andrews et al. 2015; Dong et al. 2020; Heede and Fedorov 2021; Heede et al. 2020; Hu et al. 2022; Lin et al. 2021; Park et al. 2022). If the East Pacific warmed faster than the SST in other regions, λ would destabilize compared to today (Figure 2.1), causing ΔT to increase more rapidly. To reproduce this effect, we interpolate the SST at each grid point from HadISST 2021 observations (Figure 2.3a) to the average SST pattern in the RCP8.5 ensemble members for 2031 and 2071 (Figure 2.3b). Our assumption now relaxes to trusting the far-future but not the current and near-future SST pattern from RCP8.5. The interpolation between observations and RCP8.5 includes a strong warming of MSCD regions, especially the tropical East Pacific and the Southern Ocean, both of which outpace the equatorial West Pacific (Figure 2.3c). These trends are opposite to those of the recent observational period (Figure 2.3d). We choose two "transition periods" as examples, one ten years in length (2021-2031; $\text{Transition}_{10\text{yr}}$) and the other fifty years in length (2021-2071; $\text{Transition}_{50\text{yr}}$), since it is unknown how quickly or when the East Pacific may warm (Table A.3.1; see Text A.1.7) (Andrews et al. 2015; Heede and Fedorov 2021; Heede et al. 2020; Kohyama et al. 2017).

λ becomes less negative rapidly for both transition period lengths as the observed SST pattern approaches the RCP8.5 ensemble-mean SST pattern, implying a very high warming rate during the transition periods (Figure 2.3e). This is because warming is focused in areas that lead to a less negative λ (Figure 2.1c), notably the Southeast and Northeast Pacific. In fact, $\lambda_{transition}$ overshoots $\lambda_{RCP8.5}$ for a period due to the intense warming in regions with a small negative or positive λ. The transition scenarios are dominated by less negative shortwave cloud, lapse rate, and Planck feedbacks (Figure A.2.4d) compared to current observations (Figure A.2.4c), partially due to a decrease in the extent of the MSCD in both regions. By 2030, ΔT of

Transition$_{10yr}$ is nearly 0.2K warmer than the RCP8.5 ensemble-mean ΔT. For Transition$_{50yr}$, ΔT remains nearly 0.3K warmer than the RCP8.5 ensemble-mean ΔT from 2030 through the end of the transition period in 2071. Furthermore, the planet experiences a rapid rate of warming under the transition scenarios given the heightened warming in the East Pacific. We calculate the global-mean warming rate for all 20-year segments from 2015-2044 for all ensemble members. The mean warming rate increases from 0.033 K/20yr (+/- 0.022 K/20yr) in RCP8.5 to 0.052 K/20yr (+/- 0.009 K/20yr) in Transition$_{50yr}$, meaning that the world could experience a warming rate 58% greater than that currently simulated by MPI-GE internal variability (Figure 2.3e, inset or Figure A.2.5). In Transition$_{50yr}$, the range of possible warming rates narrows significantly and shifts to the high end of what was predicted by the MPI-GE without *SST pattern uncertainty*. If the SST pattern were to reverse the recent cooling trends in the EP and SO, we may for several decades experience a warmer world and higher warming rates than suggested by AOGCM projections.

We apply two more scenarios, both assuming AOGCM SST projections from the RCP8.5 ensemble-mean are either partly or fully incorrect. The first scenario assumes observed SST approaches the RCP8.5 ensemble-mean, as the transition scenarios do, but the EP instead follows the 1991-2021 observed cooling SST trend until the end of the century (Transition$_{50yr\text{-}EPobs}$). While the rest of the world converges to the SST pattern in Figure 2.3d, we assume AOGCMs continue to erroneously simulate the tropical East Pacific, meaning the region will, counter to what AOGCMs project, continue to cool as in Figure 2.3f. With Transition$_{50yr\text{-}EPobs}$, λ is more negative than the earlier scenarios (Figure 2.3a), demonstrating the impact a cooling vs. warming EP would have on a potential real-world scenario. The difference between the solid red line (Transition$_{50yr}$) and dashed red line (Transition$_{50yr\text{-}EPobs}$) in Figure 2.3 is solely the influence of

the EP cooling rather than the EP warming. The second scenario extrapolates the 30-year observed trend from 1991-2021 forward in time everywhere. We here relax our assumptions further in that AOGCM SST patterns are not to be trusted at any future time. A constant λ of -1.7 $Wm^{-2}K^{-1}$ results from this extrapolation, since there is no change in the SST warming pattern, which begets a warming rate similar to the one observed in recent decades. By 2085, ΔT is slightly below 2.0K (Figure 2.3a), almost 1.5K lower than the RCP8.5 ensemble-mean in 2085. For this scenario, we use $N_{1991-2021} - F_{1991-2021}$ in calculating ΔT.

We conclude that in the near-future, *SST pattern uncertainty* is as relevant for projections as the three classical forms of uncertainty. It remains to be explored how much of the *SST pattern uncertainty* is due to internal variability, forcing uncertainty, or structural uncertainty.

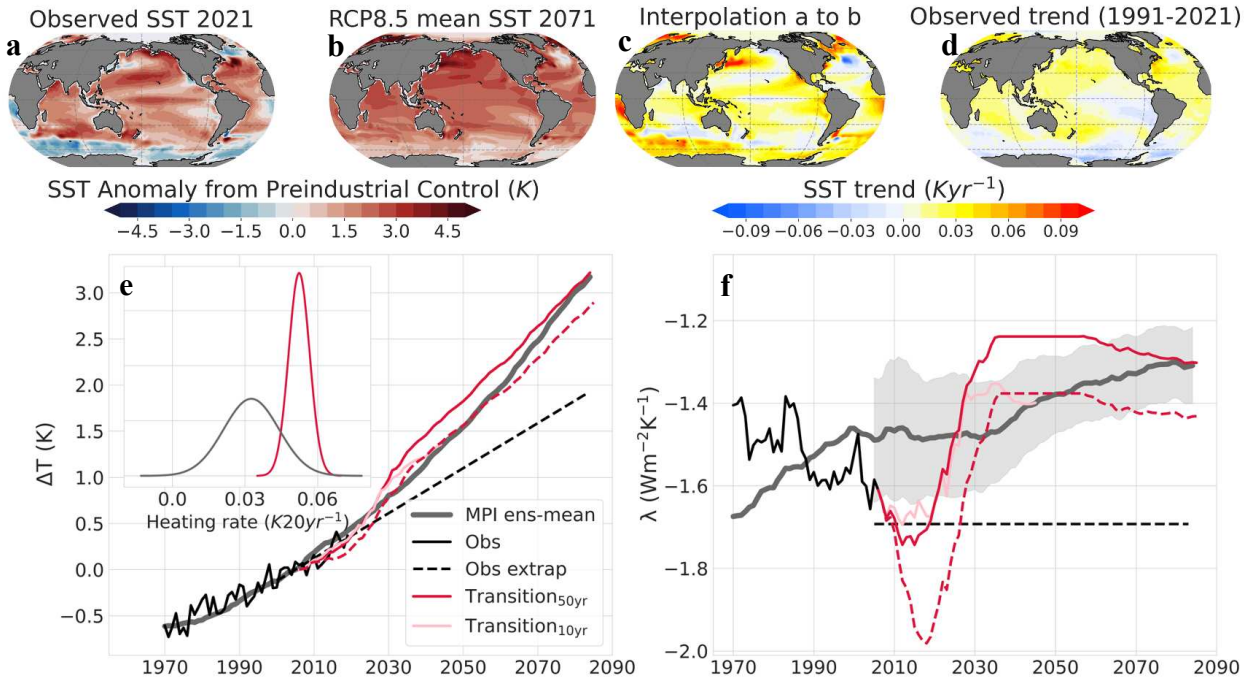

Figure 2.3. **a**, 2016-2021 HadISST observed SST pattern anomaly from the MPI-ESM preindustrial control (1850-1870) average (1st year of transition period). **b**, 2071-2076 MPI-ESM RCP8.5 ensemble-mean SST pattern anomaly from preindustrial control average (last year of transition period). **c**, The 50-year interpolated SST trend from **a** to **b**. **d**, The HadISST observed trend from 1991-2021. **e**, Time series of the global-mean temperature change from the 2001-2011 average: HADCRUT5 observations (black), MPI-ESM historical and RCP8.5 ensemble-mean (dark gray), transition scenario from observed SST to MPI-ESM RCP8.5 SST of 10 years

(light pink), 50 years (red), and 50 years with the trend in the tropical East Pacific replaced by the 1991-2021 observed trend (dashed red); observed SST trend convolved with the GFs from 1991-2021 extended through 2080 (dashed black). **e inset**, Probability density function (PDF) of heating rates for the MPI-GE RCP8.5 ensemble (gray) and $\text{Transition}_{50\text{yr}}$ (red). The heating rates are calculated using a sliding window of 20-year segments for 2015-2044 for each ensemble member. Each PDF consists of 1,000 data points since there are 10 heating rates for each ensemble member. **f**, Time series of the radiative feedback parameter (λ) with colors the same as in (**e**), except including the MPI-ESM RCP8.5 +/- 1σ ensemble spread (gray shading in **f**). Note that a constant SST trend pattern produces a constant λ value ($\text{Transition}_{50\text{yr}}$ around 2035-2060).

2.4 Discussion and Conclusion

We define *SST pattern uncertainty* as the uncertainty arising from AOGCM *forcing response biases* and AOGCM underestimation of the true range of internal variability in SST in future projections that is not captured by the classical three uncertainties as they are currently simulated. We find that *SST pattern uncertainty* significantly impacts global warming projections. This can reduce or strengthen the warming relative to standard climate projections in which the SST is generated internally by the model. Specifically, accounting for likely SST pattern scenarios could result in a global-mean surface temperature of more than a degree above current AOGCM projections for RCP8.5 (Figure 2.2a). When compared to the total model uncertainty in CMIP5 (IPCC, 2014), *SST pattern uncertainty* can increase total model uncertainty by 40% assuming similar responses across models to a redistribution of SST in the West Pacific. We find the ranges of uncertainty in RCP8.5 and 4.5 overlap for 15 years longer than without *SST pattern uncertainty*.

SST pattern uncertainty works mostly through local and nonlocal SW cloud, lapse rate, and LW cloud feedbacks (Figure A.2.4). A warmer West Pacific than the one simulated by AOGCMs for RCP8.5 amplifies the negative feedback already active and dominant in the standard RCP8.5. A shift of more warming to the East Pacific or Southern Ocean destabilizes the lapse rate and SW cloud feedbacks. We find that a warming in the equatorial West Pacific has a

greater impact on the SW feedback and MSCD (nonlocal) than a warming in the tropical East Pacific (local). We do not expect our results to qualitatively depend on the model we are using, since the GFs in other studies are spatially similar to ECHAM6 (Bloch-Johnson et al. 2024; Dong et al. 2019; Zhang et al. 2023; Zhou et al. 2017).

SST pattern uncertainty could provide a false sense of security and place doubt in overall AOGCM skill. For example, an SST pattern unforeseen by AOGCMs may trigger a period of weakened warming. In this case, mitigation and adaptation efforts may slow as the world's decision makers question the accuracy of AOGCM temperature projections. This situation is keen to observations over the last few decades: a cooler than simulated tropical East Pacific and warmer than simulated equatorial West Pacific led to less global warming than possible with another warming pattern (Zhou et al. 2021). But the cooling in the tropical East Pacific and Southern Ocean, likely unpredicted by models due to a *forcing response bias*, is expected to reverse, with some indication that this reversal is already underway (Andrews et al. 2022; Heede et al. 2020; Heede and Fedorov 2021; Loeb et al. 2021; Park et al. 2022). While the exact timing or rapidity of the reversal is uncertain, we show that a period of abrupt warming, with heating rates up to 60% higher than those currently suggested by AOGCM simulations, may occur in the near-term (Figure 2.3e, inset).

We argue that *SST pattern uncertainty* must be considered in future temperature projection uncertainty. AOGCMs are the best tools we have in predicting climate change; however, until we trust AOGCM-generated SST patterns and mechanisms leading to those patterns, we suggest developing SST pattern scenarios or storylines based on theory and observations of patterns of SST trends and ocean heat uptake. If AOGCMs were able to occasionally reproduce the observed SST trend pattern over the last few decades, *SST pattern*

uncertainty would not be necessary to distinguish from the three classical uncertainties of emissions scenarios, structural model differences, and internal variability (Figure A.2.1; Hawkins and Sutton 2009; Lehner et al. 2020).

Improving modeled ocean-atmosphere interactions to reduce mean-state biases and *forcing response biases* would increase trust in the modeled SST pattern evolution and reduce *SST pattern uncertainty*. Potentially, higher resolution modeling and a better mean-state ocean stratification would result in more trustworthy SST trend patterns (Chang et al. 2020), but in general good hypotheses or suggestions for how to improve and test *SST pattern uncertainty* are currently in high demand.

CHAPTER 3: POTENTIAL NEAR-TERM WETTING OF THE SOUTHWESTERN UNITED STATES IF THE EASTERN AND CENTRAL PACIFIC COOLING TREND REVERSES[2]

3.1 Introduction

As anthropogenic climate change continues, the risk of drought is expected to increase in the southwestern United States (SWUS), home to nearly sixty million people, mainly due to an increase in evapotranspiration and an overall drying of soils due to higher temperatures (Cook et al. 2014; Ault 2020). In fact, a severe, multi-decadal drought, known as a "megadrought," is ongoing since the beginning of the 21st century in the SWUS (Williams et al. 2022; Cook et al. 2021). Rather than being caused by increased evapotranspiration from warming, this drought developed from a decrease in precipitation due to a combination of internal atmospheric variability and forcing from sea surface temperature (SST) anomalies in the Equatorial Pacific (Lehner et al. 2018; Seager et al. 2015). Here, we focus on how long-term SST trends (30-year trends) drive SWUS precipitation trends in projections.

It is well established that the SWUS hydroclimate is sensitive to Tropical Pacific SST patterns, with the El Niño-Southern Oscillation (ENSO) being a dominant driver of interannual hydroclimate variability for the SWUS (e.g., Evans et al. 2022; Hoerling et al. 1997; Redmond and Koch 1991). Warmer SSTs in the Central and East Pacific, which are characteristic of a warm-phase ENSO event (referred to as an El Niño), shift the area of deep convection eastward from the West Pacific warm pool to the Central Pacific. The area of peak divergence then shifts

[2] Alessi, M. J., & Rugenstein, M. A. A. Potential Near-term Wetting of the Southwestern United States if the Eastern and Central Pacific Cooling Trend Reverses. *In review at Geophysical Research Letters*.

in the upper tropical troposphere, thus exciting midlatitude Rossby waves (Sardeshmukh and Hoskins 1988; Horel and Wallace 1981). This results in an extension of the northern subtropical Pacific jet, bringing anomalous moisture and precipitation to the SWUS (Deser et al. 2018; Hu et al. 2021; Ropelewski and Halpert 1986; Seager et al. 2010). While the ENSO phase is a helpful predictor of the SWUS hydroclimate, the precipitation response is nonlinear with respect to temperature (Hoerling et al. 1997; Hoerling and Kumar 2002; Seager et al. 2015), meaning that a change in SWUS precipitation does not scale linearly with a change in SST. A warming in the East Pacific (El Niño) results in an increase in precipitation in the SWUS, while the impacts of a cooling East Pacific (La Niña) are less certain (Seager et al. 2015) but tend to lead to SWUS drying (Carrillo et al. 2022). Furthermore, internal atmospheric variability has a larger role than SST forcing in explaining SWUS precipitation variance, as most historical droughts are unrelated to SST forcing (Cook et al. 2018; Schubert et al. 2016; Seager et al. 2015). In observations, SWUS precipitation is moderately positively correlated to changes in Equatorial Pacific SST (Figure 3.1a). This correlation also exists in the Max Planck Institute Earth System Model Grand Ensemble (MPI-GE), though to a lesser extent in the average of the 100 ensemble members (Figure 3.1b).

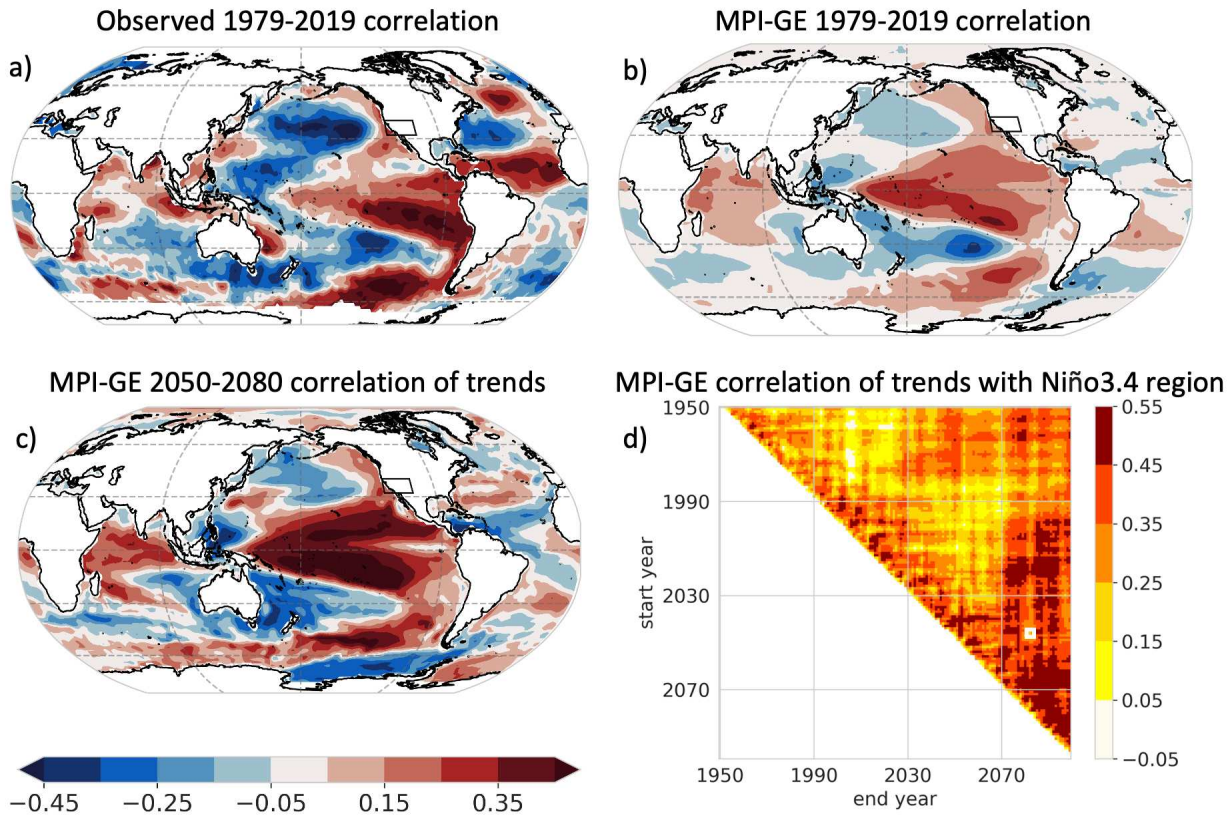

Figure 3.1. a) The observed 1979-2019 correlation between annual-mean Southwestern United States (SWUS) precipitation (Global Precipitation Climatology Project) and sea surface temperature (SST; HadISST) at each grid point. b) The simulated 1979-2019 correlation between annual-mean SWUS precipitation (32°N to 40°N, 124°W to 105°W) and SST at each grid point in the MPI-GE. Correlation is first calculated across 1979-2019 within each ensemble member and then the average of the ensemble is taken. c) Correlation between the trends in SWUS precipitation and SST at each grid point for years 2050-2080 in the MPI-GE Representative Concentration Pathway 8.5 (RCP8.5) scenario. The trend is first calculated within each ensemble member, and then the correlation is taken across the ensemble. The color bar in c) applies to a) and b) as well. d) Correlation between the trends in SWUS precipitation and Niño3.4 region (5°S to 5°N, 170°W to 120°W) SST for different start and end years when calculating the trend. The small white box in d) denotes the situation in panel c).

Dettinger et al. (1998) found that the relationship between Tropical Pacific SST and SWUS precipitation on interannual timescales (2-7 years) holds for decadal timescales (7+ years) in observations, i.e., a decadal-long cooling trend in the East Pacific is linked to long-term drying in the SWUS. Schubert et al. (2016) and Seager and Hoerling (2014) confirmed a link between long-term trends (decades long) in SST and SWUS precipitation during the historical era using

prescribed SST atmospheric general circulation model (A-GCM) simulations across different models. We find a similar relationship in the MPI-GE (Figure 3.1d): a moderate correlation exists between SWUS precipitation trends and Central Pacific SST trends for the historical period (starting and ending years pre-2014). Furthermore, some decades are correlated while others are not at all (e.g., 1960-1990 has a higher correlation than 1970-2000), meaning that studies focusing on one timescale might over- or underpredict the link between SWUS precipitation and Central Pacific SSTs. Longer trends are generally more strongly correlated (top right of Figure 3.1d) and trends should be taken over longer periods than 20 years to avoid noise (diagonal of Figure 3.1d). This dependence of SWUS precipitation trends on Tropical Pacific SST trends suggests possible skill in predicting SWUS precipitation based on the long-term SST trend in the Tropical Pacific. Naturally, this skill in projecting SWUS precipitation exists only if atmosphere-ocean general circulation models (AO-GCMs) correctly simulate the SST trend pattern.

Unfortunately, AO-GCMs fail to replicate the observed SST trend pattern in the Tropical Pacific for many time periods since 1950 (e.g., Wills et al. 2022; Rugenstein et al. 2023). The observed cooling trend (1990-2020) in the East and Central Pacific not replicated by historical simulations in AO-GCMs could indicate that models' response to anthropogenic forcing is erroneous (e.g., Seager et al. 2019; Heede and Fedorov 2021) or that their range of internal variability is too small (Olonscheck et al. 2020; Watanabe et al. 2021). The Eastern Pacific is in fact warming in trends starting after 1995 – although we do not know whether this is due to internal variability or the forced response to greenhouse gases or aerosols. The current warming could be a signal of an advanced forced response to greenhouse gases (Heede et al. 2020). By initializing AO-GCMs with observed wind-stress anomalies in the Tropical Pacific, Delworth et

al. (2015) found that models could replicate the observed cooling trend in the Central and East Pacific, which then resulted in a tropical dynamical setup conducive for development of SWUS drought. Given the relationship between Tropical Pacific SST and SWUS precipitation trends, we here analyze how a likely near-term warming trend in the Central and East Pacific might affect SWUS precipitation.

In this paper, we: 1) test the sensitivity of SWUS precipitation trends by slightly adjusting the likely erroneous near-future SST trends an AO-GCM produces by its free ocean-atmosphere interaction; 2) predict a wetting trend in the SWUS over the next few decades if the cooling trend in the East Pacific reverses. We do not attempt to argue whether the erroneously simulated SST trends in the Tropical Pacific are due to model errors in the forced response or due to an incorrect representation of internal variability. Given that modeled trends in SST are incorrect over the last few decades, we ask how SST trends affect SWUS precipitation in the future if this model error continues.

3.2 Methods

We developed a precipitation Green's function (GF_P) to identify which SST regions influence SWUS (32°N to 40°N, 124°W to 105°W) precipitation (e.g., Alessi and Rugenstein 2023; Bloch-Johnson et al. 2024; Dong et al. 2019; Zhang et al. 2023; Zhou et al. 2017). We selected this region based on previous work (Evans et al. 2022), and our results do not depend on changes to the box within a reasonable definition of the SWUS. A GF is derived from multiple simulations of one A-GCM where anomalous SST patch perturbations are prescribed locally while elsewhere the SST is kept constant (see Text B.1.1 and Figure B.2.1 for details on the development of the GF). The GF is developed using the response averages over 20 years to a constant local SST forcing, making the tool ideal for studying the relationship of long-term

trends in SST and precipitation. A GF is advantageous to using a coupled AO-GCM or uncoupled A-GCM because atmospheric variability is removed when calculating the precipitation response, i.e., we can causally attribute a precipitation response directly to a change in local SST. When using an AO-GCM or A-GCM, atmospheric noise makes the connection less obvious and causal attribution of precipitation more difficult. For example, in A-GCM simulations with a complete spatial and temporal SST pattern prescribed, as in Schubert et al. (2016) and Seager and Hoerling (2014), the precipitation response is a result of both a change in the SST pattern and fluctuations in atmospheric variability and hence sensitively depend on the timing of trend analyses, even for trends over several decades (Fig.1d). In addition, precipitation changes cannot be attributed to one specific region as the whole pattern is prescribed.

The global-mean GF_P is quantitatively similar to GF_P in Zhang et al. (2023; not shown). In this study, we utilize a regional GF_P to focus only on SWUS precipitation response to SST (Figure 3.2a). Precipitation in the SWUS is most sensitive to changes in SST in the Central Pacific and the Caribbean (Figure 3.2a), which corroborates the moderate correlation between SWUS precipitation and Central Pacific SST (Figure 3.1c). An increase in SST in the Central Pacific (denoted by green in Figure 3.2a) leads to more precipitation in the SWUS. The opposite is true for the Caribbean (denoted by brown in Figure 3.2a). This result qualitatively confirms the GF work by Barsugli and Sardeshmukh (2002), confirms the well-studied teleconnection to the Central Pacific (e.g., Hoerling et al. 1997; Redmond and Koch 1991), and backs empirical orthogonal analysis of SST and SWUS precipitation (Hu et al. 2021). Note that while we do not trust the SST pattern in AO-GCMs, we, in principle, trust the link between SST and precipitation trends because models reproduce observational precipitation given the SST pattern (Dettinger et al. 1998; McCabe et al. 2004).

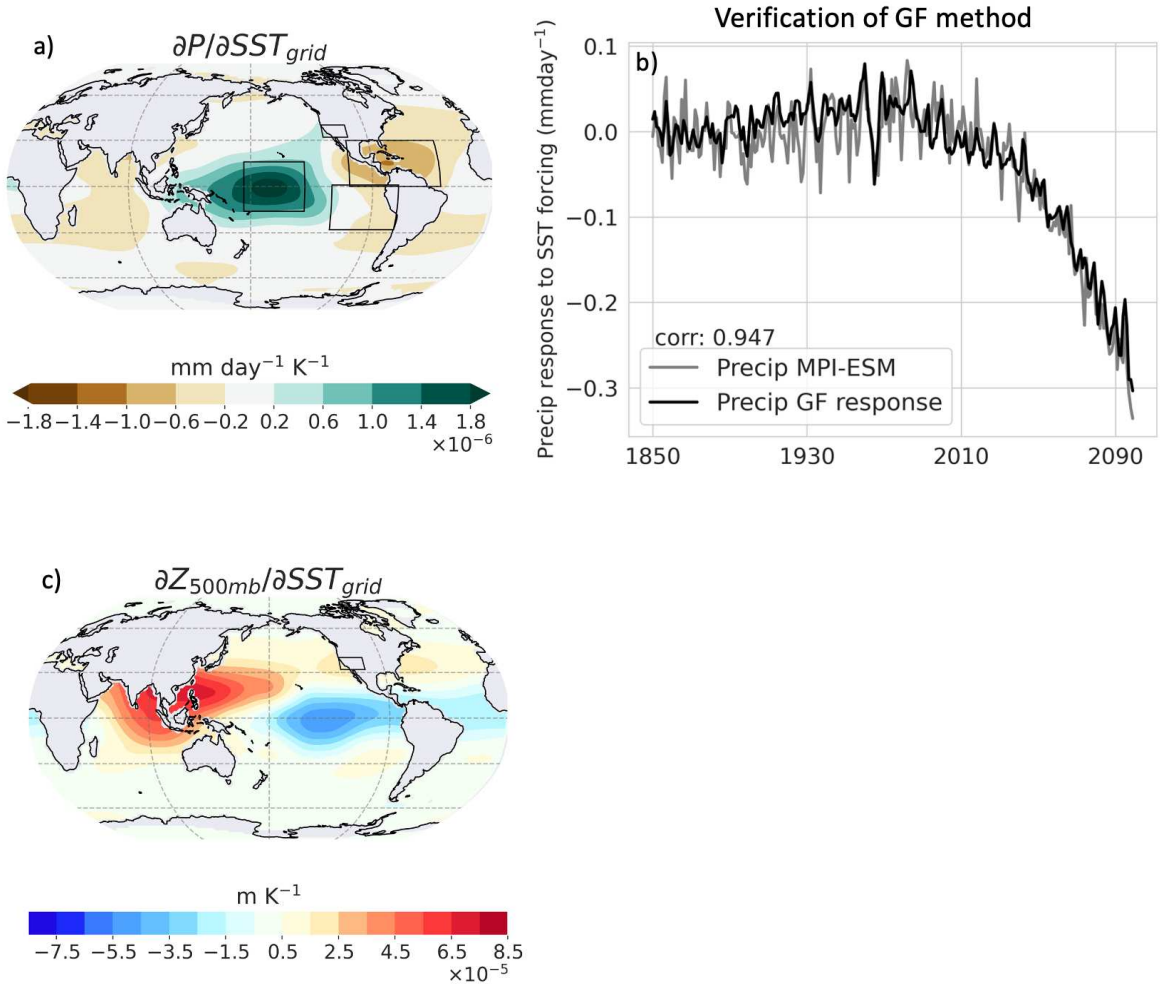

Figure 3.2. a) The annual-mean SWUS precipitation response per unit SST warming in each grid box. A warming in a green (brown) region on this map results in an increase (decrease) in precipitation over the SWUS. From the northernmost box going clockwise: the SWUS (32°N to 40°N, 124°W to 105°W), Caribbean region (0°N to 30°N, 107°W to 40°W), East Pacific region (28°S to 1°N, 120°W to 71°W), and Central Pacific region (16°S to 16°N, 175°E to 140°W). b) The SWUS precipitation response of the Green's function convolved with the MPI-GE SST pattern (black) reproducing the SWUS precipitation output from the MPI-GE historical and RCP8.5 simulations (gray). c) The annual-mean 500 mb geopotential height response averaged over the SWUS region per unit SST warming in each grid box.

We "tune" GF_P to reproduce the SWUS precipitation output from the historical and RCP8.5 MPI-GE ensemble-mean simulations (Figure 3.2b), similar to Dong et al. (2019) and Alessi and Rugenstein (2023). Without tuning, the GF predicts too much wetting in the SWUS

(Figure B.2.2). While GF_P identifies physically meaningful SST regions as impactful to SWUS precipitation, it probably overestimate the SWUS precipitation response given a warming in the Central Pacific due to nonlinearities of the climate system that GF_P cannot capture (Williams et al. 2023). We correct this error in GF_P by subtracting the same small value ($8.6x10^{-5}$) from each index of the GF_P matrix (see discussion of alternate tuning methods in Text B.1.2). Our results hold qualitatively for the untuned GF_P and for different choices of tuning. This is because the tuned GF_P has the same pattern as the original GF_P, so a warming in the Central Pacific (Caribbean) still results in a wetting (drying) of the SWUS. So far, GFs have been used only to calculate a climate response in the global-mean. In this study, we use a regional GF that is tuned for a specific range of SST and precipitation variations, i.e., for surface temperature variations of a few K and precipitation responses of a few tenths of mm day^{-1}. Tuning and applying a regional GF is a much more stringent use of the tool than the global-mean GF for radiation, which works well for situations very different from the one it was constructed and tuned for (see discussion in Alessi and Rugenstein 2023).

We develop a 500 mb geopotential height Green's function (GF_Z), a 200 mb u-wind Green's function (GF_u), and a 200 mb v-wind Green's function (GF_v) to verify if GF_P changes precipitation in the SWUS as a result of warming in the Central Pacific for the right dynamical reasons. How the subtropical jet stream responds to changes in the SST pattern is explained by GF_Z (Figure 3.2c), GF_v, and GF_u (Figure B.2.3), which represent the location of troughs and ridges, meridional displacement of the jet stream, and intensity of the jet stream, respectively. A warming of the Central Pacific decreases both the v-wind at 200 mb and the geopotential height over the SWUS, indicating a southward shift of the subtropical jet stream from the Pacific Northwest and a deepening trough over the SWUS, respectively, which allow for an increase in

precipitation in the SWUS. These dynamical GF sensitivity maps confirm a path for increased precipitation in the SWUS given a warming in the Central Pacific (e.g., Hu et al. 2021; Seager et al. 2010).

In the following, we adjust SST trend patterns by cooling and warming the SST trend in the Caribbean, the Central Pacific, and the East Pacific to test the sensitivity of SWUS precipitation to SST in these regions (Section 3.1). We then develop plausible future SST pattern storylines starting from observations and calculate the SWUS precipitation response to these SST patterns using GF_P (Section 3.2).

3.3 Results

3.3.1 Sensitivity of the SWUS Precipitation Trends to SST Trends

We adjust the SST trend in different regions to quantitatively assess the impact corrected (or more likely correct) SST trends have on SWUS precipitation. We first test six idealized scenarios: a cooler and warmer Caribbean, a cooler and warmer Central Pacific, and a cooler and warmer East Pacific than the RCP 8.5 MPI-GE simulations. In each region, an equally large area is warmed or cooled by 3% of the global-mean SST anomaly in RCP8.5 compared to the pre-industrial control simulation for each year. The 3% anomaly applied to each region is inspired by the magnitude of AO-GCM error in simulating SST trends over the last few decades. For reference, 3% of the global-mean temperature anomaly for each year is plotted in Figure B.2.5. While 3% is a small value, we concentrate this anomaly into a region of interest. For example, by 2085, a 3% anomaly of the global-mean SST change in the RCP8.5 simulation is about 0.06 K but becomes 1.1 K when that 0.06 K anomaly is concentrated into a region of interest (e.g., the Central Pacific), which is comparable to model error in the tropical East Pacific (Figure 1 in

Seager et al. 2019) and the Southern Ocean (Figure 2 in Wills et al. 2022). To maintain the same global-mean SST anomaly in the scenario as in the RCP8.5 simulation, the SST at other grid points around the globe, outside the region of interest, is slightly adjusted (an area-weighted cooling is applied to the rest of the world for a warming scenario, and vice-versa for a cooling storyline). Alessi and Rugenstein (2023) apply this method to net top-of-atmosphere radiative imbalance (see more details in Supplemental Text B.1.3).

Adjusting the SST trend in different regions by a modest amount significantly affects the SWUS precipitation trend (Figure 3.3a). As expected, changes in Central Pacific SST trends affect SWUS precipitation trends the most via changes in the midlatitude Rossby wave train, which can lengthen the subtropical Pacific jet, bringing more or less precipitation to the SWUS. The precipitation, 500 mb geopotential height, and specific humidity response to a warm anomaly patch simulation in the Central Pacific demonstrates increased precipitation and specific humidity as a result of a more prominent trough over the SWUS (bottom row in Figure B.2.4). We find that SWUS precipitation decreases by 0.44 mm day^{-1} over the SWUS by 2085 compared to the standard coupled model projections due solely to a nearly 1.1 K decrease in Central Pacific SST. This is on the same order of magnitude as in the AO-GCM simulations from Delworth et al. (2015). Adjusting the SST trend in the Caribbean leads to an opposite and weaker SWUS precipitation response than warming or cooling in the Central Pacific. In empirical orthogonal function analysis of observations, there is some indication of the Caribbean having an opposite impact to the Central Pacific on SWUS precipitation during the spring season (Figure 3 in Hu et al. 2021). The response of a Caribbean warm anomaly patch simulation, there is a clear decrease in SWUS precipitation linked to lower specific humidity because of a lack of northward moisture transport (top row in Figure B.2.4), possibly inhibiting the North American monsoon. Instead of

moisture moving into the SWUS during the boreal summer, this moisture is instead focused over the region of warming, where more precipitation occurs. However, in one paleoclimate study, a decrease in SST in the Gulf of California resulted in less precipitation in the SWUS due to decreased northward surges of tropical moisture (Barron et al. 2012), which contradicts our GF (and patch simulation) result. We attribute this difference to a different North American monsoon structure, for example, the monsoon affected a much broader area 8,000 years ago (Barron et al. 2012). Finally, changing the East Pacific SST trend does little in impacting SWUS precipitation as expected from Fig. 2a.

Critically, the SWUS could experience opposite trends in precipitation (wetting or drying) based on a small redistribution of SST. For example, if the Central Pacific (Caribbean) warms more than what AO-GCMs predict, indicative of a background mean-state El Niño, the SWUS would experience a wetting (drying) trend. On the other hand, if the Central Pacific (Caribbean) cools more than what AO-GCMs predict, the SWUS would experience a drying (wetting) trend. We applied these SST redistributions to the SST fields of all 100 MPI-GE ensembles members and took the ensemble-average after calculating the precipitation response to remove the impact of internal atmospheric variability. While atmospheric variability can be more important in affecting SWUS precipitation than SST forcing (compare the width of shading in Figure 3.3a to the magnitude of the mean response), we demonstrate here that in the ensemble-mean, the overall precipitation trend shifts based on the SST pattern trend, making it easier or more difficult for a precipitation deficit to develop in the SWUS.

Without any SST adjustment, the MPI-GE ensemble-mean predicts a slight drying over the 21st century (Figure 3.3a; gray line). This is due to a slow expansion of the Hadley Cell and a poleward shift of the subtropical dry zone (e.g., Lau and Kim 2015; Grise and Davis 2020). For

other CMIP5 models, little precipitation change is projected in the model-mean for the SWUS, although there is considerable spread among the models (Rojas et al. 2019).

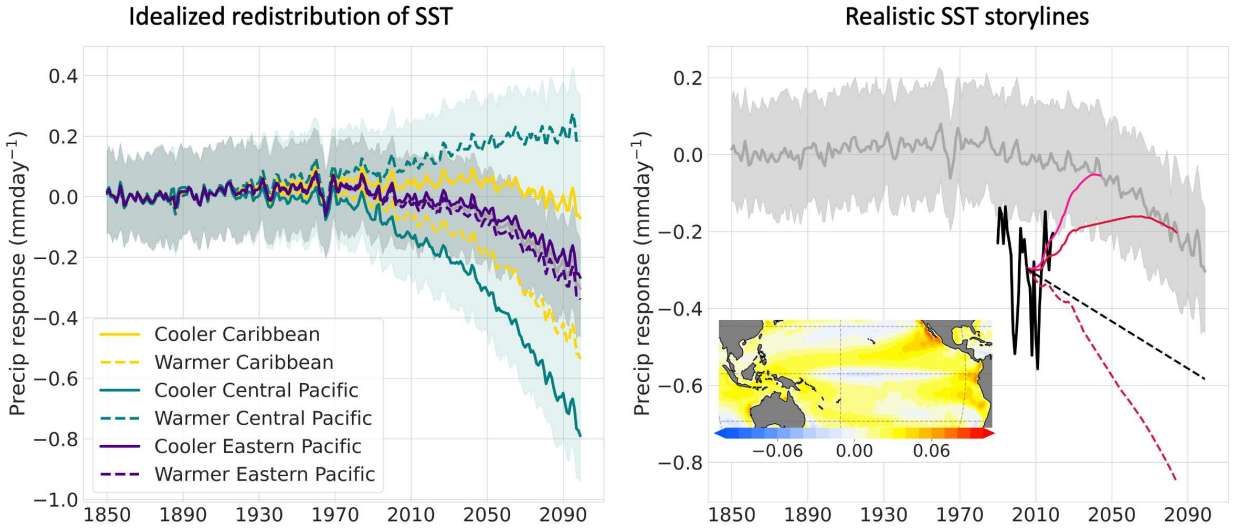

Figure 3.3. *Effect of idealized redistribution of SST on SWUS precipitation (left).* SWUS precipitation anomaly from the 1850-1870 average: MPI-GE historical and RCP8.5 projection ensemble-mean (gray); MPI-GE historical and RCP8.5 ensemble spread (+/- 1σ; gray shading); *Effect of adjusting SST trends starting from observations (right).* SWUS precipitation anomaly from the 1850-1870 average: MPI-GE historical and RCP8.5 projection ensemble-mean (gray; as in a, note different range in vertical axis); MPI-GE historical and RCP8.5 ensemble spread (+/- 1σ; gray shading); HadISST convolved with the SWUS GF$_P$ (black); precipitation response from transition SST scenarios starting from observed SST and ending with MPI-GE RCP8.5 SST over 10 years (dark pink), 50 years (red) and 50 years with the trend in the Central Pacific replaced by the 1991-2021 observed trend (dashed red); observed 1991-2021 SST trend convolved with the regional precipitation GF extended through 2100 (dashed black). The SST trend for the 50-year transition SST scenario (red) is plotted in the inset figure in units of K yr^{-1}.

3.3.2 SST Storylines Starting from Observations

The SWUS precipitation response from the observed SST pattern (HadISST) convolved with the GF$_P$ over the last few decades is noticeably lower than the MPI-GE (Figure 3.3b, black line). This demonstrates the GF$_P$'s ability to replicate the observed decrease in SWUS precipitation that led to drought conditions since the start of the 21st century.

Given that there is already a discrepancy between the observed and simulated SST trend pattern, we develop a more realistic SST pattern trend storyline that evolves from the currently

observed SST pattern into the future. This storyline approach constrains future SWUS precipitation projections to be consistent with both the currently observed SST pattern and how we expect the SST pattern to evolve based on theory. The East Pacific is likely to switch from a cooling trend (1990-2020) to a warming trend at some point in the future as greenhouse gas forcing continues and aerosol forcing decreases (e.g., Andrews et al. 2022; Heede et al. 2020; Heede and Fedorov 2021; Park et al. 2022), and in fact trends starting in the late 1990s are already positive. To reproduce this effect, we interpolate the observed SST at each grid point from the 2016-2021 average to the average SST pattern in the MPI-GE RCP8.5 for 2031-2036 and 2071-2076 (Figure 3.3b; Supplemental Text B.1.4). This interpolation includes a stronger warming of the subtropical East Pacific and Central Pacific than the equatorial West Pacific (Figure 3.3b inset), which is opposite of the trends observed since the 1970s. We choose two transition storylines, one 10 years in length (2021-2031) and one 50 years in length (2021-2071), since it is unknown how quickly or when the East Pacific may warm. These storylines assume that we trust the response of the models in the 2030s or 2070s. Below, we also relax this assumption. Both transition storylines result in increased precipitation for the SWUS over the next few decades. The 10-year transition storyline experiences a faster wetting than the 50-year transition storyline due to a faster warming in the Central and East Pacific. However, for both scenarios, after a period of wetting occurs due to the warming Central and East Pacific, the drying from the expanding Hadley Cell takes over as the transition storylines merge with the MPI-GE. For both storylines, while there is some warming in the Caribbean, the greater warming in the Tropical Pacific and higher sensitivity of SWUS precipitation to this region (Figure 3.2a) results in an overall wetting. Of note is the abrupt increase in SWUS precipitation for the transition storylines. We calculate the rate of change in SWUS precipitation for each ensemble

member for all 20-year segments centered on 2025-2044 (in total there are twenty 20-year segments). The ensemble-mean rate of change in precipitation is -0.00120 mm day^{-1} $20yr^{-1}$ for RCP8.5 and 0.00125 mm day^{-1} $20yr^{-1}$ for the 50-year transition storyline, indicating a greater (and positive) rate of change in SWUS precipitation for the storyline. If the observed SST trend pattern were to reverse in the Central and East Pacific from a cooling trend to a warming trend, as in the transition storylines, we may for several decades observe a wetting of the SWUS in spite of global warming. Note that this might happen independent of whether changes in the trends are due to decadal-scale internal variability or the forced response.

We develop two more storylines that assume SST projections from the RCP8.5 MPI-GE are either partly or fully incorrect. The first storyline is the same as the 50-year transition storyline in that the SST at each grid point is interpolated from observations to the RCP8.5 in 2071, however, the SST trend in the Central Pacific is replaced with the extrapolated 1991-2021 observed SST cooling trend through the end of the century (Figure 3.3b; dashed red line). In this storyline, we assume the AO-GCMs continue to incorrectly simulate the trend in the Central Pacific, and that the SST trend will continue to cool slightly (Seager et al., 2019). The difference between the dashed red line and the solid red line in Figure 3.3b is solely the influence of the Central Pacific cooling rather than warming. Despite warming across the rest of the globe, a cooling Central Pacific would result in continued drying for the SWUS, given its significant sensitivity to SST trends in that region (Section 3.1).

For the second storyline, we extrapolate the 30-year observed SST trend from 1991-2021 forward in time at each grid point (Figure 3.3b; black dashed line). We discard RCP8.5 SST pattern trend projections completely, or in other words, we do not trust the AO-GCM SST pattern trend at all. The extrapolated observed trend features a cooling Central and East Pacific,

which results in a decreasing SWUS precipitation trend that remains below RCP8.5 projections through the end of the century. This storyline remains wetter than the combined 50-year transition and observed Central Pacific storyline due to the latter including warming in the Caribbean, which enhances the drying signal of that scenario. Overall global warming is significantly less in this storyline due to a more stabilizing global-mean radiative feedback (Alessi and Rugenstein 2023), which could lead to less drying in the SWUS from the Hadley Cell not expanding as much as in RCP8.5 projections. We conclude that in the near-future, the pattern of SST trends is highly relevant for the sign and magnitude of projections of SWUS precipitation.

3.4 Discussion and Conclusions

There is skill in predicting the precipitation trend in the SWUS based on the Equatorial Pacific SST trend pattern (Figure 3.1c; Dettinger et al. 1998; Schubert et al. 2016; Seager and Hoerling 2014). However, AO-GCMs fail to replicate the observed SST trend pattern in recent decades (e.g., Wills et al. 2022). While AO-GCMs predicted a warming SST trend in the Central and East Pacific, the region instead experienced a cooling SST trend from 1970-2014 (e.g., (Coats and Karnauskas 2017; Seager et al. 2019), which potentially led to the observed megadrought in the SWUS due to a decrease in precipitation (Delworth et al. 2015; Seager and Hoerling 2014). The cooling of the Central and East Pacific not simulated by AO-GCMs may have been caused by a forced response to greenhouse gas emissions (Coats and Karnauskus 2017; Heede et al. 2020), a forced response to aerosols (Heede and Fedorov 2021; Kuo et al. 2023), internal variability in the climate system (Olonscheck et al. 2020; Watanabe et al. 2021), missing or poorly simulated teleconnections in climate models (e.g., Dong et al. 2022; Kang et al. 2023; Kim et al. 2022), or a combination of these factors. At least part of the megadrought

was related to a lack of precipitation from the cooling Central and East Pacific, rather than due to a significant increase in evapotranspiration from global warming (Seager et al. 2015), which will likely cause droughts in the future as anthropogenic climate change worsens (e.g., Cook et al. 2014; Diffenbaugh et al. 2015). In this study, we confirmed the connection between the Equatorial Pacific SST trend pattern and SWUS precipitation trends with a Green's function approach, which allows us to establish a causal link between SST and precipitation. We developed SST pattern trend storylines to predict how SWUS precipitation could change over the next century:

A very modest redistribution of SST could lead to a wetting or drying of the SWUS using GF_P (Figure 3.3a). A warming of the Central Pacific results in a wetting of the SWUS due to a shift in deep tropical convection to the Central Pacific that excites the midlatitude Rossby wave such that the Pacific jet is extended into the SWUS, bringing moisture and precipitation (Figure B.2.4). We also highlight a potentially strong teleconnection between the Caribbean and the SWUS, which may be overlooked in the past due to weak warming and/or internal variability in observational studies. A warming of the Caribbean and Gulf of Mexico results in a drying of the SWUS due to a decrease in incoming moisture from the Caribbean (Figure B.2.4), which could inhibit monsoon development (Ordoñez et al. 2019). The moisture instead remains in the Caribbean in order to fuel the increased convection due to the warmer SSTs.

The sign dependence of the SWUS precipitation trend on the SST trend pattern complicates prediction of future SWUS drought; since AO-GCMs are unable to replicate relevant aspects of the observed SST pattern trend, they may continue doing so in the future, confounding SWUS precipitation projections. This finding increases the total uncertainty of SWUS precipitation in projections. Some models predict a wetting of the SWUS by the end of

the century due to an extension of the Pacific jet stream, bringing in more precipitation to the SWUS (Deser et al. 2018; Dong and Leung 2021; Grise and Davis 2020). There also may exist a thermodynamic response which adds further uncertainty to subtropical land precipitation (He and Soden 2017). Given that similar GF_P sensitivities exist in the GFDL model (Zhang et al. 2023) and the National Centers for Environmental Prediction model (Barsugli and Sardeshmukh 2002), this result of the sign of SWUS precipitation trends being dependent on the Tropical Pacific SST is likely robust across AO-GCMs and a modest redistributions of SST trend patterns in the future will likely affect the sign of precipitation change in other AO-GCMs.

We note that internal atmospheric variability plays a large role in explaining interannual SWUS precipitation variance (e.g., Seager et al. 2015), so that even if the Central Pacific cools, the SWUS could experience a few wet years if atmospheric conditions are favorable. However, in long-term trends, all ensemble members still experience a drying in the SWUS if the Central Pacific cools (Figure 3.3a, solid teal line).

We also constrain projections of SWUS precipitation trends by developing storylines that start from the observed SST trend pattern (Figure 3.3b). If the Central and East Pacific continue cooling, a prolonged period of drought is more likely to continue in the SWUS. However, if the Central and East Pacific warm over the next few decades, as theory suggests (Heede et al. 2020), the SWUS would see a period of increased precipitation. This transition to a warming Central and East Pacific may have already begun (Andrews et al. 2022; Loeb et al. 2020; Rugenstein et al. 2023). Our approach does not consider changes in soil moisture and evaporative demand. The state of the hydroclimate overall could still experience drying with increased precipitation if there is a significant increase in evaporative demand, as suggested by models (Cook et al. 2014,

2015; Mankin et al. 2021; Schubert et al. 2016), though over the past 60 years evaporative demand may have had little impact (Sheffield et al. 2012).

Our work demonstrates that correctly modeled SST trend patterns are critical for SWUS precipitation projections. Improved and higher resolution modeling of ocean-atmosphere interaction may reduce mean-state biases and make the response to forcing more realistic in SST, allowing for more accurate simulation of Central and East Pacific SST trends. While AO-GCMs may fail to capture the future SST trend, and therefore the future SWUS precipitation trend, we here predict SWUS precipitation trends given likely storylines of future SST trend patterns. The possible wetting of the SWUS in the near-term should not deter efforts to limit water use and to prepare for significant drought in the SWUS, as there is ample evidence of increased drought under a drier overall hydroclimate due to anthropogenic climate change (Ault 2020; Cook et al. 2014). However, a near-term wetting would bring relief to the drought stricken SWUS, which could prove crucial for adaptation and mitigation efforts in that region.

CHAPTER 4: USING EXPLAINABLE AI TO INFORM CLIMATE MODEL SIMULATIONS: A POTENTIAL SOUTHERN HEMISPHERE SURFACE WARMING INFLUENCE ON SOUTHWESTERN U.S. PRECIPITATION ON LONG TIMESCALES[3]

4.1 Introduction

Long-term precipitation trends (7+ years) in the southwestern United States (SWUS; 32°N to 40°N, 124°W to 105°W) are partially driven by sea surface temperature (SST) trend patterns (Alessi and Rugenstein 2024; Dettinger et al. 1998; Seager and Hoerling 2014). The evolution of the SST pattern is influenced by both the response of the climate system to internal variability and anthropogenic climate change. The former is controlled by intrinsic oscillations that develop from atmosphere-ocean interactions in the climate system. SST pattern anomalies can develop from the imprint of intrinsic modes of atmospheric circulation on SST such as the Southern Annular Mode (Deser et al. 2010), and from coupled ocean-atmosphere interactions such as the El Niño-Southern Oscillation (ENSO) or the Pacific Decadal Oscillation. Because these oscillations affect SST trends, they serve as a predictor of SWUS precipitation trends on both short time scales (3-7 years; Evans et al. 2022; Redmond and Koch 1991) and on longer time scales (7+ years; Dai 2013). Typically, warmer SSTs on short and long timescales in the Central and East Pacific lead to more precipitation in the SWUS due to an excitation of midlatitude Rossby waves that extends the northern subtropical Pacific jet into the SWUS (Deser et al. 2018; Hu et al. 2021; Ropelewski and Halpert 1986; Seager et al. 2010). This warming is characteristic

[3] To be submitted to *Journal of Climate* in 2024 after further revisions and a potential restructuring of the article. Alessi, M. J., Barnes, E. A., Connolly, C. J., Rugenstein, M. A. A. (2024). Using Explainable AI to Inform Climate Model Simulations: A Potential Southern Hemisphere Surface Warming Influence on Southwestern U.S. Precipitation on Long Timescales.

of both a positive phase ENSO on short time scales and a positive phase of the Pacific Decadal Oscillation (PDO) on longer time scales. In fact, Dai (2013) demonstrated a strong relationship (correlation >0.85) between SWUS precipitation and the phase of the PDO in long-term historical trends. The phase of the decadal oscillations may also impact the strength of the influence of ENSO SST changes on SWUS precipitation (Maher et al. 2022).

How the SST pattern evolves in response to anthropogenic forcing is less clear, and there is uncertainty in how SWUS precipitation trends may change in the future (Salvi et al. 2017; Rojas et al. 2019). In fact, atmosphere-ocean general circulation models (AOGCMs) already struggle to reproduce the observed SST trend pattern in the Tropical Pacific since at least 1950 (Wills et al. 2022). Over the historical period, AOGCMs predicted a warming of the East Pacific, which reduces the SST gradient between the West and East Tropical Pacific(Seager et al. 2019). However, in observations, the SST trend in the East Pacific has remained stagnant or even cooled, depending on the length of the trend calculated (Rugenstein et al. 2023), leading to a strengthened Tropical Pacific SST gradient with wider implications for the general circulation of the atmosphere (Chemke and Polvani 2019; Chung et al. 2019; Kociuba and Power 2015). While it remains possible the discrepancy between models and observations in SST trends could be an indication of the range of internal variability in AOGCMs being too small (Olonscheck et al. 2020; Watanabe et al. 2021), models may incorrectly simulate the pattern of SST in response to CO_2 and aerosol forcing (Heede and Fedorov 2021; Heede et al. 2020). Critically, AOGCMs likely will continue simulating the SST pattern trend erroneously in the future, which has implications for predictability of SWUS precipitation trends (Alessi and Rugenstein 2024). For example, if the Central Pacific continues cooling rather than warm as AOGCMs suggest, a drying of the SWUS would continue (Delworth et al. 2015; Alessi and Rugenstein 2024). Given

that the SWUS is susceptible to increased drought conditions in the future as anthropogenic climate change persists (Ault et al. 2016; Ault 2020; Diffenbaugh et al. 2015), it is critical for scientists to fully understand which patterns of SST warming drive SWUS precipitation changes so that water resource management can plan accordingly.

There is ample research using both numerical and statistical modeling approaches analyzing how SST patterns affect SWUS precipitation (e.g., Madadgar et al. 2016; Mamalakis et al. 2017, 2018; Dettinger et al. 1998; Schubert et al. 2016; Seager and Hoerling 2014). Barsugli and Sardeshmukh (2002) were the first to develop a Green's function (GF) to test regional precipitation sensitivity to SST anomalies. A GF uses simulations from an atmosphere-only general circulation model (AGCM) to linearly approximate the response of one variable (e.g., precipitation) to a forcing (e.g., SST). In other words, the GF contains information on how precipitation at one location on Earth will respond to an SST change at a different location. For example, the precipitation over Los Angeles might increase by 2 mm day^{-1} given a 1 K increase in the Central Pacific SST, and because the GF is a linear approximation, a 2 K increase in the Central Pacific will lead to an increase in precipitation of 4 mm day^{-1} for Los Angeles. A GF is developed through perturbing an AGCM with an array of localized SST patch anomalies for all SST regions. A climate response for one location to a pattern of SST is the linear combination of the responses to all localized SST patches, meaning that a climate response (regional or global) can be calculated given any global SST pattern, since the sensitivity of the climate response for each SST grid point is known. Barsugli and Sardeshmukh (2002) refer to the GF as having *coarse grain linearity*: while the AGCM used in the patch simulations has knowledge of the nonlinear governing equations, these nonlinearities have been averaged out in space and time, as

the GF averages the climate responses to the patch perturbations over a decade of simulation for each localized patch anomaly.

The precipitation GF showing the sensitivity of SWUS precipitation to SST changes is reproduced from Alessi and Rugenstein (2024) in Figure 4.1a. A warming (cooling) of the green SST regions would result in increased (decreased) precipitation for the SWUS, and opposite for brown colors. Based on observations (Dettinger et al. 1998; Mamalakis et al. 2018) and modeling studies and theory (Hoerling et al. 2010; Hoerling and Kumar 2002; Sardeshmukh and Hoskins 1988), we know the SST regions highlighted as important for SWUS precipitation by the GF are physically meaningful, such as warming in the Central Pacific shifting the northern subtropical Pacific jet southward, bringing more precipitation to the SWUS. However, while we have some trust in the GF as a tool for long-term precipitation trend predictability, there are known issues with the GF, namely its inability to capture important spatial and temperature nonlinearities of the climate system (Williams et al. 2023). Most relevant for SWUS precipitation sensitivity is the spatial nonlinearity. It is well understood that an anomalously warm Central Pacific shifts the region of convection from the West Pacific to the Central Pacific due to the higher SSTs and greater convergence. This localized convection has the effect of raising the tropical free tropospheric stability, which acts to increase the convective initiation threshold over the whole Central Pacific and nearby regions. If extra warming were applied to an area near this already-existing anomalously warm SST region, convection would struggle to initiate over the extra warming region, given the higher convective threshold established by the original warming. Since the GF is developed from anomalous SST patch perturbations that do not have knowledge of the effects of other patch perturbations, the GF significantly exaggerates Central Pacific convection, because convective thresholds will remain the same for each

warming patch, when in reality it should drastically increase if a warming is already observed in a region. This exaggeration of convection then leads to an exaggerated SWUS precipitation response. Alessi and Rugenstein (2024) handle this nonlinearity by tuning the GF to values that replicate climate model output. However, despite tuning, there could still be more SST regions that drive SWUS precipitation that the GF does not capture.

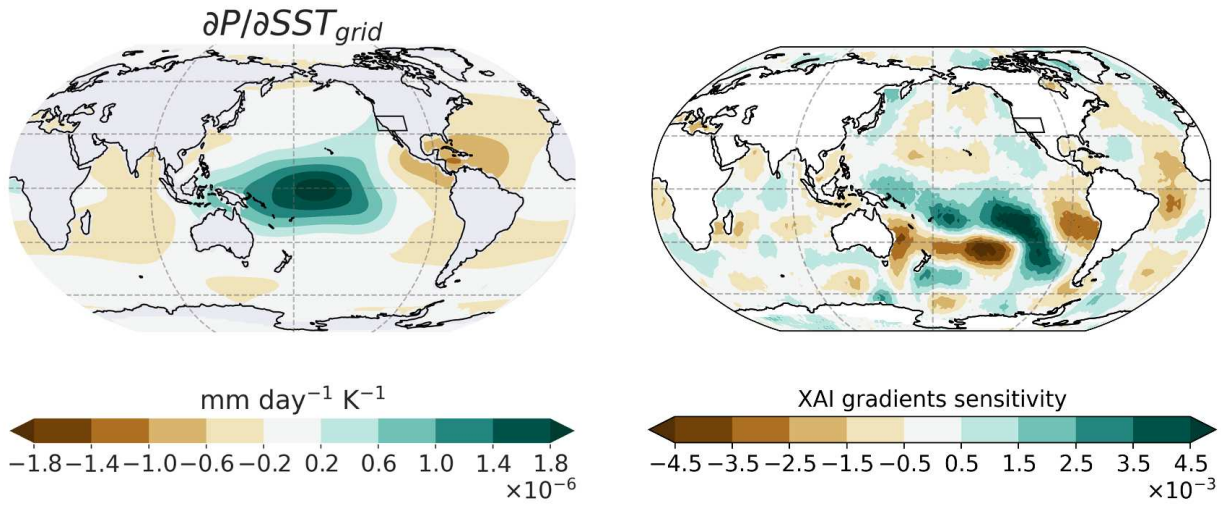

Figure 4.1. SWUS- and annual-mean precipitation response according to the GF (left). XAI gradients heatmap composite for SWUS precipitation (right). The green colors highlight SST regions that result in an increase (decrease) in long-term SWUS precipitation given an increase (decrease) in SST, and vice versa for brown regions. The SWUS region is defined as (32°N to 40°N, 124°W to 105°W).

Other linear approaches have also been employed to identify SST regions that are important for driving SWUS precipitation on long timescales. Dettinger et al. (1998) noted that the same SST regions that drive changes in SWUS precipitation on short timescales (2-7 years) holds for decadal timescales (7+ years) in observations using a correlation analysis. Specifically, a decadal cooling trend in the East Pacific has been linked to long-term drying in the SWUS (Delworth et al. 2015). Other correlation analyses demonstrated heightened sensitivity to Central

Pacific SSTs for long-term SWUS precipitation trends (Alessi and Rugenstein 2024; Schubert et al. 2016; Seager and Hoerling 2014). Mamalakis et al. (2018) were the first to identify a high correlation between SST anomalies off the coast of New Zealand and SWUS precipitation in contrast to the usual sensitivity hotspots of the Central and East Pacific. They found that warming SSTs off the coast of New Zealand induced an anomalous Hadley circulation that led to an increase in descending air near the Philippines. This anomalous descent then suppressed local convection, raising local SSTs. Through coupled ocean-atmosphere processes, the increased SSTs near the Philippines migrated to the North Pacific, which then shifted the jet stream north, drying the SWUS. In this study, we demonstrate that a similar teleconnection works in other SST regions of the Southern Hemisphere.

While linear approaches to detecting the sensitivity of some climate response to SST, such as the GF or a linear inverse model, have proven useful for precipitation predictability (Evans et al. 2022; Alessi and Rugenstein 2024), there is evidence that nonlinear approaches, such as neural networks (NN) and explainable artificial intelligence (XAI), could further identify important and physically meaningful regions for SWUS precipitation sensitivity to SST pattern evolution (Arcodia et al. 2023; Gordon et al. 2021; Beobide-Arsuaga et al. 2023; Mayer and Barnes 2021). On subseasonal timescales, Mayer and Barnes (2021) found that an artificial NN could make skillful predictions of North Atlantic 500 mb geopotential height using outgoing longwave radiation anomalies, which are representative of convection and SST anomalies, in the Tropical West Pacific. Importantly, an XAI technique showed the NN made its prediction using radiation anomalies in regions with known midlatitude teleconnections. Beobide-Arsuaga et al. (2023) used a fully connected NN to predict European summer heatwaves based on the pattern of North Atlantic SST, with XAI demonstrating the importance of the subtropical gyre in heatwave

forecasting. Perhaps most relevant to this study, Arcodia et al. (2023) trained an artificial NN on Tropical Pacific precipitation patterns to predict precipitation anomalies over the western U.S. They used the integrated gradients XAI method to identify precipitation regions most relevant for their prediction. In agreement with the GF method in Figure 4.1a, their XAI method found the Central Pacific most relevant for CA precipitation prediction, although the CNN highlighting this region as important for western U.S. precipitation could be related to a double intertropical convergence zone bias in the AOGCM model (CESM) they used. We note that the goal of these studies is to predict subseasonal to seasonal responses to a given forcing, such as SST or outgoing longwave radiation, while the goal in this paper is to evaluate the sensitivity of the long-term (10-year) SWUS precipitation average to long-term SST patterns.

As anthropogenic climate change persists, drought is expected to become more common due to increased evapotranspiration, and the population and economy of the SWUS will depend on reliable long-term SWUS precipitation predictions to inform water resource management. For example, the Bureau of Reclamation already makes 5-year probabilistic projections of SWUS hydroclimate, river flow, water demand, and policy changes (Bureau of Reclamation 2024). If decadal projections based on SST forcing were shown to be reliable and trustworthy, they could be useful for SWUS water resource management (R. Schumacher, personal communication, 2024). In this study, we compare the sensitivity of SWUS precipitation to SST on long timescales using two methods: 1) the precipitation GF, and 2) a convolutional NN (CNN) trained on patterns of 10-year averaged SST in order to predict 10-year averaged SWUS precipitation. We use the gradients XAI method to identify which SST regions the CNN is most sensitive to for SWUS precipitation. The 10-year timescale for the training of the CNN allows a fairer comparison between the CNN and the GF methods since the GF is developed from averaging the

SWUS precipitation response to 20-year SST anomaly patch simulations, however, the GF can still represent interannual and even seasonal climate responses given the pattern of SST. After the GF is developed and the CNN is trained, both methods act as a mini climate model, or an AMIP simulation equivalent, on their own: they can calculate how SWUS precipitation will respond to a given SST pattern. A key difference between the two methods also lies in how they are created: on the one hand, the GF only has knowledge of how the climate responds to individual patch perturbations forced in AGCM simulations. These patch perturbations may be unrealistic and unrepresentative of the actual SST variability of the climate system. On the other hand, the CNN is trained from realistic patterns of SST variability from climate model output, though with the caveat that these patterns may be wrong; it has knowledge of the pattern of SST and identifies which SST regions are most helpful in predicting SWUS precipitation. This is an advantage of the CNN method. However, the GF is advantageous in that its sensitivity map represents physically meaningful regions for SWUS precipitation changes, since the GF is calculated from AGCM simulations that capture the dynamical response of the climate system to a given patch perturbation. In other words, the GF is informed by the governing equations of the atmosphere and causality can be directly assessed. The CNN instead could highlight an SST region as being important for SWUS precipitation changes simply due to a statistical relationship with no physical explanation.

In this study, we first detail the GF and CNN methods (Section 4.2) and then compare their sensitivities (Section 4.3.1). While both methods have predictive skill in SWUS precipitation, they identify different SST regions for being most important for SWUS precipitation changes. The GF highlights the relevance of the Central Pacific and Caribbean for SWUS precipitation (Figure 4.1a), which is backed by theory and modeling studies (e.g., Redmond and Koch 1991;

Evans et al. 2022; Hu et al. 2021), while the CNN method highlights the South-Central Pacific, which could be a new region for SWUS precipitation sensitivity (Figure 4.1b). We then validate the sensitivity of SWUS precipitation to the South-Central Pacific through physical reasoning: we use the XAI map to inform a perturbed AGCM simulation set up in a similar way to the GF patch simulations (Section 4.3.2). We find that SST changes in both regions affect the northern subtropical Pacific jet that controls how much precipitation the SWUS receives. This is the first study to our knowledge that uses a CNN and XAI to inform an AGCM simulation setup to prove the physical connection or causality between the predictor and predictand. We also document the potential influence of the South-Central Pacific on SWUS precipitation via a cross-equatorial atmospheric bridge (as in Mamalakis et al. 2018), which could improve predictability of SWUS precipitation on long timescales.

4.2 Methods

4.2.1 The Green's Function

We derive a precipitation GF following the approach in Alessi and Rugenstein (2023) who calculated top-of-atmosphere radiation and temperature GFs. Barsugli and Sardeshmukh (2002) previously developed a precipitation GF to analyze SWUS precipitation sensitivity to patterns of SST, but their GF was produced solely from localized SST patch anomaly simulations in the Tropical Pacific, whereas here we apply patch perturbations to the whole ocean surface. Zhang et al. (2023) also produce a global-mean response precipitation GF in this way, though they do not analyze regional precipitation sensitivity. We note there is also an established protocol for deriving a GF from SST patch simulations for the Green's Function Model Intercomparison Project (GFMIP) (Bloch-Johnson et al. 2024), though our setup is slightly different here as our GF was created prior to the completion of the protocol.

We use the Max Planck Institute's (MPI) atmospheric model ECHAM v6.3 with a latitude x longitude grid of 96 x 192 to conduct our simulations (Stevens et al. 2013). We first performed a control simulation for 26 years with prescribed 1990-2009 averaged SST from the HadISST observed SST dataset (Rayner et al. 2003). All radiative forcings (GHG, aerosols) were held constant at year 2000 levels, following the approaches in Dong et al. (2019) and in GFMIP (Bloch-Johnson et al. 2024). We then ran 182 fixed-SST simulations with localized patches of anomalous SST applied to the HadISST averaged pattern that forced the control simulation. These patch simulations were branched from the sixth year of the control simulation and ran for 20 years each. The SST patch anomalies follow a cosine hump as in Barsugli and Sardeshmukh (2002) to avoid nonlinearities caused by unrealistic SST gradients:

$$\delta SST(x,y) = A\cos^2\left(\frac{\pi}{2}\frac{y-y_p}{y_w}\right)\cos^2\left(\frac{\pi}{2}\frac{x-x_p}{x_w}\right),$$

where A is the amplitude of the SST patch anomaly (+/- 4 K) (Zhou et al., 2017), subscript p denotes the center point of the patch, and subscript w denotes the half-width of the patch. y_w is 2150 km and x_w is 4300 km, so that the patches are 8600 km x 4300 km in size. We performed cool and warm patch simulations (91 each) to reduce the effects of some known temperature nonlinearities in deriving a GF (Williams et al. 2023). The 1 K outline of the patch perturbations are plotted in Figure B.2.1. We note that the setup used in Alessi and Rugenstein (2023) is novel in their use of equal-area patches, rather than patches developed based on latitude and longitude coordinates (Dong et al. 2019; Barsugli and Sardeshmukh 2002; Zhou et al. 2017; Barsugli and Sardeshmukh 2002). The equal-area patch approach was later adopted by the GFMIP protocol, given its more realistic response in higher latitudes where patches were too small in previous studies (Bloch-Johnson et al. 2024). The precipitation GF is then derived following the approach outlined by Dong et al. (2019) (Figure 4.1a).

The precipitation GF matrix (referred to as the Jacobian in Dong et al. (2019)) is made up of columns containing the sensitivity of precipitation at one model grid point (i) to changes in SST at all grid points around the world (j) ($\partial P_i/\partial SST_j$). The matrix size is then all model grid points x all model grid points (18,432 x 18,432). The diagonal of the matrix represents all local responses (how local SST changes affect precipitation at the same grid point), while the off-diagonal values represent all non-local responses. A regional GF merely cuts the original matrix to only the columns of the GF matrix (i) that represent the region of interest: for the SWUS region, the GF matrix shape becomes 40 x 18,432, representing how the precipitation at each SWUS model grid point (size 40) responds to SST changes at all model grid points (size 18,432). To calculate the 10-year average SWUS precipitation response to a global pattern of SST, this smaller GF matrix is matrix multiplied with the 10-year average SST pattern. The resulting matrix is then averaged by area-weight, providing the overall SWUS precipitation response to that pattern of SST.

4.2.2 CNN Architecture

Our main goal is to develop a CNN that is similar to the GF: given a pattern of 10-year averaged SST, we wish to reproduce 10-year averaged SWUS precipitation and to identify which SST regions are most important for the CNN's prediction. We note the CNN must have skill in predicting SWUS precipitation in order for its sensitivity to be meaningful. To train our CNN, we use SST and precipitation data from 70 members of the 100-member MPI Earth System Model Grand Ensemble (MPI-GE) historical and RCP8.5 scenarios (Maher et al. 2019), representing years 1850-2100. The data are first detrended and turned into anomalies by subtracting out the ensemble mean—since our main goal is to identify SWUS precipitation sensitivity, we do not train on the forced response. We then apply a 10-year sliding mean to both

SWUS precipitation and SST anomaly data. Instead of 250 years per ensemble member, there are now only 240 years, representing 10-year averaged data centered on the years 1855-2095. This is done for two reasons: 1) the precipitation GF is developed from the long-term equilibrium responses of all the patch simulations, so a fair comparison between the GF and the CNN would be a CNN that predicts SWUS precipitation based on equilibrium responses to long-term SST patterns, and 2) we focus on long-term averages in this study, rather than subseasonal to seasonal predictability, as in other NN studies (Mayer and Barnes 2021; Arcodia et al. 2023).

We develop a CNN for a supervised regression task that is trained on the detrended SST pattern of 60 ensemble members, for a total of 14,400 training samples (60 members x 240 10-year averaged years). We use 5 ensemble members for validation and 5 ensemble members for testing. The CNN architecture is shown in Figure 4.2 and contains nine layers total: an input layer, three convolutional layers each followed by a max pooling layer, and then two dense layers after a flattening of the data, plus a final dense layer providing the prediction of SWUS precipitation. The input layer is a detrended SST anomaly map with size 96 x 192 (model grid point size for the atmospheric component of MPI Earth System Model). We employ 32 kernels with size 5 x 5 for all three convolutional layers, and we use the tanh activation function for both the convolutional and the dense layers. The max pooling layers are size 2 x 2, so that after the first max pooling, the size of the SST map becomes 48 x 96 (x 32 for each kernel), then after the second max pooling 24 x 48, and after the third max pooling 12 x 24, followed by a flattening of the data for the three dense layers. We also employ sample weighting in order for the model to perform slightly better for extreme values. Specifically, the weighting of precipitation samples less than -0.30 mm day^{-1} and greater than 0.30 mm day^{-1} were given a weighting of 2, while the

remaining precipitation samples were given a weighting of 1. The loss curve for the CNN is shown in Figure C.1.1.

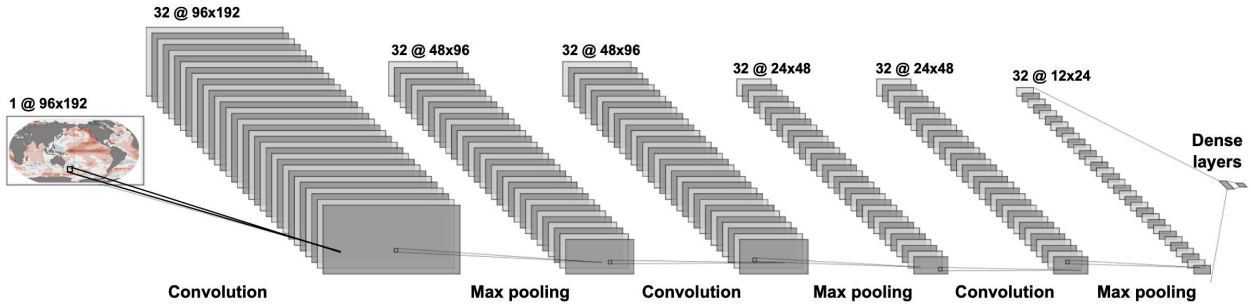

Figure 4.2. Schematic representation of the CNN. The input layer is a detrended SST anomaly map representing one year from one ensemble member. The dense layers are size 16x1 and 8x1.

We evaluate the CNN by comparing the CNN 10-year averaged SWUS precipitation to the AOGCM 10-year averaged SWUS precipitation output (Figure 4.3a). The CNN does well in predicting AOGCM precipitation, although the CNN fails to reproduce extreme values of long-term SWUS precipitation, despite the use of sample weighting and several tests with other activation functions. We note that there was slight improvement in the validation loss after including sample weights. Again, our goal here is to reproduce the AOGCM precipitation output and identify what SST regions SWUS precipitation is most sensitive to according to the CNN. Since the CNN is able to reproduce long-term SWUS precipitation averages, we believe the XAI map to be somewhat meaningful, although this exercise would not work if the CNN had no skill in predictability. The CNN further does better in predicting long-term SWUS precipitation given the pattern of SST compared to the GF (example ensemble member in Figure 4.3b). Specifically, the CNN has a correlation of 0.53 between the prediction and AOGCM output across the 5 testing ensemble members, while the GF has a correlation of 0.38 between the prediction and AOGCM output for the same input SST data. We then use an XAI method called gradients to

derive a CNN SWUS precipitation sensitivity map. The gradients XAI map shows the sensitivity of SWUS precipitation to SST regions, rather than the relevance of each SST grid point as in other XAI methods such as integrated gradients and layer-wise relevance propagation ().

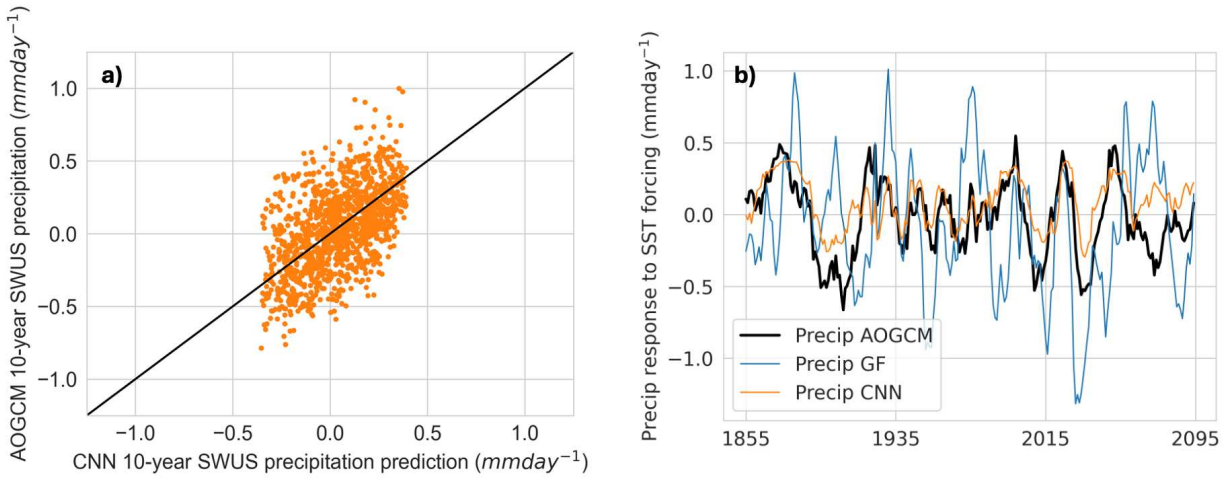

Figure 4.3. a) The CNN 10-year averaged SWUS precipitation prediction compared to the 10-year averaged AOGCM SWUS precipitation output for all 5 testing ensemble members (5 members x 240 years). b) The 10-year averaged SWUS precipitation prediction according to the AOGCM (black), GF (blue), and CNN (orange), for one testing ensemble member. The precipitation prediction for each method is in response to the same SST forcing.

4.3 Results

4.3.1 Comparing the GF and CNN Sensitivity Maps

The GF map in Figure 4.1a qualitatively confirms the precipitation GF work done by Barsugli and Sardeshmukh (2002), corroborates the well-documented teleconnection between the Central Pacific and the SWUS (Hoerling et al. 1997; Redmond and Koch 1991), and backs empirical orthogonal analysis of SST and SWUS precipitation (Hu et al. 2021). We note that the GF identifies the Caribbean as an important predictor region for SWUS precipitation, which has not been documented. This sensitivity originates in the lack of northward moisture transport from the Caribbean to the SWUS when the SST in this region is warmed, resulting in decreased

SWUS precipitation. The warming in the Caribbean causes moisture and convection to remain over the Caribbean instead of moving northward into the SWUS during the months of the North American monsoon (see Figure B.2.4).

Following Alessi and Rugenstein (2024), we tune the GF to account for the nonlinearities of the climate system that the GF does not capture and to reproduce SWUS precipitation output from the historical and RCP8.5 MPI-GE ensemble-mean simulations (not shown). Since the GF likely exaggerates the precipitation response to a warming in the Central Pacific due to spatial nonlinearities (Williams et al. 2023), we subtract a small number (8.6×10^{-5}) from each index of the GF matrix. More details on the tuning of the GF can be found in Alessi and Rugenstein (2024). We note that tuning of the GF has also been implemented in Alessi and Rugenstein (2023) and Dong et al. (2019) for global-mean radiation.

While the CNN XAI gradients sensitivity map also highlights the importance of the Central Pacific in predicting SWUS precipitation (Figure 4.1b), it instead finds the South-Central Pacific as having the most importance for predicting SWUS precipitation. In fact, the CNN finds the South-Central Pacific important for both positive and negative relationships between SST and SWUS precipitation: the dark green regions indicate a positive relationship where an increase in SST would result in an increase in precipitation, while the dark brown regions indicate a negative relationship where an increase in SST would result in a decrease in SWUS precipitation. From our knowledge, this teleconnection between the South-Central Pacific and the SWUS is a new finding. However, we note that the SST regions highlighted by the CNN as most important for SWUS precipitation prediction on long timescales are similar to the SST regions with a high positive and high negative linear correlation between SST and SWUS precipitation, as shown in Figure 3.1c in Chapter 3. We trained a separate CNN model using only

linear activation functions and found results closer to Figure 2c in Chapter 2 and with a lower skill than the CNN trained with the tanh activation function (not shown). The higher skill and slightly different XAI map pattern indicate some advantage in using the nonlinear CNN method over the linear correlation method.

It is also possible the CNN is overfitting to certain SST regions—a CNN merely looks for SST regions with a high statistical relationship to SWUS precipitation, perhaps with no physical explanation or mechanism behind the relationship. According to the loss curve (Figure C.1.1), there does not appear to be significant overfitting, with the two curves converging by the last training epoch. The training loss curve is greater than the validation loss curve because of the addition of sample weighting—the training will have a higher loss because it is also considering the higher weight of extreme precipitation values, which is not applied to the validation portion of training. To test for overfitting, we trained an additional CNN model on the same 10-year averaged SST maps but set the SST to zero for the most important regions according ot the original XAI map. If the CNN can reproduce SWUS precipitation *without* knowledge of the South-Central Pacific SST pattern just as well as *with* knowledge of the South-Central Pacific SST pattern, then this could be an indication of the model overfitting. To do this, we set all Southern Hemisphere SST values in the training, validation, and testing data to zero. We found this CNN model to have a higher loss and lower predictive skill for long-term SWUS precipitation. Interestingly, the XAI gradients sensitivity map for this model shows most predictability originating around the Equator in the Central Pacific—the model seems to attempt to highlight SST regions that are as close as possible to the original XAI map. For these reasons, we believe the model is not overfitting to the South-Central Pacific, and therefore there could be

a physical reason for why the CNN highlights the South-Central Pacific as being important for SWUS precipitation prediction.

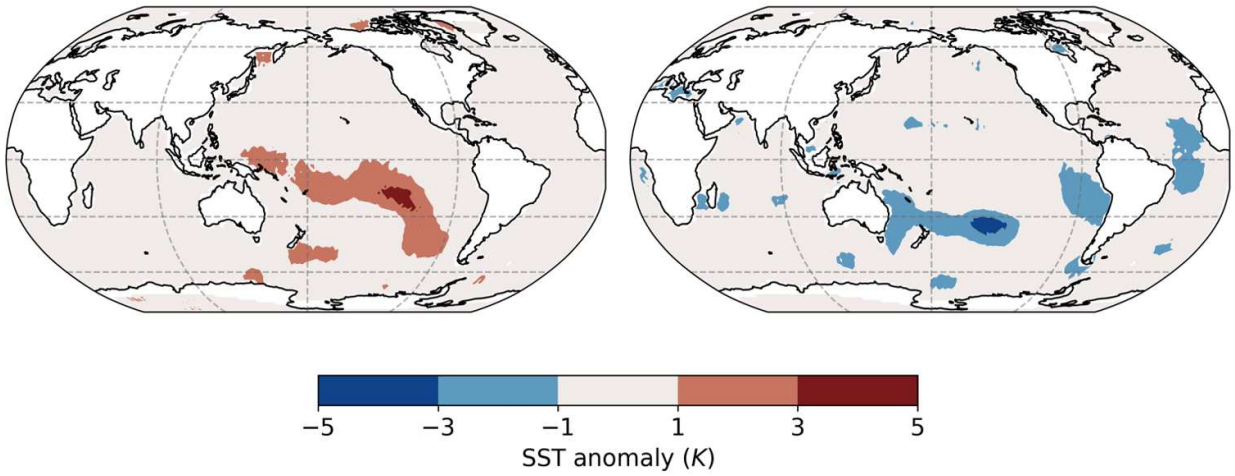

Figure 4.4. SST anomaly applied to the two XAI-informed AGCM simulations.

4.3.2 XAI-informed AGCM Simulations

A high correlation or relationship between SST and SWUS precipitation does not indicate causation. In order to prove a physical mechanism underpinning the supposed teleconnection between the South-Central Pacific and SWUS according to the CNN, we run two XAI-informed AGCM simulations using the ECHAM atmospheric model. Both simulations involve adding SST anomalies to the control SST pattern used to create the patch simulations for the GF. However, instead of a cosine hump anomaly as for a GF patch simulation, the SST patch is instead the same shape as the green or brown region in the XAI sensitivity map (Figure 4.1b). We use the AGCM simulation, with an XAI-informed SST perturbation, to explain the dynamical mechanism relating the South-Central Pacific SST to SWUS precipitation. Since the CNN looks to SST changes in the green or brown regions to change its SWUS precipitation prediction, our hypothesis is that the northern subtropical Pacific jet that delivers precipitation to the SWUS

shifts north of the SWUS or over the SWUS based on warming in the brown or green regions, respectively.

The simulations are setup using the same approach as the GF patch simulations. In the first simulation, we seek to understand the dynamical mechanism for the how the green SST regions in the XAI sensitivity map influence SWUS precipitation in a positive relationship ($AGCM_{Green}$). We first remove all negative (brown) values from the XAI sensitivity map and divide the map by the maximum value. We then multiply the map by 4, so that the largest SST anomaly is 4.0 K, similar to the GF patch simulations (Figure 4.4a). For the second simulation, we instead discern the dynamical mechanism leading to a negative relationship between the brown SST regions in the XAI sensitivity map and SWUS precipitation ($AGCM_{Brown}$). The same process is done for this simulation as in $AGCM_{Green}$ except in the opposite direction: all the positive (green) values are removed from the XAI map and then the map is divided by the minimum value. We then multiply the map by -4, resulting in the largest absolute SST anomaly being -4 K (Figure 4.4b). These simulations are branched from the sixth year of the control simulation, the same as the GF patch simulations, and run for 11 years each. We discard the first year of simulation in for the model to spin-up in response to the SST anomaly. Based on the setup of each simulation, we expect both $AGCM_{Green}$ to $AGCM_{Brown}$ to increase precipitation in the SWUS, given the positive and negative relationship, respectively, between SST and SWUS precipitation for the green and brown XAI sensitivity map regions.

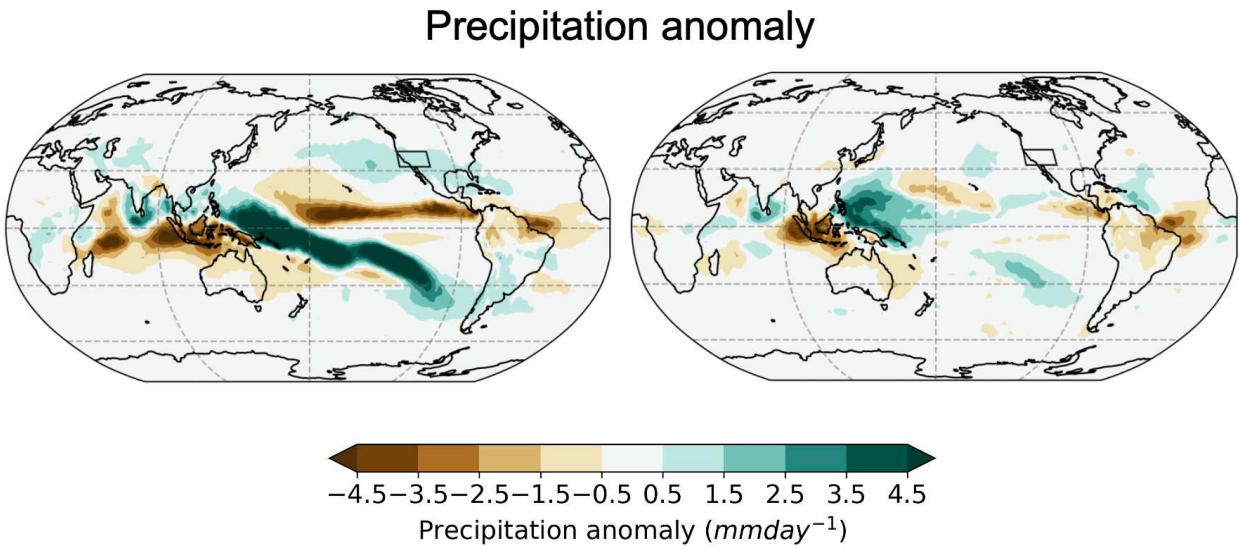

Figure 4.5. 10-year averaged precipitation anomaly for the $AGCM_{Green}$ simulation (left) and the $AGCM_{Brown}$ simulation (right).

$AGCM_{Green}$ leads to a 94% increase in precipitation in the SWUS compared to the control simulation averaged over the ten years of simulation (2.33 mm day^{-1} compared to 1.21 mm day^{-1}), while there is a 20% increase in SWUS precipitation from the $AGCM_{Brown}$ simulation (1.44 mm day^{-1} compared to 1.21 mm day^{-1}) (Figure 4.5). This change in precipitation confirms influence of the South-Central Pacific on SWUS precipitation as identified by the CNN model. Both AGCM simulations have a similar response to the XAI-informed SST patch anomaly, though it is more muted in $AGCM_{Brown}$ (Figure 4.6). Increased SST in the South-Central Pacific triggers more convection south of the Equator, represented by more rising air (lower ω values; Figure 4.6 top row). This response is realistic: the intertropical convergence zone typically shifts towards the hemisphere with warmer SSTs where greater convergence occurs (Broccoli et al. 2006; Goswami et al. 1984). In the process, more energy is transferred to the opposite, cooler atmosphere via the ascending and outward branches of the Hadley Cell, which allows the planet to maintain radiative equilibrium. We find both the ascending (represented by ω in the top row

of Figure 4.6) and upward branches (represented by v-wind in the middle row of Figure 4.6) strengthen when a warming is applied to the South-Central Pacific. This additional northward v-wind then results in anomalous subsidence in the Northern Hemisphere Pacific basin, exciting midlatitude Rossby waves in such a way where the northern subtropical Pacific jet increases in strength and shifts south (represented by the 850 mb u-wind map in the bottom row of Figure 4.6). This additional strength in the prevailing westerlies allows for more precipitation to flow into the SWUS via the northern subtropical Pacific jet. We confirm the presence of a stronger, more southerly northern subtropical Pacific jet in analyzing the 500 mb anomaly and absolute value maps for $AGCM_{Green}$ (Figure 4.7). The trough is noticeably deeper in $AGCM_{Green}$ compared to the control simulation over the North Pacific Ocean, allowing for more moisture to be brought into the SWUS from the Tropical Pacific.

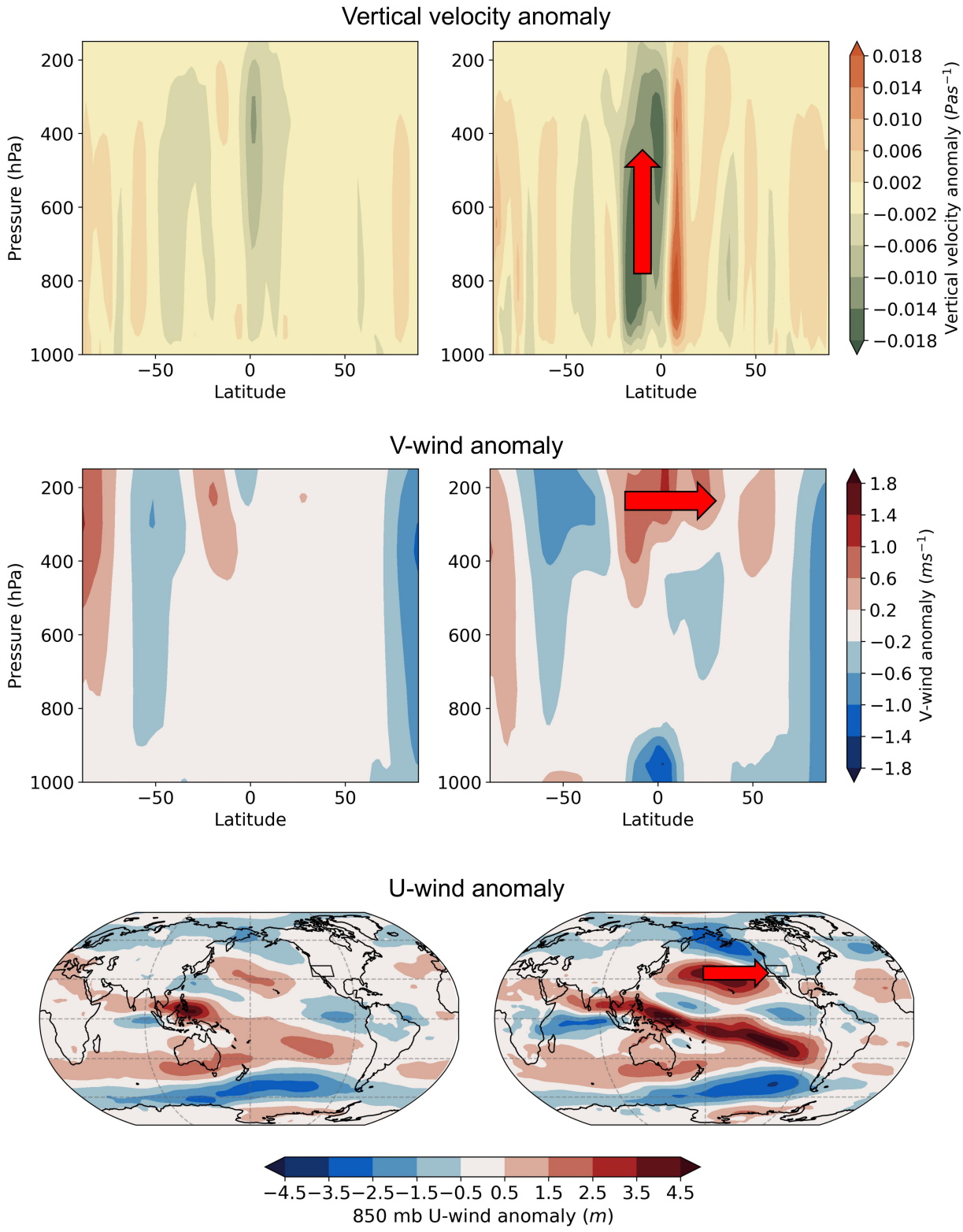

Figure 4.6. 10-year averaged ω (top row) and v-wind (middle row) zonal-mean anomaly for $AGCM_{Brown}$ (left column) and $AGCM_{Green}$ (right column). The zonal mean is only taken over the

Pacific basin (120°E to 285°E). U-wind at 850 mb anomaly maps (bottom row) for $AGCM_{Brown}$ (left column) and $AGCM_{Green}$ (right column).

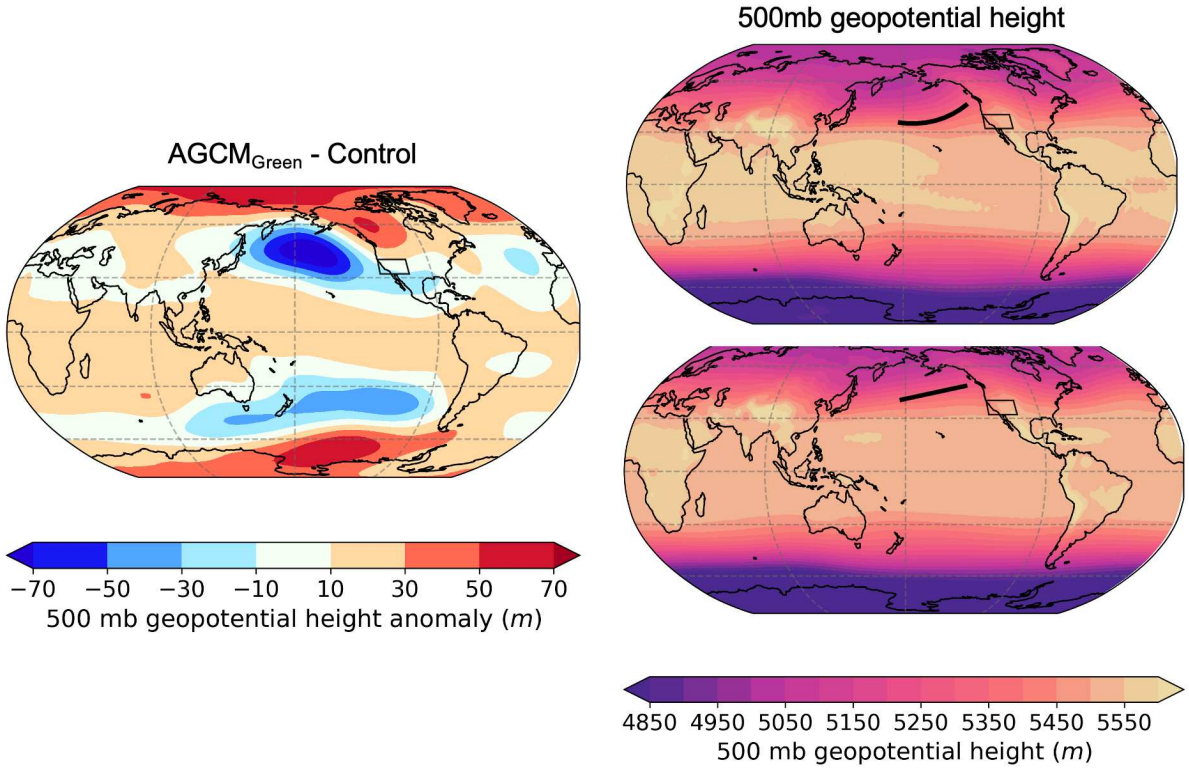

Figure 4.7. 10-year averaged 500 mb geopotential height anomaly for $AGCM_{Green}$ (left). The 10-year averaged 500 mb geopotential height in the $AGCM_{Green}$ simulation (top) and the control simulation (bottom). The black line in the right figures is to accentuate the trough which exhibits more curvature in $AGCM_{Green}$ than the control simulation.

Through a CNN approach, we identify a new region of SST influence on SWUS precipitation on long timescales. We run XAI-informed AGCM simulations to diagnose the dynamical and causal pathway for the South-Central Pacific's influence on SWUS precipitation. This approach is novel in that it forces an AGCM with an SST anomaly from a CNN XAI map in order to identify dynamical mechanisms underpinning the CNN's sensitivity.

4.4 Discussion

There are other studies that highlight Southern Hemisphere SSTs as having an influence on SWUS precipitation, mainly through the Pacific Decadal Oscillation (Dai 2013; Cayan et al. 1998). Mamalakis et al. (2018) is the only other study to our knowledge that diagnoses a specific region in the Southern Hemisphere, SST changes near New Zealand, as having an impact on SWUS precipitation that is unconnected from the major oscillations of internal variability. To be sure the South-Central SST region in our study is not related to the PDO, we calculate the correlation between SST at each grid point and the average SST for a boxed region where the XAI sensitivity peaks for a positive relationship (darkest green region in Figure 4.1b) (Figure 4.8; 40°S to 30°S, 120°W to 90°W). The SSTs in this region do not seem to correlate highly with other regions, including where we expect the PDO to be; this would be represented by a more pronounced correlation signature stretching, or darker colors in Figure 4.8, from the ENSO region to the North Pacific. We note there is some relationship between the ENSO region and the boxed region in Figure 4.8. This is interesting because we know the ENSO SST region is important for SWUS precipitation variability, and yet the CNN does not highlight the region at all. Perhaps there is some relationship between ENSO and SWUS precipitation, but the model only looks at the South-Central Pacific, given these low to moderate correlation values. However, ECHAM does not simulate the precipitation response perfectly between the ENSO region and SWUS precipitation (Figure 10 in Stevens et al. 2013), which could be a major caveat of the analysis here.

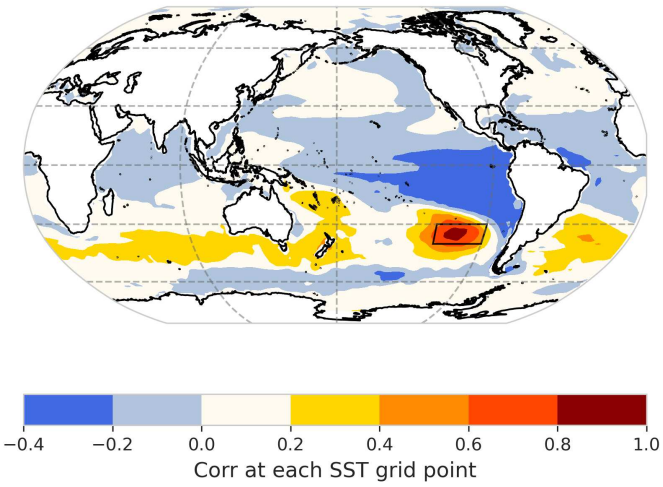

Figure 4.8. Correlation between SST at each grid point and the averaged SST of the boxed region in the figure (40°S to 30°S, 120°W to 90°W). This region corresponds to the largest values in Figure 4.1b.

This analysis is only done using the MPI atmospheric model, ECHAM. AGCMs have different responses to SST patterns based on the structural differences between models (e.g., different dynamical core, different parameterizations). We did separately train a CNN on both SST and precipitation from the Canadian AOGCM, CanESM, and the Japanese AOGCM, MIROC. The XAI maps for these CNNs highlighted different regions for SWUS precipitation sensitivity, mainly the North Pacific, which is more of a reflection of the PDO signature. The fact that different models highlight different SST regions for SWUS precipitation sensitivity on long timescales reflects the scale of this problem: climate models struggle to agree qualitatively on the precipitation response to anthropogenic warming, i.e. some models predict a wetting of the SWUS while others predict a drying, and there is much model difference between sensitivity. However, a comparison between the ECHAM ENSO precipitation response and the observed ENSO response shows significant agreement (Stevens et al. 2013), which argues ECHAM may be more realistic than others. Our GF sensitivity, however, agrees qualitatively with other

models: the AGCM used in Barsugli and Sardeshmukh (2002), as well as the precipitation GF used in Zhang et al. (2023) (regional GF through communication). This could be a reflection of similar response to applied SST forcings across models, though more work needs to be done analyzing the cross-model sensitivity.

We also trained a CNN on SST and SWUS precipitation on annual timescales. This CNN identified the same region, the South-Central Pacific, as being important for SWUS precipitation prediction. This sensitivity across timescales corroborates the analysis in Dettinger et al. (1998), which found that spatial Empirical Orthogonal Functions of zonally averaged precipitation over western North America correlated with SST on short (3-7 years) and long timescales (7+ years). The results of this study could then be extrapolated to shorter timescales, though internal atmospheric variability will have a larger impact on SWUS precipitation changes compared to SST forcing as the period of analysis decreases (Seager et al. 2015).

4.5 Conclusions

It is well established that the evolution of the SST pattern drives SWUS precipitation changes on longer timescales (Dettinger et al. 1998; Cayan et al. 1998; Alessi and Rugenstein 2024). In this study, we analyze the sensitivity differences between two methods of SWUS precipitation response to SST forcing: the GF and a CNN. A GF is derived from many AGCM simulations with localized SST anomaly patch forcings. It is realistic in its SWUS precipitation response to these patch forcings, since the precipitation can be attributed to and dynamically explained by a certain SST forcing. However, the GF is a linearization of SWUS precipitation response to an SST forcing. Further, its sensitivity may be unrealistic since it is calculated from simulations with potentially unrealistic SST patch forcings. A CNN instead trains on the pattern of SST to predict SWUS precipitation. It is more realistic than the GF in that it can identify

nonlinear relationships between the forcing and the response, and it makes its predictions from knowledge of realistic, though potentially incorrect, SST patterns. However, the CNN could highlight SST regions that are statistically related to SWUS precipitation with no apparent dynamical explanation.

The two methods identify slightly different regions as being most responsible for driving SWUS precipitation changes on long timescales. The GF highlights the Central Pacific, while the CNN highlights the South-Central Pacific. The theory behind the Central Pacific's influence on SWUS precipitation is well documented, while the South-Central Pacific as a driver of SWUS precipitation is a new finding. To justify the CNN method and identify the physical mechanism underpinning the relationship between South-Central Pacific SSTs and SWUS precipitation, we run two AGCM simulations that are informed by the CNN's XAI map. In one simulation, we apply a warm SST anomaly to the regions in the XAI map with a positive relationship between local SST and SWUS precipitation (green in Figure 4.1b). In the other simulation, we apply a cool SST anomaly to the regions in the XAI map with a negative relationship between local SST and SWUS precipitation (brown in Figure 4.1b). As expected based on the relationship identified in the XAI map, both simulations lead to an increase in SWUS precipitation (Figure 4.5a). The AGCM simulation explains this relationship: a warming of the South-Central Pacific with a positive relationship to SWUS precipitation shifts the intertropical convergence zone south, leading to a stronger Hadley Cell circulation north of this convergence (greater vertical motion and greater northward v-wind anomalies in Figure 4.6). This leads to a subsidence anomaly in the North Pacific, which excites the Rossby wave in such a way to develop a deeper trough in the North Pacific, positioning the northern subtropical Pacific jet over the SWUS (Figure 4.7), which has the effect of bringing in more precipitation to the region (Figure 4.5b).

Understanding the sensitivity of SWUS precipitation to the pattern of SST evolution is critical as anthropogenic climate change persists. This allows water resource management to plan for long-term precipitation changes with knowledge of the SST pattern. However, there is the added problem of AOGCMs erroneously reproducing the observed pattern of SST evolution. Climate scientists must continue developing potential future scenarios and storylines of the SST pattern that are backed by theory (Alessi and Rugenstein 2024, 2023), which may lead to greater uncertainty in projections of SST. However, with increased knowledge of the sensitivity of SWUS precipitation the pattern of SST, and with a better understanding of the SST pattern evolution, the SWUS can mitigate and adapt to climate projections accordingly.

CHAPTER 5: CONCLUSION

5.1 Summary

In this dissertation, we assess how future model error in SST trends affect climate projections. In Chapter 2, we first demonstrate through a Green's function (GF) approach that the pattern of SST can substantially increase the total uncertainty of global-mean warming and influence the rate of warming. For example, if the West Pacific warms slightly less than what AOGCMs predict over the next few decades, the globe would warm 0.5 K more than current model projections. By 2085, total model uncertainty of global-mean temperature increases by 40% when considering possible combinations of idealized SST trend pattern scenarios that differ from AOGCMs but are inspired by historical model error. If we constrain future SST trends to start from observations and reverse the East Pacific cooling trend, the globe may warm 60% faster over the next few decades than what AOGCMs predict. Critically, this reversal of the East Pacific cooling trend already appears to be a reality (Rugenstein et al. 2023; Loeb et al. 2021; Andrews et al. 2022), potentially influencing global-mean warming today. If climate scientists fail to account for the potential error in future SST pattern trends, there could be a false sense of security or doubt in the overall skill of AOGCMs. For example, if a pattern of SST develops unpredicted by AOGCMs, it could cause the Earth to warm slower, potentially having the effect of halting the world's effort in mitigating and adapting to climate change. However, this scenario could be quickly followed by a switch to an SST pattern, again one not predicted by AOGCMs, that induces abrupt warming. This would be a shock to the world's governments and their response efforts if they were not sufficiently warned of the possibility of different SST pattern scenarios that are outside the realm of AOGCM simulation. It is critical for climate scientists to further develop physically meaningful SST pattern scenarios that are inspired by theory or

observations and outside the realm of AOGCM simulation to better understand the uncertainty of global-mean warming.

In Chapter 3, we focus on the effect of future model error in SST pattern trends on SWUS precipitation projections. The cooling trend in the Central and East Pacific, unpredicted by AOGCMs, may have contributed to heightened drought conditions over the past few decades in the SWUS (Delworth et al. 2015; Lehner et al. 2018). Using a GF approach, we first confirm the teleconnection between the Equatorial Pacific SST trend pattern and SWUS precipitation trends. We find that a modest redistribution of SST in the Central Pacific or Caribbean could lead to a wetting or drying of the SWUS, highlighting the extreme sensitivity of SWUS precipitation to the SST pattern trend. This sensitivity complicates prediction of future SWUS drought, given that an SST warming of the West Pacific, for example, unpredicted by AOGCMs results in a wetting of the SWUS. When constraining future SST trends to start from observations, a wetting over the SWUS would occur if the Central and East Pacific cooling trend reverses. However, we note that internal variability plays a larger role in explaining interannual SWUS precipitation variance, i.e., a warmer Central Pacific could still have a string of dry years depending on the state of the atmospheric circulation. Furthermore, our analysis only considers changes in precipitation rather than changes in hydroclimate. Even if precipitation increases in the SWUS, drought conditions could become more common in the future given higher evaporative demand and drier soils.

In Chapter 4, we further diagnose SWUS precipitation sensitivity to different patterns of SST on long timescales (>7+ years). We compare the GF approach from Chapter 3 to a convolutional neural network approach, which identifies nonlinear relationships between SST and SWUS precipitation. The two methods, both having advantages and disadvantages (see

Chapter 4 for discussion), identify different regions as being most responsible for driving changes in SWUS precipitation. The GF highlights the Central Pacific, while the CNN highlights the South-Central Pacific. The CNN identifies statistical relationships between SST and SWUS precipitation with potentially no physical explanation with their connection. However, to explain dynamically the South-Central Pacific SST to SWUS precipitation teleconnection, we force an AGCM with SST anomalies informed by an explainable Artificial Intelligence (XAI) method. We find that a warming of the South-Central Pacific leads to an increase in SWUS precipitation through an atmospheric bridge via the intertropical convergence zone, which shifts the northern subtropical jet over the SWUS, bringing with it more precipitation. This result suggests a physical mechanism underpins the nonlinear statistical relationship between SWUS precipitation and South-Central Pacific SSTs identified by the CNN.

5.2 Future Work

There are many avenues of future work that stem from this dissertation. Following the methods in Chapter 2 and 3, we could apply the SST pattern scenarios and storylines to the CNN developed in Chapter 4. Because the CNN identifies SSTs in the South-Central Pacific as the most important in affecting SWUS precipitation on long timescales, forcing the CNN with the SST scenarios in Chapter 3, both the idealized SST changes (e.g., increasing SST in the Central Pacific) and constraining SST evolution from observations with a reversing of the East Pacific trend, could produce different results. There is much less SWUS precipitation sensitivity to changes in Caribbean SST in the CNN compared to the GF (Figure 4.1 in Chapter 4). This could reflect the GF being unrealistic in its SST perturbation in the Caribbean. For example, perhaps a large positive SST anomaly is unlikely in the Caribbean, which shifts convection from the SWUS to the Caribbean, without similar positive SST anomalies in nearby regions or the whole

tropics. Therefore, we hypothesize little change in SWUS precipitation given the idealized SST scenarios in the Caribbean from Chapter 3. For the storyline approach where we constrain SST projections to start from observations, we expect a similar result to Chapter 3: the CNN still has plenty of sensitivity to the Central Pacific in general where significant warming in the SST scenario occurs in order to catch up to AOGCMs.

There is also much work to be done involving the GF. Over the last few years, I helped co-lead the Green's Function Model Intercomparison Project, and the protocol paper was recently published (Bloch-Johnson, Rugenstein, Alessi et al. 2024). The GF could be a breakthrough in comparing climate responses (for many variables) across models. For example, a precipitation GF derived from localized SST anomaly experiments from different models would highlight different SST regions for precipitation sensitivity. This could be done on the global-mean or regional scale. Regional precipitation changes are especially inconsistent between AOGCMs; if we can first identify the SST regions most important for regional precipitation across models, we could then undergo a dynamical analysis of why these models produce the results they do, perhaps highlighting the different dynamical cores or parameterizations in these models. Once it is clear what is driving differences between models, the GF could be key in advising climate projections, for example those issued by the Intergovernmental Panel on Climate Change. Uncertainty in projections partly originates in model spread—with GFMIP, scientists will be better equipped to explain this uncertainty based on the different sensitivities of AOGCMs to forcings.

Perhaps the most important question is: why are AOGCMs failing in simulating the pattern of SST evolution? And further: is the discrepancy between AOGCMs and observations a reflection of the range of AOGCM internal variability being too small or an issue with AOGCM

response to GHG forcing? We demonstrate that correctly modeled SST trend patterns are critical for both global-mean temperature projections and SWUS, and other regional, precipitation projections. There is evidence to suggest that improved and higher resolution modeling of ocean-atmosphere interaction may reduce mean-state biases in SST (Chang et al. 2020), which could be responsible for the erroneous SST trends (Delworth et al. 2015; Seager et al. 2019). However, these high-resolution modeling endeavors are computationally expensive and have limited simulation length (Schneider et al. 2017). Furthermore, climate scientists must be careful in running more complex simulations merely to reproduce observations. Getting the "right answer for the wrong reason" or not understanding the theory behind why a model is producing certain results could be detrimental to the field as we try to balance larger observational and modeling datasets with theoretical understanding (Emanuel 2020). Another potential avenue to better simulate the climate system could be using deep learning approaches that represent microscale processes in the ocean and atmosphere, which would drastically cut the computational cost of high-resolution modeling (Rasp et al. 2018). Critically, these approaches can be interpretable, encapsulate physics, and perhaps even highlight new physical relationships in the climate system, as we do in Chapter 4 (Zanna and Bolton 2020). There is also the additional approach of running larger ensembles to better capture the full range of internal variability of the climate system, but if these models are inherently wrong in their SST response to GHG or aerosol forcing, then perhaps this path may not be ideal. For now, climate scientists must develop physically meaningful SST pattern scenarios that are unpredicted by AOGCMs to capture the true range of projection uncertainty from anthropogenic forcing or internal variability of the climate system.

REFERENCES

Alessi, M. J., and M. A. A. Rugenstein, 2023: Surface Temperature Pattern Scenarios Suggest Higher Warming Rates Than Current Projections. *Geophysical Research Letters*, **50**, e2023GL105795, https://doi.org/10.1029/2023GL105795.

——, and M. A. A. Rugenstein, 2024: Potential near-term wetting of the Southwestern United States if the Eastern and Central Pacific cooling trend reverses. https://doi.org/in review.

Andrews, T., and M. J. Webb, 2018: The Dependence of Global Cloud and Lapse Rate Feedbacks on the Spatial Structure of Tropical Pacific Warming. *Journal of Climate*, **31**, 641–654, https://doi.org/10.1175/JCLI-D-17-0087.1.

——, J. M. Gregory, and M. J. Webb, 2015: The Dependence of Radiative Forcing and Feedback on Evolving Patterns of Surface Temperature Change in Climate Models. *Journal of Climate*, **28**, 1630–1648, https://doi.org/10.1175/JCLI-D-14-00545.1.

——, and Coauthors, 2018: Accounting for Changing Temperature Patterns Increases Historical Estimates of Climate Sensitivity. *Geophysical Research Letters*, **45**, 8490–8499, https://doi.org/10.1029/2018GL078887.

——, and Coauthors, 2022: On the Effect of Historical SST Patterns on Radiative Feedback. *Journal of Geophysical Research: Atmospheres*, **127**, e2022JD036675, https://doi.org/10.1029/2022JD036675.

Arcodia, M. C., E. A. Barnes, K. J. Mayer, J. Lee, A. Ordonez, and M.-S. Ahn, 2023: Assessing decadal variability of subseasonal forecasts of opportunity using explainable AI. *Environ. Res.: Climate*, **2**, 045002, https://doi.org/10.1088/2752-5295/aced60.

Armour, K. C., 2017: Energy budget constraints on climate sensitivity in light of inconstant climate feedbacks. *Nature Clim Change*, **7**, 331–335, https://doi.org/10.1038/nclimate3278.

——, C. M. Bitz, and G. H. Roe, 2013: Time-Varying Climate Sensitivity from Regional Feedbacks. *Journal of Climate*, **26**, 4518–4534, https://doi.org/10.1175/JCLI-D-12-00544.1.

Ault, T. R., 2020: On the essentials of drought in a changing climate. *Science*, **368**, 256–260, https://doi.org/10.1126/science.aaz5492.

——, J. S. Mankin, B. I. Cook, and J. E. Smerdon, 2016: Relative impacts of mitigation, temperature, and precipitation on 21st-century megadrought risk in the American Southwest. *Science Advances*, **2**, e1600873, https://doi.org/10.1126/sciadv.1600873.

Barron, J. A., S. E. Metcalfe, and J. A. Addison, 2012: Response of the North American monsoon to regional changes in ocean surface temperature. *Paleoceanography*, **27**, https://doi.org/10.1029/2011PA002235.

Barsugli, J. J., and P. D. Sardeshmukh, 2002: Global Atmospheric Sensitivity to Tropical SST Anomalies throughout the Indo-Pacific Basin. *Journal of Climate*, **15**, 3427–3442, https://doi.org/10.1175/1520-0442(2002)015<3427:GASTTS>2.0.CO;2.

Beobide-Arsuaga, G., A. Düsterhus, W. A. Müller, E. A. Barnes, and J. Baehr, 2023: Spring Regional Sea Surface Temperatures as a Precursor of European Summer Heatwaves. *Geophysical Research Letters*, **50**, e2022GL100727, https://doi.org/10.1029/2022GL100727.

Bloch-Johnson, J., and Coauthors, 2024: The Green's Function Model Intercomparison Project (GFMIP) Protocol. *Journal of Advances in Modeling Earth Systems*, **16**, e2023MS003700, https://doi.org/10.1029/2023MS003700.

Broccoli, A. J., K. A. Dahl, and R. J. Stouffer, 2006: Response of the ITCZ to Northern Hemisphere cooling. *Geophysical Research Letters*, **33**, https://doi.org/10.1029/2005GL024546.

Bureau of Reclamation, 2024: 5-Year Probabilistic Projections. https://www.usbr.gov/lc/region/g4000/riverops/crss-5year-projections.html (Accessed April 22, 2024).

Carrillo, C. M., and Coauthors, 2022: Megadrought: A Series of Unfortunate La Niña Events? *Journal of Geophysical Research: Atmospheres*, **127**, e2021JD036376, https://doi.org/10.1029/2021JD036376.

Cayan, D. R., M. D. Dettinger, H. F. Diaz, and N. E. Graham, 1998: Decadal Variability of Precipitation over Western North America. *Journal of Climate*, **11**, 3148–3166, https://doi.org/10.1175/1520-0442(1998)011<3148:DVOPOW>2.0.CO;2.

Ceppi, P., and J. M. Gregory, 2017: Relationship of tropospheric stability to climate sensitivity and Earth's observed radiation budget. *Proceedings of the National Academy of Sciences*, **114**, 13126–13131, https://doi.org/10.1073/pnas.1714308114.

——, F. Brient, M. D. Zelinka, and D. L. Hartmann, 2017: Cloud feedback mechanisms and their representation in global climate models. *WIREs Climate Change*, **8**, e465, https://doi.org/10.1002/wcc.465.

Chang, P., and Coauthors, 2020: An Unprecedented Set of High-Resolution Earth System Simulations for Understanding Multiscale Interactions in Climate Variability and Change. *Journal of Advances in Modeling Earth Systems*, **12**, e2020MS002298, https://doi.org/10.1029/2020MS002298.

Chemke, R., and L. M. Polvani, 2019: Opposite tropical circulation trends in climate models and in reanalyses. *Nat. Geosci.*, **12**, 528–532, https://doi.org/10.1038/s41561-019-0383-x.

Chung, E.-S., A. Timmermann, B. J. Soden, K.-J. Ha, L. Shi, and V. O. John, 2019: Reconciling opposing Walker circulation trends in observations and model projections. *Nat. Clim. Chang.*, **9**, 405–412, https://doi.org/10.1038/s41558-019-0446-4.

Coats, S., and K. B. Karnauskas, 2017: Are Simulated and Observed Twentieth Century Tropical Pacific Sea Surface Temperature Trends Significant Relative to Internal Variability? *Geophysical Research Letters*, **44**, 9928–9937, https://doi.org/10.1002/2017GL074622.

Cook, B. I., R. Seager, and J. E. Smerdon, 2014: The worst North American drought year of the last millennium: 1934. *Geophysical Research Letters*, **41**, 7298–7305, https://doi.org/10.1002/2014GL061661.

——, T. R. Ault, and J. E. Smerdon, 2015: Unprecedented 21st century drought risk in the American Southwest and Central Plains. *Science Advances*, **1**, e1400082, https://doi.org/10.1126/sciadv.1400082.

——, A. P. Williams, J. S. Mankin, R. Seager, J. E. Smerdon, and D. Singh, 2018: Revisiting the Leading Drivers of Pacific Coastal Drought Variability in the Contiguous United States. *Journal of Climate*, **31**, 25–43, https://doi.org/10.1175/JCLI-D-17-0172.1.

Cook, B. I., J. S. Mankin, A. P. Williams, K. D. Marvel, J. E. Smerdon, and H. Liu, 2021: Uncertainties, Limits, and Benefits of Climate Change Mitigation for Soil Moisture Drought in Southwestern North America. *Earth's Future*, **9**, e2021EF002014, https://doi.org/10.1029/2021EF002014.

Dai, A., 2013: The influence of the inter-decadal Pacific oscillation on US precipitation during 1923–2010. *Clim Dyn*, **41**, 633–646, https://doi.org/10.1007/s00382-012-1446-5.

Delworth, T. L., F. Zeng, A. Rosati, G. A. Vecchi, and A. T. Wittenberg, 2015: A Link between the Hiatus in Global Warming and North American Drought. *Journal of Climate*, **28**, 3834–3845, https://doi.org/10.1175/JCLI-D-14-00616.1.

Deser, C., M. A. Alexander, S.-P. Xie, and A. S. Phillips, 2010: Sea Surface Temperature Variability: Patterns and Mechanisms. *Annual Review of Marine Science*, **2**, 115–143, https://doi.org/10.1146/annurev-marine-120408-151453.

——, I. R. Simpson, A. S. Phillips, and K. A. McKinnon, 2018: How Well Do We Know ENSO's Climate Impacts over North America, and How Do We Evaluate Models Accordingly? *Journal of Climate*, **31**, 4991–5014, https://doi.org/10.1175/JCLI-D-17-0783.1.

Dettinger, M. D., D. R. Cayan, H. F. Diaz, and D. M. Meko, 1998: North–South Precipitation Patterns in Western North America on Interannual-to-Decadal Timescales. *Journal of Climate*, **11**, 3095–3111, https://doi.org/10.1175/1520-0442(1998)011<3095:NSPPIW>2.0.CO;2.

Diffenbaugh, N. S., D. L. Swain, and D. Touma, 2015: Anthropogenic warming has increased drought risk in California. *Proceedings of the National Academy of Sciences of the United States of America*, **112**, 3931–3936.

Dong, L., and L. R. Leung, 2021: Winter Precipitation Changes in California Under Global Warming: Contributions of CO2, Uniform SST Warming, and SST Change Patterns.

Geophysical Research Letters, **48**, e2020GL091736, https://doi.org/10.1029/2020GL091736.

Dong, Y., C. Proistosescu, K. C. Armour, and D. S. Battisti, 2019: Attributing Historical and Future Evolution of Radiative Feedbacks to Regional Warming Patterns using a Green's Function Approach: The Preeminence of the Western Pacific. *Journal of Climate*, **32**, 5471–5491, https://doi.org/10.1175/JCLI-D-18-0843.1.

——, K. C. Armour, M. D. Zelinka, C. Proistosescu, D. S. Battisti, C. Zhou, and T. Andrews, 2020: Intermodel Spread in the Pattern Effect and Its Contribution to Climate Sensitivity in CMIP5 and CMIP6 Models. *Journal of Climate*, **33**, 7755–7775, https://doi.org/10.1175/JCLI-D-19-1011.1.

——, A. G. Pauling, S. Sadai, and K. C. Armour, 2022: Antarctic Ice-Sheet Meltwater Reduces Transient Warming and Climate Sensitivity Through the Sea-Surface Temperature Pattern Effect. *Geophysical Research Letters*, **49**, e2022GL101249, https://doi.org/10.1029/2022GL101249.

Emanuel, K., 2020: The Relevance of Theory for Contemporary Research in Atmospheres, Oceans, and Climate. *AGU Advances*, **1**, e2019AV000129, https://doi.org/10.1029/2019AV000129.

England, M. H., and Coauthors, 2014: Recent intensification of wind-driven circulation in the Pacific and the ongoing warming hiatus. *Nature Clim Change*, **4**, 222–227, https://doi.org/10.1038/nclimate2106.

Evans, C. P., S. Coats, C. M. Carrillo, X. Li, M. J. Alessi, D. A. Herrera, B. N. Benton, and T. R. Ault, 2022: Intrinsic Century-Scale Variability in Tropical Pacific Sea Surface Temperatures and Their Influence on Western US Hydroclimate. *Geophysical Research Letters*, **49**, e2022GL099770, https://doi.org/10.1029/2022GL099770.

Eyring, V., S. Bony, G. A. Meehl, C. A. Senior, B. Stevens, R. J. Stouffer, and K. E. Taylor, 2016: Overview of the Coupled Model Intercomparison Project Phase 6 (CMIP6) experimental design and organization. *Geoscientific Model Development*, **9**, 1937–1958, https://doi.org/10.5194/gmd-9-1937-2016.

Flynn, C. M., and T. Mauritsen, 2020: On the climate sensitivity and historical warming evolution in recent coupled model ensembles. *Atmospheric Chemistry and Physics*, **20**, 7829–7842, https://doi.org/10.5194/acp-20-7829-2020.

Frey, W. R., E. A. Maroon, A. G. Pendergrass, and J. E. Kay, 2017: Do Southern Ocean Cloud Feedbacks Matter for 21st Century Warming? *Geophysical Research Letters*, **44**, 12,447-12,456, https://doi.org/10.1002/2017GL076339.

Fueglistaler, S., and L. g. Silvers, 2021: The Peculiar Trajectory of Global Warming. *Journal of Geophysical Research: Atmospheres*, **126**, e2020JD033629, https://doi.org/10.1029/2020JD033629.

Gordon, E. M., E. A. Barnes, and J. W. Hurrell, 2021: Oceanic Harbingers of Pacific Decadal Oscillation Predictability in CESM2 Detected by Neural Networks. *Geophysical Research Letters*, **48**, e2021GL095392, https://doi.org/10.1029/2021GL095392.

Goswami, B. N., J. Shukla, E. K. Schneider, and Y. C. Sud, 1984: Study of the Dynamics of the Intertropical Convergence Zone with a Symmetric Version of the GLAS Climate Model. *Journal of the Atmospheric Sciences*, **41**, 5–19, https://doi.org/10.1175/1520-0469(1984)041<0005:SOTDOT>2.0.CO;2.

Gregory, J. M., and P. M. Forster, 2008: Transient climate response estimated from radiative forcing and observed temperature change. *Journal of Geophysical Research: Atmospheres*, **113**, https://doi.org/10.1029/2008JD010405.

——, R. J. Stouffer, S. C. B. Raper, P. A. Stott, and N. A. Rayner, 2002: An Observationally Based Estimate of the Climate Sensitivity. *Journal of Climate*, **15**, 3117–3121, https://doi.org/10.1175/1520-0442(2002)015<3117:AOBEOT>2.0.CO;2.

——, and Coauthors, 2004: A new method for diagnosing radiative forcing and climate sensitivity. *Geophysical Research Letters*, **31**, https://doi.org/10.1029/2003GL018747.

——, T. Andrews, and P. Good, 2015: The inconstancy of the transient climate response parameter under increasing CO2. *Philosophical Transactions of the Royal Society A: Mathematical, Physical and Engineering Sciences*, **373**, 20140417, https://doi.org/10.1098/rsta.2014.0417.

——, ——, P. Ceppi, T. Mauritsen, and M. J. Webb, 2020: How accurately can the climate sensitivity to $$\hbox {CO}_{2}$$ be estimated from historical climate change? *Clim Dyn*, **54**, 129–157, https://doi.org/10.1007/s00382-019-04991-y.

Grise, K. M., and S. M. Davis, 2020: Hadley cell expansion in CMIP6 models. *Atmospheric Chemistry and Physics*, **20**, 5249–5268, https://doi.org/10.5194/acp-20-5249-2020.

Hawkins, E., and R. Sutton, 2009: The Potential to Narrow Uncertainty in Regional Climate Predictions. *Bulletin of the American Meteorological Society*, **90**, 1095–1108, https://doi.org/10.1175/2009BAMS2607.1.

He, J., and B. J. Soden, 2017: A re-examination of the projected subtropical precipitation decline. *Nature Clim Change*, **7**, 53–57, https://doi.org/10.1038/nclimate3157.

Heede, U. K., and A. V. Fedorov, 2021: Eastern equatorial Pacific warming delayed by aerosols and thermostat response to CO2 increase. *Nat. Clim. Chang.*, **11**, 696–703, https://doi.org/10.1038/s41558-021-01101-x.

——, ——, and N. J. Burls, 2020: Time Scales and Mechanisms for the Tropical Pacific Response to Global Warming: A Tug of War between the Ocean Thermostat and Weaker Walker. *Journal of Climate*, **33**, 6101–6118, https://doi.org/10.1175/JCLI-D-19-0690.1.

Hoerling, M., J. Eischeid, and J. Perlwitz, 2010: Regional Precipitation Trends: Distinguishing Natural Variability from Anthropogenic Forcing. *Journal of Climate*, **23**, 2131–2145, https://doi.org/10.1175/2009JCLI3420.1.

Hoerling, M. P., and A. Kumar, 2002: Atmospheric Response Patterns Associated with Tropical Forcing. *Journal of Climate*, **15**, 2184–2203, https://doi.org/10.1175/1520-0442(2002)015<2184:ARPAWT>2.0.CO;2.

——, ——, and M. Zhong, 1997: El Niño, La Niña, and the Nonlinearity of Their Teleconnections. *Journal of Climate*, **10**, 1769–1786, https://doi.org/10.1175/1520-0442(1997)010<1769:ENOLNA>2.0.CO;2.

Horel, J. D., and J. M. Wallace, 1981: Planetary-Scale Atmospheric Phenomena Associated with the Southern Oscillation. *Monthly Weather Review*, **109**, 813–829, https://doi.org/10.1175/1520-0493(1981)109<0813:PSAPAW>2.0.CO;2.

Hu, F., L. Zhang, Q. Liu, and D. Chyi, 2021: Environmental Factors Controlling the Precipitation in California. *Atmosphere*, **12**, 997, https://doi.org/10.3390/atmos12080997.

Hu, S., S.-P. Xie, and S. M. Kang, 2022: Global Warming Pattern Formation: The Role of Ocean Heat Uptake. *Journal of Climate*, **35**, 1885–1899, https://doi.org/10.1175/JCLI-D-21-0317.1.

Huang, P., and J. Ying, 2015: A Multimodel Ensemble Pattern Regression Method to Correct the Tropical Pacific SST Change Patterns under Global Warming. *Journal of Climate*, **28**, 4706–4723, https://doi.org/10.1175/JCLI-D-14-00833.1.

Huber, M., and R. Knutti, 2014: Natural variability, radiative forcing and climate response in the recent hiatus reconciled. *Nature Geosci*, **7**, 651–656, https://doi.org/10.1038/ngeo2228.

Intergovernmental Panel on Climate Change (IPCC), ed., 2023: Technical Summary. *Climate Change 2021 – The Physical Science Basis: Working Group I Contribution to the Sixth Assessment Report of the Intergovernmental Panel on Climate Change*, Cambridge University Press, 35–144.

Kajtar, J. B., A. Santoso, M. Collins, A. S. Taschetto, M. H. England, and L. M. Frankcombe, 2021: CMIP5 Intermodel Relationships in the Baseline Southern Ocean Climate System and With Future Projections. *Earth's Future*, **9**, e2020EF001873, https://doi.org/10.1029/2020EF001873.

Kang, S. M., Y. Yu, C. Deser, X. Zhang, I.-S. Kang, S.-S. Lee, K. B. Rodgers, and P. Ceppi, 2023: Global impacts of recent Southern Ocean cooling. *Proceedings of the National Academy of Sciences*, **120**, e2300881120, https://doi.org/10.1073/pnas.2300881120.

Kim, H., S. M. Kang, J. E. Kay, and S.-P. Xie, 2022: Subtropical clouds key to Southern Ocean teleconnections to the tropical Pacific. *Proceedings of the National Academy of Sciences*, **119**, e2200514119, https://doi.org/10.1073/pnas.2200514119.

Klocke, D., J. Quaas, and B. Stevens, 2013: Assessment of different metrics for physical climate feedbacks. *Clim Dyn*, **41**, 1173–1185, https://doi.org/10.1007/s00382-013-1757-1.

Kociuba, G., and S. B. Power, 2015: Inability of CMIP5 Models to Simulate Recent Strengthening of the Walker Circulation: Implications for Projections. *Journal of Climate*, **28**, 20–35, https://doi.org/10.1175/JCLI-D-13-00752.1.

Kohyama, T., D. L. Hartmann, and D. S. Battisti, 2017: La Niña–like Mean-State Response to Global Warming and Potential Oceanic Roles. *Journal of Climate*, **30**, 4207–4225, https://doi.org/10.1175/JCLI-D-16-0441.1.

Kuhlbrodt, T., and J. M. Gregory, 2012: Ocean heat uptake and its consequences for the magnitude of sea level rise and climate change. *Geophysical Research Letters*, **39**, https://doi.org/10.1029/2012GL052952.

Kuo, Y.-N., H. Kim, and F. Lehner, 2023: Anthropogenic Aerosols Contribute to the Recent Decline in Precipitation Over the U.S. Southwest. *Geophysical Research Letters*, **50**, e2023GL105389, https://doi.org/10.1029/2023GL105389.

Lau, W. K. M., and K.-M. Kim, 2015: Robust Hadley Circulation changes and increasing global dryness due to CO2 warming from CMIP5 model projections. *Proceedings of the National Academy of Sciences*, **112**, 3630–3635, https://doi.org/10.1073/pnas.1418682112.

Lehner, F., C. Deser, I. R. Simpson, and L. Terray, 2018: Attributing the U.S. Southwest's Recent Shift Into Drier Conditions. *Geophysical Research Letters*, **45**, 6251–6261, https://doi.org/10.1029/2018GL078312.

——, ——, N. Maher, J. Marotzke, E. M. Fischer, L. Brunner, R. Knutti, and E. Hawkins, 2020: Partitioning climate projection uncertainty with multiple large ensembles and CMIP5/6. *Earth System Dynamics*, **11**, 491–508, https://doi.org/10.5194/esd-11-491-2020.

L'Heureux, M. L., M. K. Tippett, and W. Wang, 2022: Prediction Challenges From Errors in Tropical Pacific Sea Surface Temperature Trends. *Front. Clim.*, **4**, https://doi.org/10.3389/fclim.2022.837483.

Lin, Y.-J., Y.-T. Hwang, J. Lu, F. Liu, and B. E. J. Rose, 2021: The Dominant Contribution of Southern Ocean Heat Uptake to Time-Evolving Radiative Feedback in CESM. *Geophysical Research Letters*, **48**, e2021GL093302, https://doi.org/10.1029/2021GL093302.

Loeb, N. G., G. C. Johnson, T. J. Thorsen, J. M. Lyman, F. G. Rose, and S. Kato, 2021: Satellite and Ocean Data Reveal Marked Increase in Earth's Heating Rate. *Geophysical Research Letters*, **48**, e2021GL093047, https://doi.org/10.1029/2021GL093047.

Ma, S., and T. Zhou, 2016: Robust Strengthening and Westward Shift of the Tropical Pacific Walker Circulation during 1979–2012: A Comparison of 7 Sets of Reanalysis Data and

26 CMIP5 Models. *Journal of Climate*, **29**, 3097–3118, https://doi.org/10.1175/JCLI-D-15-0398.1.

Madadgar, S., A. AghaKouchak, S. Shukla, A. W. Wood, L. Cheng, K.-L. Hsu, and M. Svoboda, 2016: A hybrid statistical-dynamical framework for meteorological drought prediction: Application to the southwestern United States. *Water Resources Research*, **52**, 5095–5110, https://doi.org/10.1002/2015WR018547.

Maher, N., and Coauthors, 2019: The Max Planck Institute Grand Ensemble: Enabling the Exploration of Climate System Variability. *Journal of Advances in Modeling Earth Systems*, **11**, 2050–2069, https://doi.org/10.1029/2019MS001639.

——, J. E. Kay, and A. Capotondi, 2022: Modulation of ENSO teleconnections over North America by the Pacific decadal oscillation. *Environ. Res. Lett.*, **17**, 114005, https://doi.org/10.1088/1748-9326/ac9327.

Mamalakis, A., A. Langousis, R. Deidda, and M. Marrocu, 2017: A parametric approach for simultaneous bias correction and high-resolution downscaling of climate model rainfall. *Water Resources Research*, **53**, 2149–2170, https://doi.org/10.1002/2016WR019578.

——, J.-Y. Yu, J. T. Randerson, A. AghaKouchak, and E. Foufoula-Georgiou, 2018: A new interhemispheric teleconnection increases predictability of winter precipitation in southwestern US. *Nat Commun*, **9**, 2332, https://doi.org/10.1038/s41467-018-04722-7.

Manabe, S., and R. T. Wetherald, 1975: The Effects of Doubling the CO2 Concentration on the climate of a General Circulation Model. *Journal of the Atmospheric Sciences*, **32**, 3–15, https://doi.org/10.1175/1520-0469(1975)032<0003:TEODTC>2.0.CO;2.

Mankin, J. S., I. R. Simpson, A. Hoell, and R. Fu, 2021: NOAA Drought Task Force Report on the 2020–2021 Southwestern U.S. Drought | Drought.gov. https://www.drought.gov/documents/noaa-drought-task-force-report-2020-2021-southwestern-us-drought (Accessed April 24, 2024).

Mayer, K. J., and E. A. Barnes, 2021: Subseasonal Forecasts of Opportunity Identified by an Explainable Neural Network. *Geophysical Research Letters*, **48**, e2020GL092092, https://doi.org/10.1029/2020GL092092.

McCabe, G. J., M. A. Palecki, and J. L. Betancourt, 2004: Pacific and Atlantic Ocean influences on multidecadal drought frequency in the United States. *Proceedings of the National Academy of Sciences*, **101**, 4136–4141, https://doi.org/10.1073/pnas.0306738101.

Murphy, J. M., 1995: Transient Response of the Hadley Centre Coupled Ocean-Atmosphere Model to Increasing Carbon Dioxide. Part 1: Control Climate and Flux Adjustment. *Journal of Climate*, **8**, 36–56, https://doi.org/10.1175/1520-0442(1995)008<0036:TROTHC>2.0.CO;2.

Newsom, E., L. Zanna, S. Khatiwala, and J. M. Gregory, 2020: The Influence of Warming Patterns on Passive Ocean Heat Uptake. *Geophysical Research Letters*, **47**, e2020GL088429, https://doi.org/10.1029/2020GL088429.

Olonscheck, D., M. Rugenstein, and J. Marotzke, 2020: Broad Consistency Between Observed and Simulated Trends in Sea Surface Temperature Patterns. *Geophysical Research Letters*, **47**, e2019GL086773, https://doi.org/10.1029/2019GL086773.

Ordoñez, P., R. Nieto, L. Gimeno, P. Ribera, D. Gallego, C. A. Ochoa-Moya, and A. I. Quintanar, 2019: Climatological moisture sources for the Western North American Monsoon through a Lagrangian approach: their influence on precipitation intensity. *Earth System Dynamics*, **10**, 59–72, https://doi.org/10.5194/esd-10-59-2019.

Park, C., S. M. Kang, M. F. Stuecker, and F.-F. Jin, 2022: Distinct Surface Warming Response Over the Western and Eastern Equatorial Pacific to Radiative Forcing. *Geophysical Research Letters*, **49**, e2021GL095829, https://doi.org/10.1029/2021GL095829.

Pincus, R., P. M. Forster, and B. Stevens, 2016: The Radiative Forcing Model Intercomparison Project (RFMIP): experimental protocol for CMIP6. *Geoscientific Model Development*, **9**, 3447–3460, https://doi.org/10.5194/gmd-9-3447-2016.

Plesca, E., V. Grützun, and S. A. Buehler, 2018: How Robust Is the Weakening of the Pacific Walker Circulation in CMIP5 Idealized Transient Climate Simulations? *Journal of Climate*, **31**, 81–97, https://doi.org/10.1175/JCLI-D-17-0151.1.

Rasp, S., M. S. Pritchard, and P. Gentine, 2018: Deep learning to represent subgrid processes in climate models. *Proceedings of the National Academy of Sciences of the United States of America*, **115**, 9684–9689.

Rayner, N. A., D. E. Parker, E. B. Horton, C. K. Folland, L. V. Alexander, D. P. Rowell, E. C. Kent, and A. Kaplan, 2003: Global analyses of sea surface temperature, sea ice, and night marine air temperature since the late nineteenth century. *Journal of Geophysical Research: Atmospheres*, **108**, https://doi.org/10.1029/2002JD002670.

Redmond, K. T., and R. W. Koch, 1991: Surface Climate and Streamflow Variability in the Western United States and Their Relationship to Large-Scale Circulation Indices. *Water Resources Research*, **27**, 2381–2399, https://doi.org/10.1029/91WR00690.

Rojas, M., F. Lambert, J. Ramirez-Villegas, and A. J. Challinor, 2019: Emergence of robust precipitation changes across crop production areas in the 21st century. *Proceedings of the National Academy of Sciences*, **116**, 6673–6678, https://doi.org/10.1073/pnas.1811463116.

Ropelewski, C. F., and M. S. Halpert, 1986: North American Precipitation and Temperature Patterns Associated with the El Niño/Southern Oscillation (ENSO). *Monthly Weather Review*, **114**, 2352–2362, https://doi.org/10.1175/1520-0493(1986)114<2352:NAPATP>2.0.CO;2.

Rugenstein, M., S. Dhame, D. Olonscheck, R. J. Wills, M. Watanabe, and R. Seager, 2023: Connecting the SST Pattern Problem and the Hot Model Problem. *Geophysical Research Letters*, **50**, e2023GL105488, https://doi.org/10.1029/2023GL105488.

Rugenstein, M. A. A., K. Caldeira, and R. Knutti, 2016: Dependence of global radiative feedbacks on evolving patterns of surface heat fluxes. *Geophysical Research Letters*, **43**, 9877–9885, https://doi.org/10.1002/2016GL070907.

Salvi, K., G. Villarini, and G. A. Vecchi, 2017: High resolution decadal precipitation predictions over the continental United States for impacts assessment. *Journal of Hydrology*, **553**, 559–573, https://doi.org/10.1016/j.jhydrol.2017.07.043.

Sardeshmukh, P. D., and B. J. Hoskins, 1988: The Generation of Global Rotational Flow by Steady Idealized Tropical Divergence. *Journal of the Atmospheric Sciences*, **45**, 1228–1251, https://doi.org/10.1175/1520-0469(1988)045<1228:TGOGRF>2.0.CO;2.

Schneider, T., J. Teixeira, C. S. Bretherton, F. Brient, K. G. Pressel, C. Schär, and A. P. Siebesma, 2017: Climate goals and computing the future of clouds. *Nature Clim Change*, **7**, 3–5, https://doi.org/10.1038/nclimate3190.

Schubert, S. D., and Coauthors, 2016: Global Meteorological Drought: A Synthesis of Current Understanding with a Focus on SST Drivers of Precipitation Deficits. *Journal of Climate*, **29**, 3989–4019, https://doi.org/10.1175/JCLI-D-15-0452.1.

Seager, R., and M. Hoerling, 2014: Atmosphere and Ocean Origins of North American Droughts. *Journal of Climate*, **27**, 4581–4606, https://doi.org/10.1175/JCLI-D-13-00329.1.

——, N. Naik, and G. A. Vecchi, 2010: Thermodynamic and Dynamic Mechanisms for Large-Scale Changes in the Hydrological Cycle in Response to Global Warming. *Journal of Climate*, **23**, 4651–4668, https://doi.org/10.1175/2010JCLI3655.1.

——, M. Hoerling, S. Schubert, H. Wang, B. Lyon, A. Kumar, J. Nakamura, and N. Henderson, 2015: Causes of the 2011–14 California Drought. *Journal of Climate*, **28**, 6997–7024, https://doi.org/10.1175/JCLI-D-14-00860.1.

——, M. Cane, N. Henderson, D.-E. Lee, R. Abernathey, and H. Zhang, 2019: Strengthening tropical Pacific zonal sea surface temperature gradient consistent with rising greenhouse gases. *Nat. Clim. Chang.*, **9**, 517–522, https://doi.org/10.1038/s41558-019-0505-x.

——, N. Henderson, and M. Cane, 2022: Persistent Discrepancies between Observed and Modeled Trends in the Tropical Pacific Ocean. *Journal of Climate*, **35**, 4571–4584, https://doi.org/10.1175/JCLI-D-21-0648.1.

Senior, C. A., and J. F. B. Mitchell, 2000: The time-dependence of climate sensitivity. *Geophysical Research Letters*, **27**, 2685–2688, https://doi.org/10.1029/2000GL011373.

Sheffield, J., E. F. Wood, and M. L. Roderick, 2012: Little change in global drought over the past 60 years. *Nature*, **491**, 435–438, https://doi.org/10.1038/nature11575.

Shepherd, T. G., and Coauthors, 2018: Storylines: an alternative approach to representing uncertainty in physical aspects of climate change. *Climatic Change*, **151**, 555–571, https://doi.org/10.1007/s10584-018-2317-9.

Stevens, B., and Coauthors, 2013: Atmospheric component of the MPI-M Earth System Model: ECHAM6. *Journal of Advances in Modeling Earth Systems*, **5**, 146–172, https://doi.org/10.1002/jame.20015.

——, S. C. Sherwood, S. Bony, and M. J. Webb, 2016: Prospects for narrowing bounds on Earth's equilibrium climate sensitivity. *Earth's Future*, **4**, 512–522, https://doi.org/10.1002/2016EF000376.

van Vuuren, D. P., and Coauthors, 2011: The representative concentration pathways: an overview. *Climatic Change*, **109**, 5, https://doi.org/10.1007/s10584-011-0148-z.

Wang, C., L. Zhang, S.-K. Lee, L. Wu, and C. R. Mechoso, 2014: A global perspective on CMIP5 climate model biases. *Nature Clim Change*, **4**, 201–205, https://doi.org/10.1038/nclimate2118.

Wang, G., W. Cai, and A. Santoso, 2017: Assessing the Impact of Model Biases on the Projected Increase in Frequency of Extreme Positive Indian Ocean Dipole Events. *Journal of Climate*, **30**, 2757–2767, https://doi.org/10.1175/JCLI-D-16-0509.1.

Watanabe, M., J.-L. Dufresne, Y. Kosaka, T. Mauritsen, and H. Tatebe, 2021: Enhanced warming constrained by past trends in equatorial Pacific sea surface temperature gradient. *Nat. Clim. Chang.*, **11**, 33–37, https://doi.org/10.1038/s41558-020-00933-3.

Williams, A. I. L., N. Jeevanjee, and J. Bloch-Johnson, 2023: Circus Tents, Convective Thresholds, and the Non-Linear Climate Response to Tropical SSTs. *Geophysical Research Letters*, **50**, e2022GL101499, https://doi.org/10.1029/2022GL101499.

Williams, A. P., B. I. Cook, and J. E. Smerdon, 2022: Rapid intensification of the emerging southwestern North American megadrought in 2020–2021. *Nat. Clim. Chang.*, **12**, 232–234, https://doi.org/10.1038/s41558-022-01290-z.

Wills, R. C. J., Y. Dong, C. Proistosecu, K. C. Armour, and D. S. Battisti, 2022: Systematic Climate Model Biases in the Large-Scale Patterns of Recent Sea-Surface Temperature and Sea-Level Pressure Change. *Geophysical Research Letters*, **49**, e2022GL100011, https://doi.org/10.1029/2022GL100011.

Wood, R., and C. S. Bretherton, 2006: On the Relationship between Stratiform Low Cloud Cover and Lower-Tropospheric Stability. *Journal of Climate*, **19**, 6425–6432, https://doi.org/10.1175/JCLI3988.1.

Zanna, L., and T. Bolton, 2020: Data-Driven Equation Discovery of Ocean Mesoscale Closures. *Geophysical Research Letters*, **47**, e2020GL088376, https://doi.org/10.1029/2020GL088376.

Zelinka, M. D., T. A. Myers, D. T. McCoy, S. Po-Chedley, P. M. Caldwell, P. Ceppi, S. A. Klein, and K. E. Taylor, 2020: Causes of Higher Climate Sensitivity in CMIP6 Models. *Geophysical Research Letters*, **47**, e2019GL085782, https://doi.org/10.1029/2019GL085782.

Zhang, B., M. Zhao, and Z. Tan, 2023: Using a Green's Function Approach to Diagnose the Pattern Effect in GFDL AM4 and CM4. *Journal of Climate*, **36**, 1105–1124, https://doi.org/10.1175/JCLI-D-22-0024.1.

Zhou, C., M. D. Zelinka, and S. A. Klein, 2016: Impact of decadal cloud variations on the Earth's energy budget. *Nature Geosci*, **9**, 871–874, https://doi.org/10.1038/ngeo2828.

——, ——, and ——, 2017: Analyzing the dependence of global cloud feedback on the spatial pattern of sea surface temperature change with a Green's function approach. *Journal of Advances in Modeling Earth Systems*, **9**, 2174–2189, https://doi.org/10.1002/2017MS001096.

——, ——, A. E. Dessler, and M. Wang, 2021: Greater committed warming after accounting for the pattern effect. *Nat. Clim. Chang.*, **11**, 132–136, https://doi.org/10.1038/s41558-020-00955-x.

APPENDIX A: SUPPORTING INFORMATION FOR CHAPTER 2

A.1 Text

A.1.1 Definitions

Mean-state bias: Disagreement between model output and observations in the mean (climatological) state, usually defined over a period in the recent past of 30 years or more (Zhang et al., 2023).

***Forcing response bias*:** Inability of AOGCMs to replicate the observed SST trend patterns in response to a climate forcing (e.g., CO_2, volcanic). Can sometimes be caused by the existence of a mean-state bias (Seager et al., 2019; Kajtar et al., 2021).

SST pattern scenario: A scenario where the SST pattern is inspired by historical *SST pattern uncertainty* and theory. We convolve this SST pattern with the radiation and temperature GFs to obtain λ (Eq. 2) and then solve for ΔT (Eq. 1).

Uncertainty due to internal variability: Natural fluctuations that arise in the absence of any radiative forcing of the planet (Hawkins and Sutton, 2009).

Structural uncertainty: Different models simulate different changes in climate in response to the same radiative forcing (Hawkins and Sutton, 2009). This is due to differences in, e.g., model parameterizations, model coupling, and model resolution.

Forcing scenario uncertainty: Uncertainty in the future radiative forcing (Hawkins and Sutton, 2009). E.g., the high emissions scenario (RCP8.5) increases CO_2 emissions through the end of the 21st century. This uncertainty is expressed in the range of scenarios (RCP8.5 or RCP4.5). We use the higher emission scenarios (RCP4.5 and RCP8.5) for illustrative reasons here.

***SST pattern uncertainty*:** A future model uncertainty arising from erroneous model physics (most likely in their ocean-atmosphere interaction or upper ocean physics), erroneous internal

variability, and/or erroneous forcing input to AOGCM simulations. It accounts for the fact that SST trend patterns simulated in the future by AOGCMs may not capture future observations, just as the historical SST trend pattern in AOGCMs did not capture the observed warming (potential *forcing response bias* and underestimation of true internal variability of the climate system). This uncertainty could be described as a sum of the three classical uncertainties if AOGCMs were able to replicate the observed SST pattern.

A.1.2 Green's function

We develop a Green's function (GF) following the approaches in Zhou et al. (2017) and Dong et al. (2019). A GF is derived from multiple simulations of one atmospheric GCM where anomalous SST patch perturbations are prescribed locally while elsewhere the SST is kept constant. We use the Max Planck Institute's atmospheric model ECHAM v6.3 with a latitude x longitude grid of 96 x 192 (Stevens et al., 2013). First, a base state simulation is run for 26 years with a prescribed SST from the HadISST observed dataset (Rayner et al., 2003) averaged from 1990-2009, and all radiative forcings (e.g., GHG, aerosols) are held constant at year 2000 levels (Dong et al., 2019). Anomalous SST patch simulations are then initialized from year 6 of the control simulation and run for 20 years each. A positive and negative SST perturbation is run for each patch (Zhou et al., 2017). Following Barsugli and Sardeshmukh (2002), the SST anomalies follow a cosine hump to avoid nonlinearity caused by an unrealistic SST gradient:

$$\delta SST(x,y) = A\cos^2\left(\frac{\pi}{2}\frac{y-y_p}{y_w}\right)\cos^2\left(\frac{\pi}{2}\frac{x-x_p}{x_w}\right),$$

where A is the amplitude of the SST patch anomaly (+/- 4 K) (Zhou et al., 2017), subscript p denotes the center point of the patch, and subscript w denotes the half-width of the patch. The setup we use here is novel in that the patches are equal in forcing area, rather than set by lat/lon boxes (Zhou et al., 2017; Dong et al, 2019), which avoids some nonlinearities that propagate

through the calculations due to different patch sizes. y_w is 2150 km and x_w is 4300 km, so that the patches are 8600 km x 4300 km in size. In total 91 patch simulations were run for each temperature perturbation to cover most of the globe, and sea ice was kept constant using the 1990-2009 average (Figure A.2.6). The forcing and radiative response for one of the SST patches east of the Philippines is plotted in Figure A.2.6.

Once the two GF are created (GF_R and GF_T; see text), they are slightly adjusted to better represent the net TOA radiative response and temperature response to a given SST pattern compared to coupled model output. For GF_R, very small negative values (-5.0×10^{-4} to 0.0) are set to zero, since we found GF_R to have too small of a signal to noise ratio. These negative values resulted in the calculated net TOA radiative response to any SST pattern to be too negative; so that the response to an SST pattern calculated from the GF (dashed lines in Figure A.2.2) are too negative compared to the MPI-ESM coupled model output (solid lines in Figure A.2.2). Setting all small positive and negative values equal to zero that were not statistically different from zero, as in Dong et al. (2019), resulted in a GF_R that was too positive by 1.5 Wm^{-2} by year 100 in an abrupt $4xCO_2$ simulation. We found GF_T to not be positive enough and slightly increased all values in GF_T by 3.5×10^{-5} K/K. We validate the use of the GF for our purpose by convolving SST output from fully coupled MPI Earth System Model (MPI-ESM) simulations with both GFs (Figure A.2.2). The GF reproduces ΔT and $N - F$ well over the historical period (1850-2006) but slightly underpredicts simulations which quadruple CO_2 in a step-forcing (Figure A.2.2). We applied GF_R to each ensemble member of the MPI-GE RCP8.5 and found that the GF predicts the coupled modeled values well, with a 0.97 correlation between the GF_R response and the coupled model output from 2006-2100. We also highlight that in comparing our GF to the coupled model output (Figure A.2.2), we chose a more difficult target than the AGCM

simulations with prescribed SST which are used to validate the GF in Dong et al. (2019). This makes our GF more robust and more widely applicable than others used thus far.

A.1.3 Construction of temperature projections

We derive temperature projections from the energy balance model in equation (1). We use Eq. (2) to calculate ΔT, rather than simply convolving the SST pattern with GF_T, to keep the climate system in energy balance given an adjusted SST pattern. To solve for λ, an annual-mean SST pattern is first convolved with GF_R and GF_T to get global mean R and T values respectively. The SST pattern is an anomaly from the preindustrial control (1850-1870). A 30-year sliding linear regression is then applied to these R and T values to get λ (e.g., Andrews et al. 2018), such that a λ value for a given year represents the center of the 30-year sliding window. For example, in Figure 2.2b, the MPI-ESM grand ensemble ensemble-mean historical λ of -1.47 $Wm^{-2}K^{-1}$ in 2000 represents the slope of R against T for the years 1985-2015. To complete equation (2), N_{RCP} and F are also anomalies with respect to pre-industrial control (average of 1850-1870). We calculate F by running an ECHAM simulation with constant preindustrial (average of 1850-1870) SST and sea ice concentration with time-dependent atmospheric and land forcings from historical and RCP8.5 simulations (Pincus et al. 2016). N_{RCP} is taken from the MPI-ESM grand ensemble output for all ensemble members for RCP historical, RCP4.5, and RCP8.5. Anomalies in all temperature projection figures (Figures 2.2a) are with respect to the 2000-2010 RCP ensemble-mean ΔT.

To solve for ΔT, the GF is convolved with the SST pattern of each ensemble member from historical, RCP8.5, RCP4.5, and the idealized scenarios in Section 4 (Eq. 2). Therefore, the *ensemble-mean* throughout the paper is the mean of all the 100 ensemble members after their individual SST patterns are convolved with the GFs.

The MPI-GE ensemble-mean historical and RCP8.5 temperature projections (dark gray in Figures 2.2a) follow the same method as the scenarios (Eq. 1). The coupled model output SST is used to solve for λ, and then the same N_{RCP} and F are used to calculate ΔT.

A.1.4 Idealized Scenarios

We generate a warm and cool scenario for the equatorial West Pacific, tropical East Pacific, and Southern Ocean. We selected these three regions due to their prominent *forcing response biases* over the historical record (Table A.3.1). All six scenarios have equal area forcings, so that the scenarios are comparable to each other. The bounding boxes for the regions are: 110°E-156°E and 18°S-20°N for the equatorial West Pacific, 120°W-71°W and 28°S to 1°N for the tropical East Pacific, and 0°-360° and 58°S-53°S for the Southern Ocean. Note that ΔT is insensitive to the SO patch location (Figure 2.1), and the EP patch was selected based on the MSCD location. We apply an SST anomaly adjustment to each ensemble member's SST pattern in these regions based on 3% of the global-mean SST anomaly for any given year from pre-industrial control (1850-1870). Thus, a "cool" scenario is somewhat colder than the RCP reference but still warming with respect to present day values. We selected a perturbation of 3% based on realistic SST fluctuations due to historical *SST pattern uncertainty* in these regions. The order of magnitude of the adjusted SST, 1.1 K in the region by 2085, is comparable to model error in the tropical East Pacific (Figure 1 in Seager et al. 2019) and Southern Ocean (Figure 2 in Wills et al. 2022) and slightly greater than the difference between AOGCMs and observations in the equatorial West Pacific (Figure 2 in Wills et al. 2022; Figure 5 in Fueglistaler and Silvers, 2021). To keep the global-mean SST constant (ΔSST), we redistribute the warming or cooling to the rest of the planet (on the order of 0.01K by 2085), again for each ensemble member. This adjustment has almost no impact on changing the final ΔT result (on the order of 0.01K), which we tested by

running the same simulations with only a change in SST in the region of interest (with no redistribution of SST).

While a 3% redistribution is selected based on historical *SST pattern uncertainty*, we also tested the sensitivity of future global-mean temperature projection uncertainty to other redistribution values. For a 10% redistribution SST value applied to both WP scenarios, the range of uncertainty increases from 1.1 K to 4.0 K (instead of 2.0 K with a 3% SST adjustment). However, an increase and decrease in SST in the WP based on 10% of ΔSST (~4.0 K) is unrealistic, and it has no historical precedence. For a 5% redistribution scenario, SST is adjusted by 1.9 K in the region of interest and results in a range of uncertainty increase from 1.1 K to 2.5 K.

A.1.5 Uncertainty of the Top of Atmosphere Radiative Imbalance (N)

We use N_{RCP} as the top of atmosphere radiative imbalance for all scenarios with different SST patterns. While there is evidence that N and λ are correlated based on a change in the SST pattern (because both depend on the SST pattern; Newsom et al. 2020; Andrews et al. 2022), we found that the two are uncorrelated across ensemble members for different years in the MPI-GE (Figure A.2.3a), and the correlation does not exist across time (Figure A.2.3b). In other words, a less negative (destabilizing) λ does not necessarily require a high ocean heat uptake on decadal timescales or over the range of λ we are testing here. Despite this finding, we tested the sensitivity of ΔT to a +/- 10% change in N_{RCP} compared to the default values for each scenario used in the main text. While the effect of *SST pattern uncertainty* increases the range of uncertainty by 0.9 K in 2085 for WP_{cool} and WP_{warm}, a +/- 10% adjustment of N_{RCP} only affects the RCP8.5 ensemble spread of ΔT by 0.3 K (Figure A.2.7). N_{RCP} would have to be adjusted by nearly 30% to offset the potential impacts of *SST pattern uncertainty* which is unlikely given our

findings that N and λ are uncorrelated. Even if N were to fluctuate based on changes in the SST pattern (which we do not find), *SST pattern uncertainty* still elicits a stronger change in ΔT. We also found no correlation between λ and the ocean heat uptake efficiency (κ) for all 100 ensemble members of the MPI-GE (Figure A.2.3c). Despite the strongly different SST patterns across the ensemble, κ and λ are uncorrelated. Gregory and Forster (2008)also found no correlation between the two across CMIP3 models, and Kuhlbrodt and Gregory (2012) came to the same conclusion for CMIP5 models when two models were removed from the analysis. We further note that the ocean heat uptake experiments in Newsom et al. (2020) within one model found κ and λ to be correlated but did not consider the stronger observed trade winds which have accelerated the subtropical cells, enhancing ocean heat uptake efficiency (England et al. 2014; Andrews et al. 2022). The lack of correlation between κ and λ holds across time for all ensemble members in MPI-GE, i.e., there is no correlation between the *change in time* in λ and *the change in time* in κ within one ensemble member despite evolving SST patterns (Figure A.2.3d). We acknowledge that at some point there must be a correlation between $\Delta\lambda$ and $\Delta\kappa$ if the world warms significantly and increased ocean stratification decreases ocean heat uptake efficiency. However, with changes of λ between -1.55 $Wm^{-2}K^{-1}$ and -1.05 $Wm^{-2}K^{-1}$, a potential anticorrelation (which we do not find) is of second order importance for ΔT. Furthermore, λ will be more important for Eq. 1 because it is in the denominator. This justifies our use of N_{RCP} across the different temperature projection scenarios.

A.1.6 Change in Nonlocal SW Cloud Feedback Dominates

We decompose λ into individual radiative feedbacks by applying the partial radiation perturbation (PRP) technique (Klocke et al. 2013) to each patch simulation used to create the GFs. Thus, we have a GF for lapse rate, water vapor, longwave cloud (LW cloud), shortwave

cloud (SW cloud), albedo, and the Planck feedback. We tune these GFs in the same manner as GF_R so that they add up to GF_R, since there is no method for verification of each feedback individually. In other words, the very small negative values in each radiative GF (-5.0×10^{-4} to 0.0) are set to zero.

We convolve the GFs with each ensemble member's RCP8.5 SST pattern for years 2050-2100, which represents the reference state (Figure A.2.4a). The pattern effect acts mostly through SW clouds (Figure A.2.4b; Zhou et al. 2016, 2017; Dong et al. 2019), but also impacts the lapse rate feedback (Andrews and Webb 2018). For an idealized warming in the equatorial West Pacific from Section 4, a decrease in SW cloud feedback is consistent with nonlocal impacts on the MSCD (Wood and Bretherton 2006; Zhou et al. 2016; Ceppi and Gregory 2017; Andrews et al. 2018; Andrews and Webb 2018; Dong et al. 2019). For a change in SST in the East Pacific, the effects remain local (Zhou et al. 2016, 2017). We find this less negative λ to be accompanied by a slight increase in the lapse rate feedback, which develops from increased warming at the surface and little change in the mid atmosphere (Andrews and Webb 2018). In the Southern Ocean, the lapse rate and water vapor feedbacks influence the feedback parameter more than the SW cloud feedback. This seemingly disagrees with research suggesting the Southern Ocean drives changes in the SW cloud feedback through nonlocal warming in the tropical East Pacific (Lin et al. 2021), which we cannot capture with our GF based on SST patterns. In other words, our influence of SSTs in a certain region is due to local and remote TOA effects only, *not* due to remote SST changes.

For the 50-year transitional scenario (section 5), changes in λ from observations are dominated by a more positive lapse rate, SW cloud, and Planck λ and more negative water vapor and LW cloud λ (Figure A.2.4). This is due to weak warming in the equatorial West Pacific in

the middle years (2036-2056) of the transitional scenario and strong warming in the tropical East Pacific and Southern Ocean regions.

A.1.7 Change in Nonlocal SW Cloud Feedback Dominates

We develop more realistic and plausible temperature projection scenarios starting from the HadISST observed averaged pattern in 2016-2021. Two of these scenarios (see Supplemental Table 1) involve interpolating the SST at each grid point from the HadISST 2016-2021 average to the RCP8.5 ensemble-mean in 2031-2036 average ($\text{Transition}_{10\text{yr}}$) or 2071-2076 average ($\text{Transition}_{50\text{yr}}$). To calculate λ using the sliding linear regression method, these transitional scenarios require a combination of observed SST, interpolated SST, and RCP8.5 SST (illustrated in A.2.8). An exact temperature projection cannot be made as in Section 4, since N is unknown in this scenario. As an approximation, we use the same $N_{RCP} - F$ as in Section 4 (Figure 2.3a). This assumes that the N_{RCP} from the MPI-GE ensemble-mean and F from our prescribed SST simulation are true currently and over the next 60 years, despite a mismatch between the simulated and observed SST patterns now. This assumption seems reasonable given the similarity between recent global-mean temperature trends in MPI-ESM and observations.

We reiterate that the black dashed line in Figure 2.3e uses $N_{1991-2021} - F_{1991-2021}$, which represents the mean trend of $N - F$ from 1991-2021 extrapolated into the future for this scenario (6 in Supplemental Table 1).

A.2 Figures

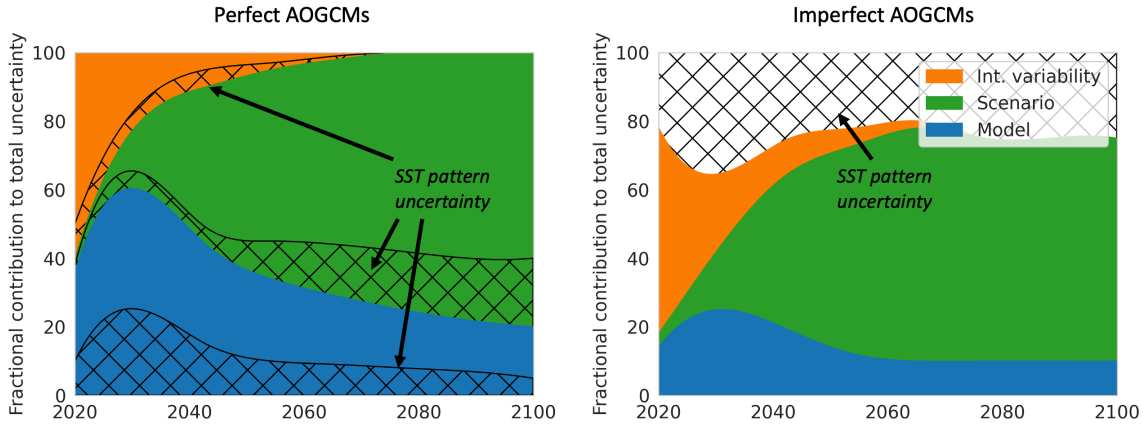

Figure A.2.1. An illustration of the fractional contribution to total model uncertainty of internal variability, forcing scenario, and structural uncertainty based on Hawkins and Sutton (2009). If AOGCMs were able to reproduce the observed SST pattern, *SST pattern uncertainty* would be part of the three classical uncertainties (left). However, because models are unable to reproduce the observed SST pattern, we separate *SST pattern uncertainty* from the other three uncertainties (right), creating a separate uncertainty unaccounted for in projections. The values are random and shown for illustration only as we do not know the magnitude of *SST pattern uncertainty* in the future and across models. In the main text, we make the point that *SST pattern uncertainty* might increase total model uncertainty by 40% by 2085, assuming MPI-ESM is representative of other models.

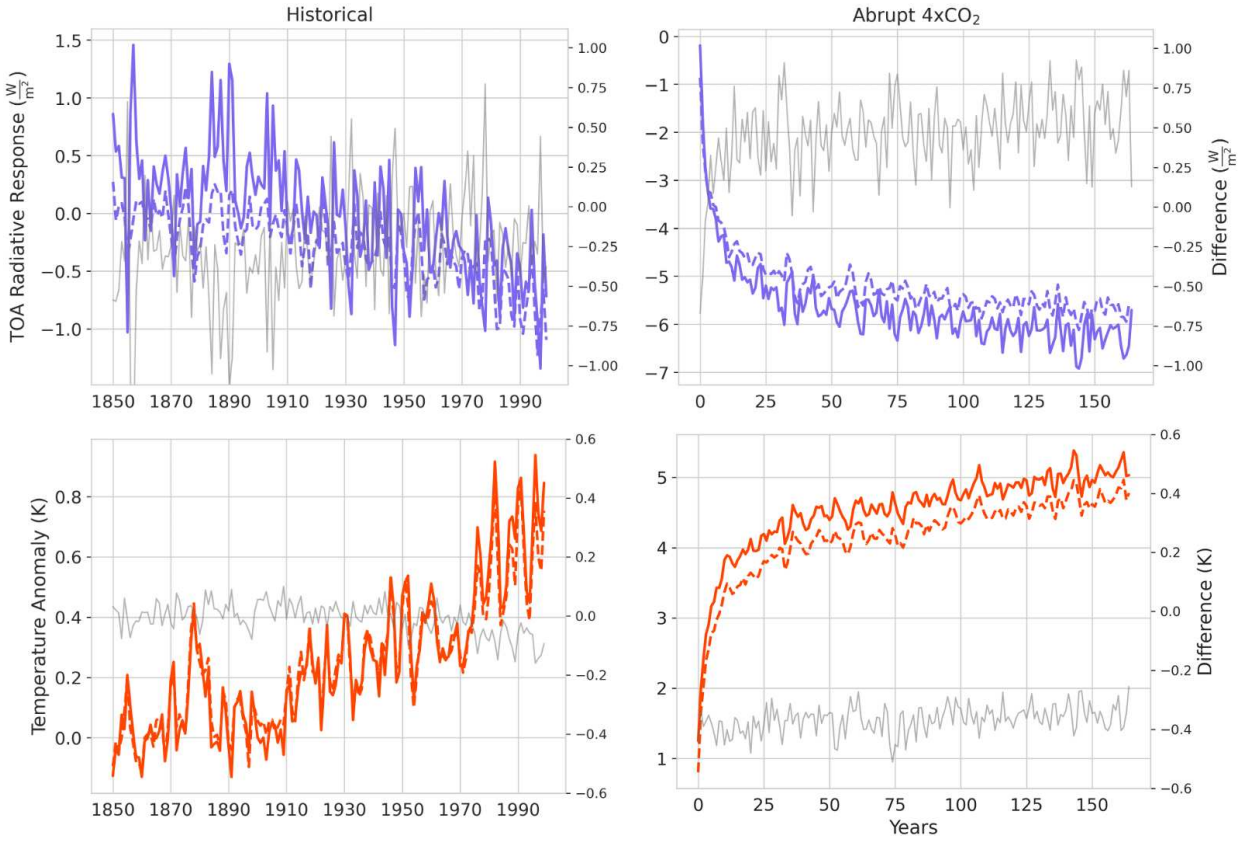

Figure A.2.2. Global-mean radiative response (top) and global-mean temperature response (bottom) output from the coupled MPI-ESM historical simulation (left; solid) and the coupled MPI-ESM abrupt-4xCO_2 simulation (right; solid). The radiative GF convolved with the SST pattern from the same coupled simulations (top; dashed) and the temperature GF convolved with the SST pattern from the same coupled simulations (bottom; dashed). The gray lines denote the difference between the GF response and coupled model output. See Supplemental: Green's function for computing and tuning GF_R and GF_T. The GF approach works well for the historical but has a constant offset in the stronger forced simulations, possibly due to temperature nonlinearity in higher forcing scenarios (Bloch-Johnson et al. 2024). However, interannual variability and the change of T and R are still faithfully represented.

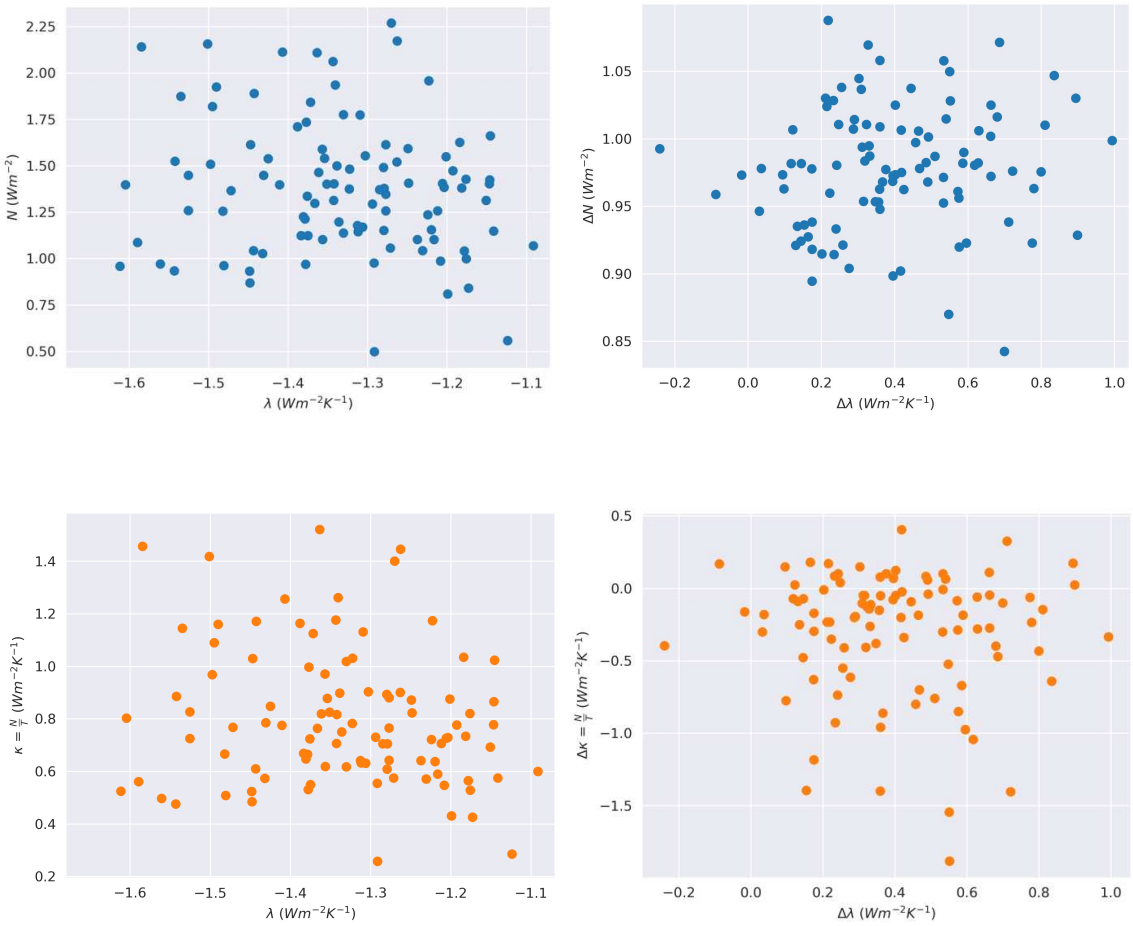

Figure A.2.3. **a**, The global-mean energy imbalance ($N_{RCP8.5}$) versus the global-mean radiative feedback (λ) for each ensemble member in the MPI-GE for the 30 years centered at 2050. **b**, The change in λ and $N_{RCP8.5}$ between 30-year periods centered at 2020 and at 2070 for each ensemble member. **c**, The global-mean ocean heat uptake efficiency (κ) versus λ for each ensemble member for the 30 years centered at 2050. **d**, The change in κ plotted against the change in λ for each ensemble member in the MPI-GE from 2020 to 2070 for each ensemble member in the MPI-GE. The surrounding 30-year average is used to calculate N and ΔT for κ in all plots (e.g., 2005 to 2035 for 2020), and λ is calculated using the surrounding 30-year linear regression of $(N_{RCP} - F_{RCP})$ against ΔT (solely output from the coupled model and not including the GF).

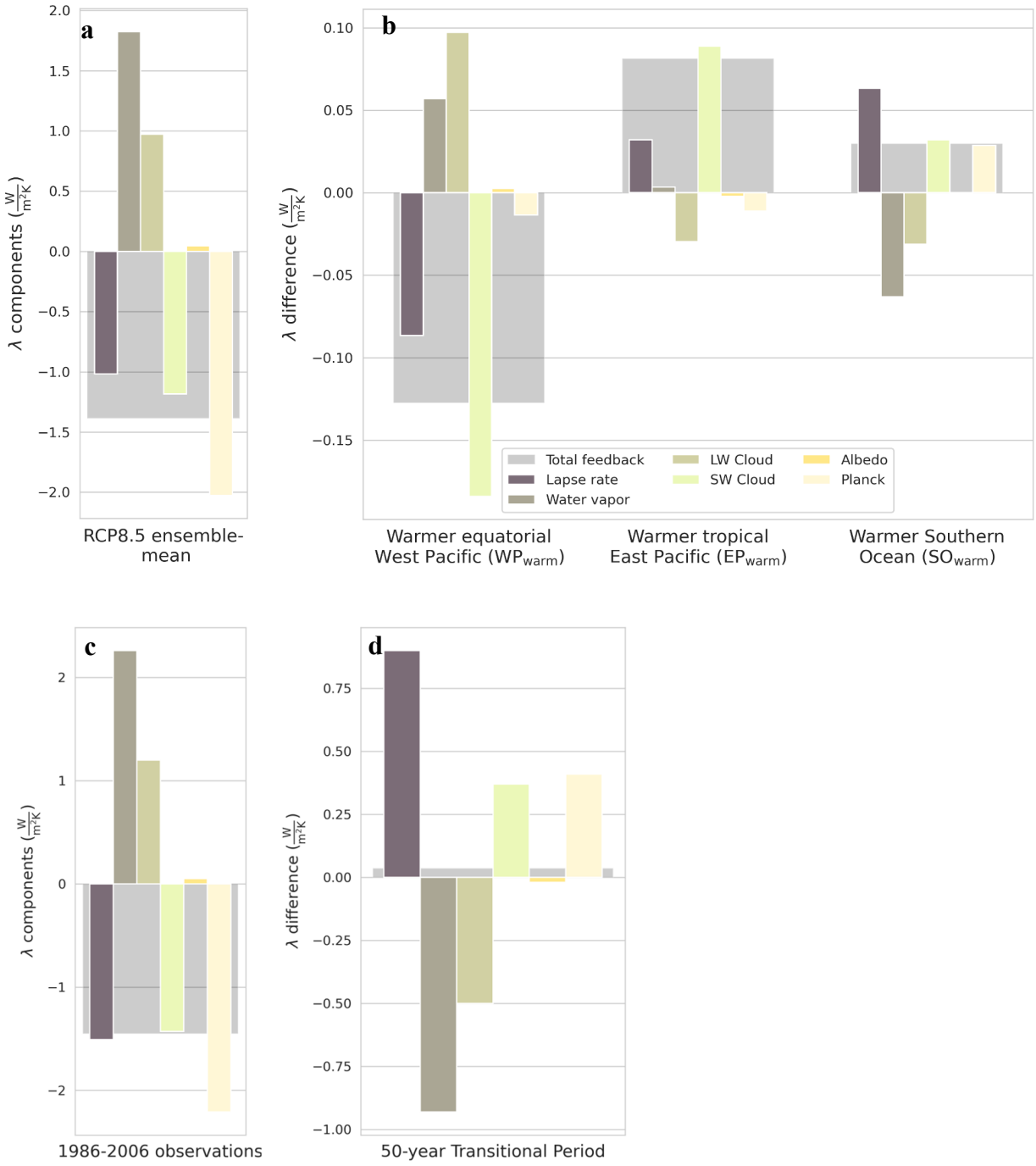

Figure A.2.4. **a**, Decomposition of the MPI-ESM RCP8.5 global- and ensemble-mean radiative feedback for years 2065. **b**, The difference in λ for each feedback for WP_{warm}, EP_{warm}, and SO_{warm} from the RCP8.5 ensemble-mean 2065. Cool scenarios are opposite in λ and their decompositions. **c**, Decomposition of the HadISST observation-based feedback (solid black line in Figure 2.2b) for years 1986-2006. **d**, The difference in λ for each feedback for the 50-year transitional scenario for 2036-2056 from the observational λ decomposition. The net feedback and its change are shaded behind each scenario.

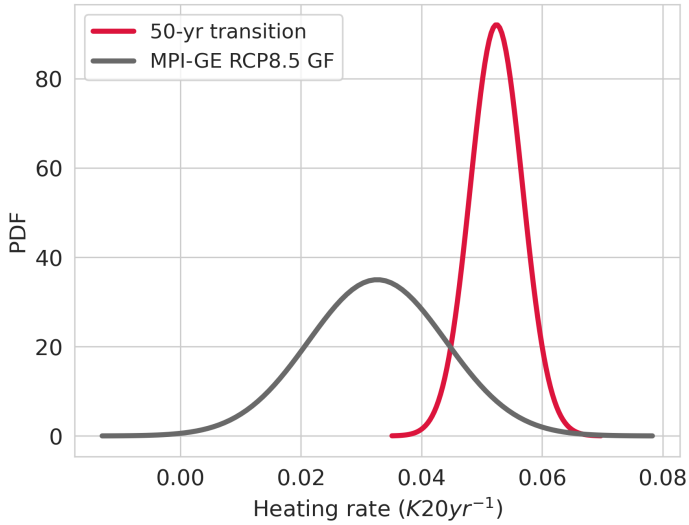

Figure A.2.5. Probability density function (PDF) of heating rates for the MPI-GE RCP8.5 ensemble (gray) and $\text{Transition}_{50\text{yr}}$ (red). The heating rates are calculated using a sliding window of 20-year segments for 2015-2045 for each ensemble member. Each PDF consists of 2,000 data points since there are 20 heating rates for each ensemble member.

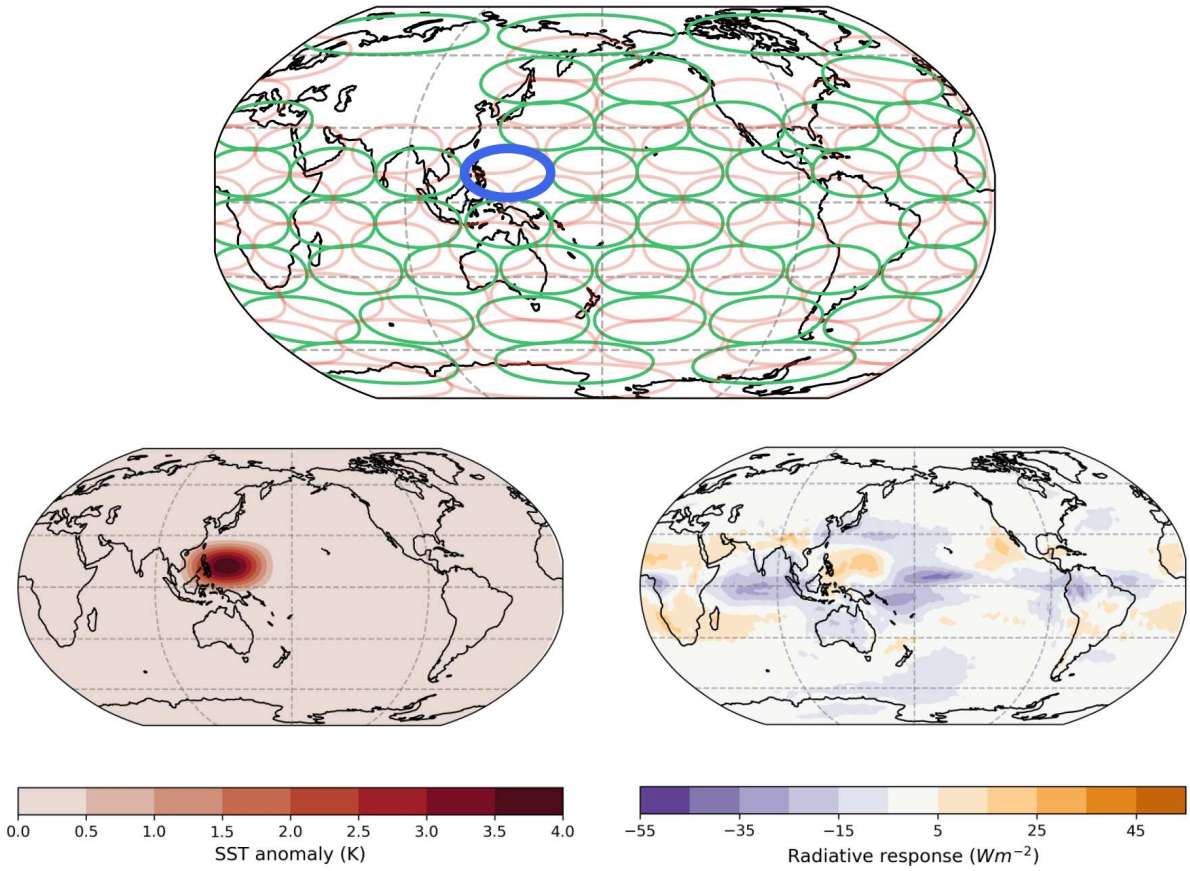

Figure A.2.6. Location of SST patches to create the GF (top). The contour denotes 1 K amplitude of each patch. For illustration, we show the SST forcing for the warm patch east of the Philippines (bottom left; highlighted as blue in the top figure). The radiative response for the same patch (bottom right).

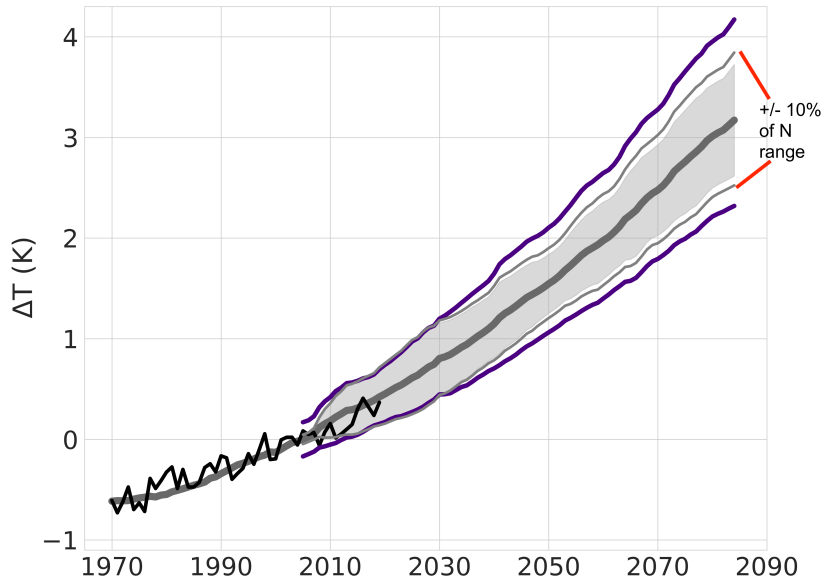

Figure A.2.7. Global-mean surface temperature anomaly (ΔT) from the 2000-2010 average: HADCRUT5 observations (black), MPI-ESM historical (1970-2006) and RCP8.5 projection (2006-2085) ensemble-mean (dark gray), MPI-ESM RCP8.5 ensemble spread (+/- 2σ; gray shading), MPI-ESM RCP8.5 ensemble spread with +/- 10% applied to each ensemble member (region between gray lines), and model spread when WP_{cool} and WP_{warm} are applied to each RCP8.5 ensemble member (region between purple lines). The effect of +/- 10% of N on ΔT is small compared to *SST pattern uncertainty*.

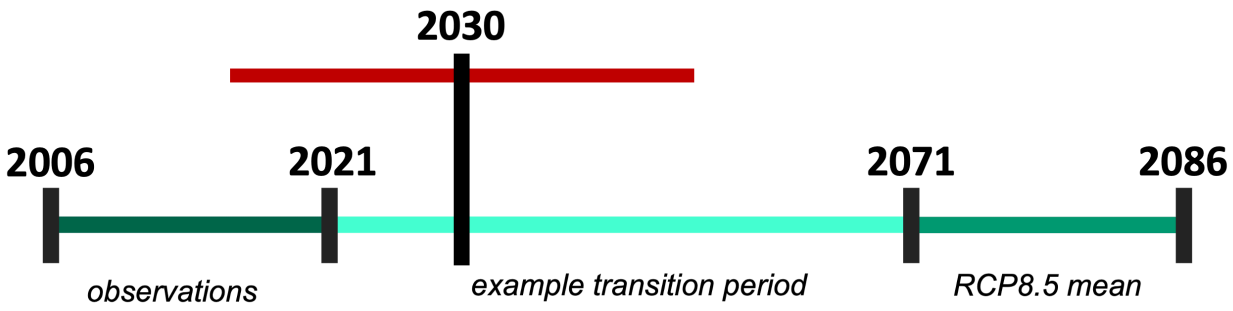

Figure A.2.8. Schematic diagram showing the T and R values required to calculate λ for the 50-year transitional period scenario (Section 3). λ is calculated using a linear regression of T and R of the surrounding 30 years of a given year. For example, if the year is 2030, to calculate λ, T and R would come from 7 years of observations (2015-2022) and 23 years of interpolated SST from observations in 2021 to the RCP8.5 mean in 2071.

A.3 Tables

Table A.3.1. Motivation for each SST pattern scenario generated. The first three scenarios are idealized SST patterns from Section 3, and the last three are realistic SST pattern scenarios from Section 5. Note that the "cooling scenarios" (1-3) still warm in the regions of interest, just at a lower rate than AOGCM RCP8.5 projections. The colors of the regions in the maps (rows 1-3) are the same as in Figure 2.2. The SST trend maps (rows 4-6) use the same color bar. An additional motivation for scenarios 1-3 is that the range of internal variability simulated by AOGCMs may not be realistic, resulting in the erroneous SST trends for these regions (Watanabe et al. 2021, Olonscheck et al. 2020).

Order in text	Scenario	Equal-area dimensions (1-3) and SST trend (4-6)	Motivation
1	Equatorial West Pacific (WP_{warm}/WP_{cool})	18°S to 20°N; 110°E to 156°E 	*Forcing response bias*: the warming trend observed in the convective region of the equatorial West Pacific is greater than the tropical average, which is not replicated in AOGCMs (Fueglistaler and Silvers, 2021).
2	Tropical East Pacific (EP_{warm}/EP_{cool})	28°S to 1°N; 120°W to 71°W 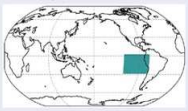	*Mean-state bias*: the ubiquitous cold tongue bias in AOGCMs might prohibit the correct response of the East Pacific SSTs to forcing (Seager et al., 2019). *Forcing response biases*: observed cooling are not captured by AOGCMs (Seager et al., 2019; Seager et al., 2022; Wills et al., 2022). Their cause is debated and may arise due to: (1) the cold tongue mean-state bias (Seager et al., 2019); (2) the lack of an ocean thermostat effect, which causes models to warm the East Pacific despite increased upwelling (Clement et al., 1996; Heede et al., 2020); (3) an incorrect SST response to aerosols over the East Pacific (Heede and Fedorov, 2021); (4) an incorrect simulation of the Southern Ocean, possibly due to missing melt water (Kim et al., 2022; Dong et al., 2022; Kang et al., 2023).
3	Southern Ocean (SO_{warm}/SO_{cool})	58°S to 53°S; 0° to 360° 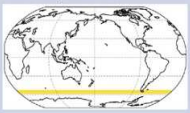	*Mean-state bias*: Observations are cooler in the Southern Ocean than AOGCMs (e.g., Kay et al., 2016; Kajtar et al., 2021). *Forcing response bias*: AOGCMs fail to replicate observed cooling trends, which may be a response to CO_2, aerosol, or freshwater forcing (Kostov et al., 2018; Armour et al., 2016; Dong et al., 2022) or mean-state biases (Kajtar et al., 2021).
4	10-year transition ($Transition_{10yr}$) and 50-year transition ($Transition_{50yr}$)	$Transition_{10yr}$ SST Trend 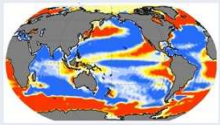 $Transition_{50yr}$ SST Trend 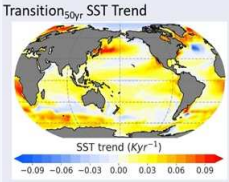	A transition from HadISST in 2021 (2016-2021 average pattern) to the RCP8.5 ensemble-mean in 2031 (2031-2036 average pattern) or 2071 (2071-2076 average pattern). This warms the tropical East Pacific, which is what studies argue may occur (Heede et al., 2020; Park et al., 2022), however the timescale of this warming is unknown, so we suggest a fast warming (10 years) and a slow warming (50 years).
5	50-year transition with 1991-2021 observed trend in EP ($Transition_{50yr\text{-}EPobs}$)	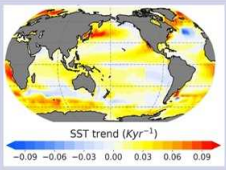	We replace the EP with the 1991-2021 HadISST trend, which is negative (Figure 4f). In this scenario, the tropical East Pacific does not warm as simulated in AOGCMs over the next few decades, and the rest of the world approaches the RCP8.5 ensemble-mean SST. This scenario assumes oceanic heat transport from the extratropics or a reduction in aerosol forcing will not warm the EP anytime soon (Heede et al, 2020; Heede and Fedorov, 2021; Park et al., 2022).
6	1991-2021 observed SST trend for all regions	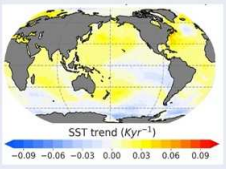	Assuming all AOGCM projections of SST are incorrect, and the observed trend (1991-2021) continues through 2085. We regard this as unlikely because observations show strong variation in SST trend patterns given interannual and inter-decadal variability.

APPENDIX B: SUPPORTING INFORMATION FOR CHAPTER 3

B.1 Text

B.1.1 Green's function

The Green's function was developed following the approach in Zhou et al. (2017) and Dong et al. (2019) and is described in depth in Alessi and Rugenstein (2023). We used the Max Planck Institute's atmospheric model ECHAM v6.3 with a latitude x longitude grid of 96 x 192 (Stevens et al., 2013). A control simulation is first run for 26 years with prescribed 1990-2009 averaged SST from the HadISST observed dataset (Rayner et al., 2003). All radiative forcings (e.g., GHG, aerosols) are held constant at year 2000 levels (Dong et al., 2019). Multiple ECHAM simulations are then run, each with an anomalously warm or cool SST patch, that are initialized from year 6 of the control simulation for 20 years. The SST anomalies follow a cosine hump to avoid unrealistic SST gradients:

$$\delta SST(x,y) = A\cos^2(\frac{\pi}{2}\frac{y-y_p}{y_w})\cos^2(\frac{\pi}{2}\frac{x-x_p}{x_w}),$$

where A is the amplitude of the SST patch anomaly (+/- 4 K) (Zhou et al., 2017), subscript p denotes the center point of the patch, and subscript w denotes the half-width of the patch. y_w is 2150 km and x_w is 4300 km, so that the patches are 8600 km x 4300 km in size. 182 patch simulations were run (91 cool and 91 warm) with constant 1990-2009 averaged sea ice. The setup and example temperature perturbation are shown in Figure B.2.1.

The GF is a large matrix, where each index represents the sensitivity of each SWUS grid point to each SST grid point (see below matrix). For example, one index in the GF is the sensitivity of precipitation over the Los Angeles grid box to SST changes over the Gulf of Mexico grid box to the west of Florida. The rest of this column in the GF matrix represents the sensitivity of Los Angeles precipitation to each SST grid box across the planet.

$$\begin{bmatrix} \frac{\partial P_1}{\partial SST_1} & \cdots & \frac{\partial P_j}{\partial SST_1} \\ \vdots & \ddots & \vdots \\ \frac{\partial P_1}{\partial SST_n} & \cdots & \frac{\partial P_j}{\partial SST_n} \end{bmatrix}$$

B.1.2 Tuning the Green's function

The original SWUS precipitation Green's function (GF_P; Figure B.2.2, first column) was slightly adjusted to better represent the SWUS precipitation response to a given SST pattern compared to coupled model output. Since the untuned GF_P increased SWUS precipitation too much given a positive SST change, we subtracted a very small value ($8.6x10^{-5}$) from each index of GF_P. We validated our method by comparing the GF_P precipitation response to the MPI-GE precipitation output, which have a correlation of 0.947 after tuning (Figure 3.2b). Before tuning, the correlation was -0.846 (Figure B.2.2). The small value that was removed from each index of the GF matrix ($8.6x10^{-5}$) was selected based on its strong replication of the AO-GCM precipitation output, as well as its SST sensitivity pattern retaining the same sensitivities as the untuned GF_P (green in Central Pacific and brown in the Caribbean). The untuned GF_P is likely too sensitive in the Central Pacific due to nonlinearities that exist in the climate system that the GF, which is a linear approximation between a forcing (SST) and a climate response (precipitation), cannot capture (Williams et al., 2023). For example, because the GF is developed from individual anomalous SST patch simulations, it does not consider the effect of multiple anomalous SST patch perturbations occurring simultaneously (similar to a tropical mean warming in the real world). Williams et al. (2023) demonstrate that an anomalously warm patch perturbation in the Central Pacific increases the tropical free tropospheric stability, which then increases the convective initiation threshold, resulting in a decrease in convection in other regions in the Tropics due to the higher convective threshold over the Central Pacific. Since the untuned GF_P is

created from individual patch perturbations, it does not consider this changing convective initiation for SST warming. GF_P then significantly exaggerates convection in the Central Pacific, which then overstates the SWUS precipitation response due to the Central Pacific initiation affecting the midlatitude Rossby wave. We argue that the tuning of the GF_P makes the GF more realistic in its portrayal of a nonlinear system, while retaining the features of the original untuned GF. We trust the feature of SWUS precipitation being most sensitive to the Central Pacific based on decades of literature, which are mostly based on single patch simulations (Hoerling et al. 1997; Hoerling and Kumar, 2002). Hence, we trust the location but not the magnitude and exact spatial extent of the sensitivity. The real world's sensitivity might look different in magnitude and spatial extent depending on deep convection and its sensitivity to SST and SST gradients, which is somewhat but not perfectly understood (Johnson and Xie, 2010; Williams et al., 2023).

We tested other methods of tuning that would decrease SWUS precipitation sensitivity to SST change, including removing large positive values and small positive values. Removing large positive values (Figure B.2.2, middle column) completely removed the sensitivity of SWUS precipitation to the Central Pacific. We know this response to be incorrect given the well-established teleconnection between the two regions (Redmond and Koch, 1991; Dettinger et al., 1998) and previous precipitation GF studies (Barsugli and Sardeshmukh, 2002; Zhang et al., 2023). In other words, while GF_P can replicate some of the precipitation response (bottom row; middle), it is not realistic nor physically meaningful in its teleconnections (top row; middle). Removing small positive values, as done for radiation in Alessi and Rugenstein (2023) and similar to Dong et al. (2019), produced a similar map to the untuned and tuned version used in this study, with a high correlation between GF_P precipitaton response and MPI-GE precipitation output of 0.927. However, year-to-year SWUS precipitation sensitivity to the pattern of SST is

noticeably diminished (compare Figure B.2.2, right to Figure 3.2b). We tested other methods including multiplying (increasing the sensitivity of large-magnitude regions, e.g., the Central Pacific and Caribbean) and dividing (decreasing the sensitivity of large-magnitude regions) each index in GF_P but could not replicate the MPI-GE precipitation output. We settled on the method of subtracting a small value from each index because it retains the broad location of the original pattern of SST and replicated the coupled model precipitation output the best.

B.1.3 Regional SST adjustment

We generate a warm and cool scenario for the equatorial Central Pacific (16°S to 16°N, 175°E to 140°W), tropical East Pacific (28°S to 1°N, 120°W to 71°W), and Caribbean (0°N to 30°N, 107°W to 40°W). All six scenarios have equal area forcings, so that the scenarios are comparable to each other. Note that the East Pacific patch was selected based on the marine stratocumulus cloud deck location.

We apply an SST anomaly adjustment to each ensemble member's SST pattern in these regions based on 3% of the global-mean SST anomaly (~0.01 K, see Figure B.2.5) for any given year from pre-industrial control (1850-1870). Thus, a "cool" scenario is somewhat colder than the RCP reference but still warming with respect to present day values. We selected a perturbation of 3% based on realistic SST fluctuations due to historical SST pattern uncertainty in these regions. The order of magnitude of the adjusted SST, 1.1 K at each grid point when the anomaly is concentrated in the region of interest by 2085, is comparable to model error in the tropical East Pacific (Figure 1 in Seager et al., 2019) and Southern Ocean (Figure 2 in Wills et al., 2022) and slightly greater than the difference between AOGCMs and observations in the equatorial West Pacific (Figure 2 in Wills et al., 2022; Figure 5 in Fueglistaler and Silvers, 2021). To keep the global-mean SST constant, we redistribute the warming or cooling to the rest

of the planet (on the order of 0.01K by 2085), again for each ensemble member. This adjustment has almost no impact on changing the final ΔT result (on the order of 0.01K), which we tested by running the same simulations with only a change in SST in the region of interest (with no redistribution of SST).

B.1.4 Regional SST adjustment

The 10-year and 50-year transition scenarios in Section 3.2 involve interpolating the SST at each grid point from the HadISST 2016-2021 average to the MPI-GE RCP8.5 in 2031-2036 or 2071-2076 average, respectively, for each ensemble member. The lines plotted represent the SST pattern for that year (interpolated) convolved with GF_P averaged over all MPI-GE ensemble members.

B.2 Figures

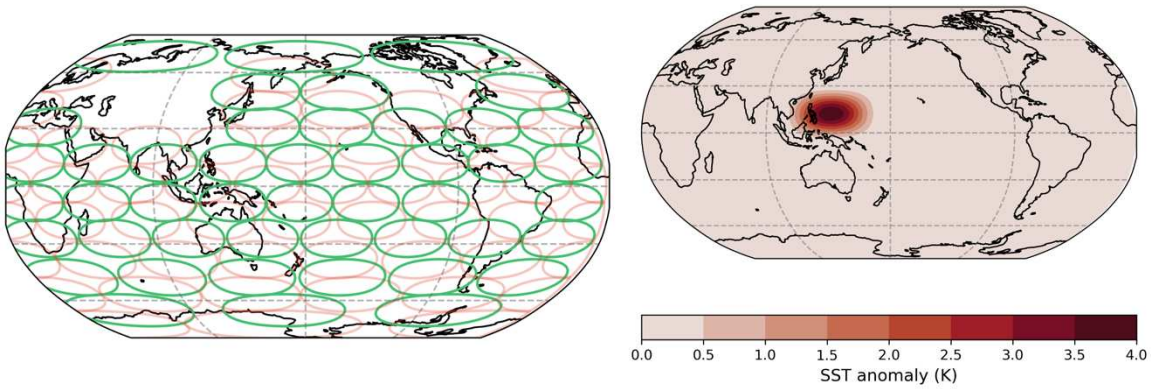

Figure B.2.1. Location of SST patches to create the GF (left). The contour denotes 1 K amplitude of each patch. For illustration, we show the SST forcing for the warm patch east of the Philippines (right).

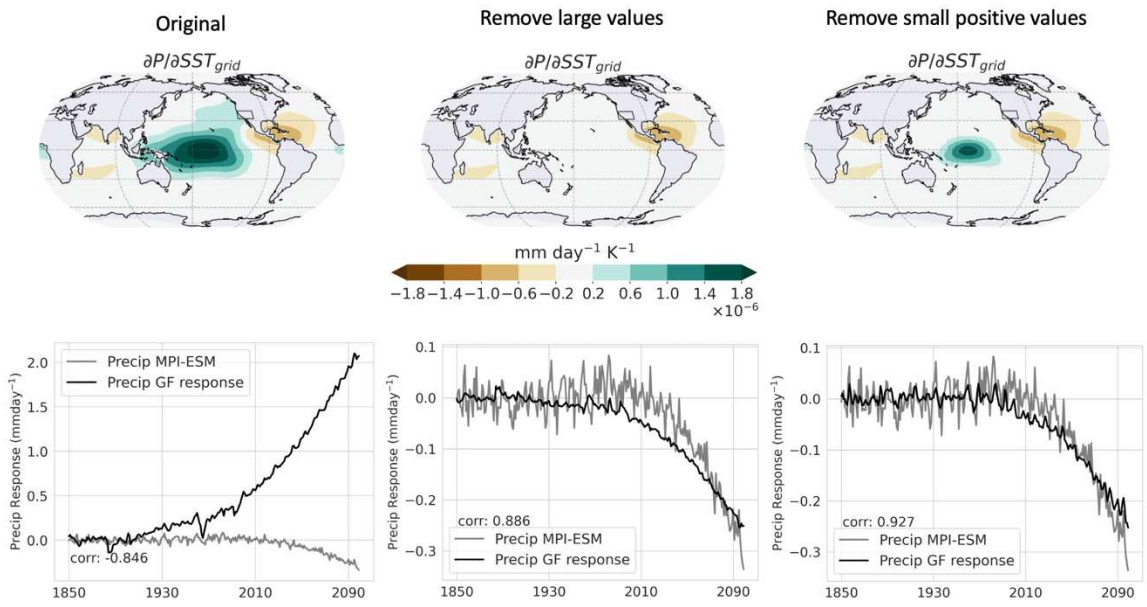

Figure B.2.2. Annual-mean SWUS precipitation response per unit SST warming in each grid box (top). The SWUS precipitation response of the Green's function convolved with the MPI-ESM Grand Ensemble-mean SST pattern, and the SWUS precipitation output from the MPI-ESM Grand Ensemble is also shown (bottom). The original precipitation GF (untuned) is in the first column, GFP with values greater than the 92nd percentile removed is in the second column, and GFP with small positive values removed (< 0.00085) is in the third column.

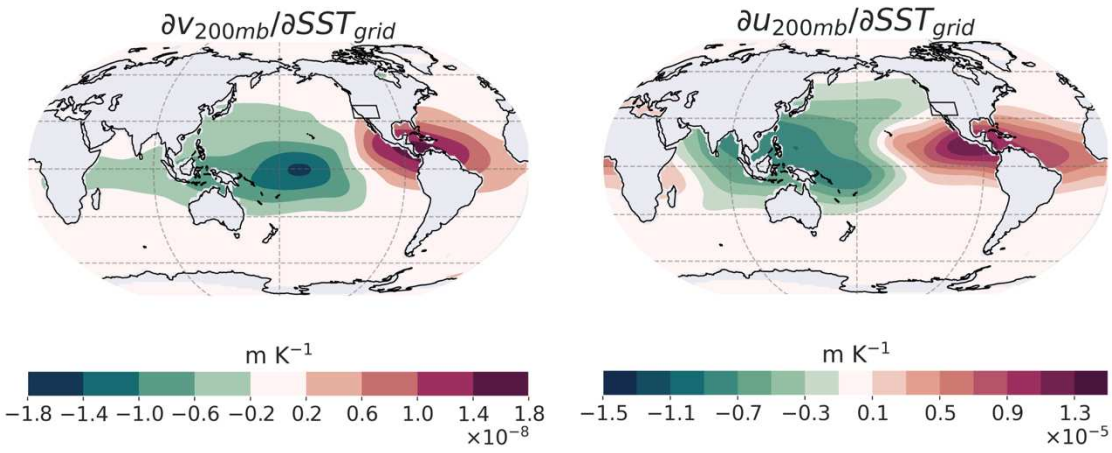

Figure B.2.3. The annual-mean SWUS 200 mb v-wind (left) and 200 mb u-wind (right) response per unit SST warming in each grid box.

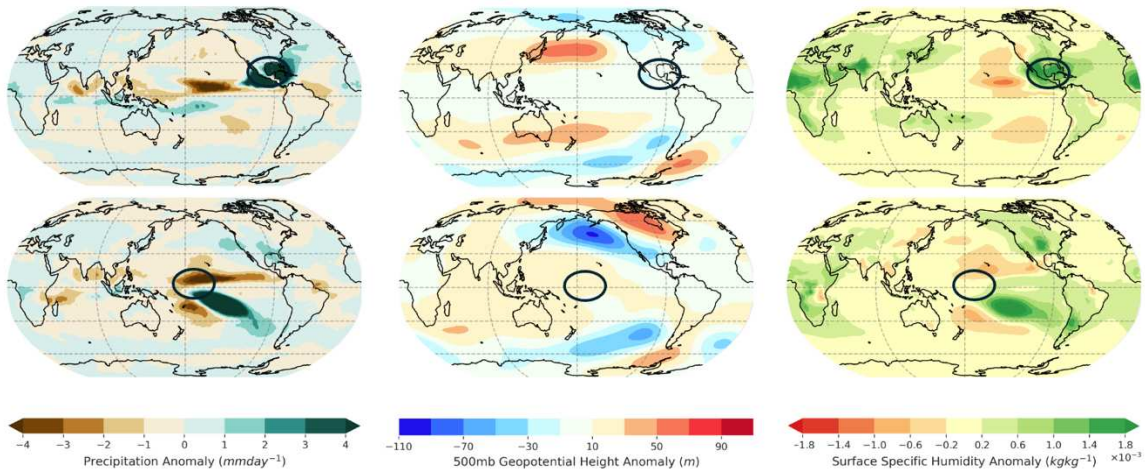

Figure B.2.4. The precipitation (left), 500 mb geopotential height (center), and specific humidity (right) response to a warm patch experiment in the Caribbean (top) and the Central Pacific (bottom). The black circles represent the location of the localized SST patch perturbations (Central Pacific for bottom row and Caribbean for top row).

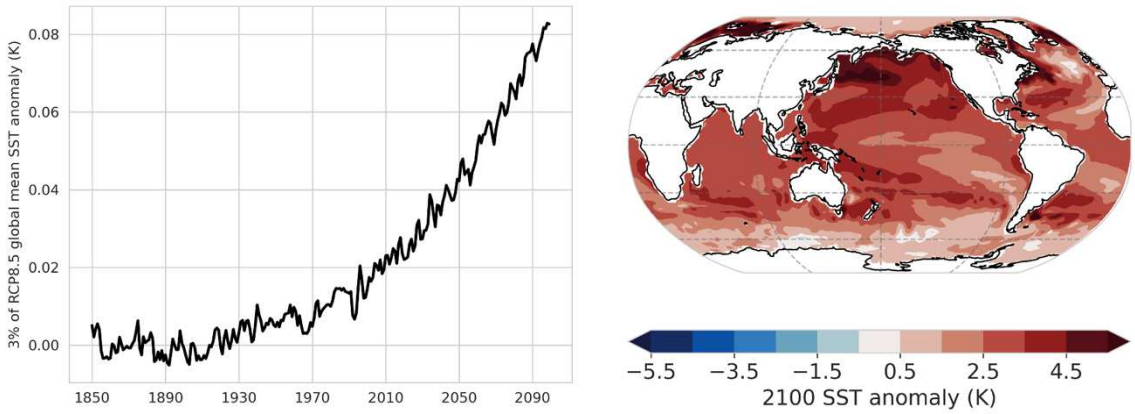

Figure B.2.5. Timeseries of the global-mean SST anomaly between RCP8.5 and pre-industrial (1850-1870 average) (left). Map of the SST anomaly in year 2100 (right).

APPENDIX C: SUPPORTING INFORMATION FOR CHAPTER 4

C.1 Figures

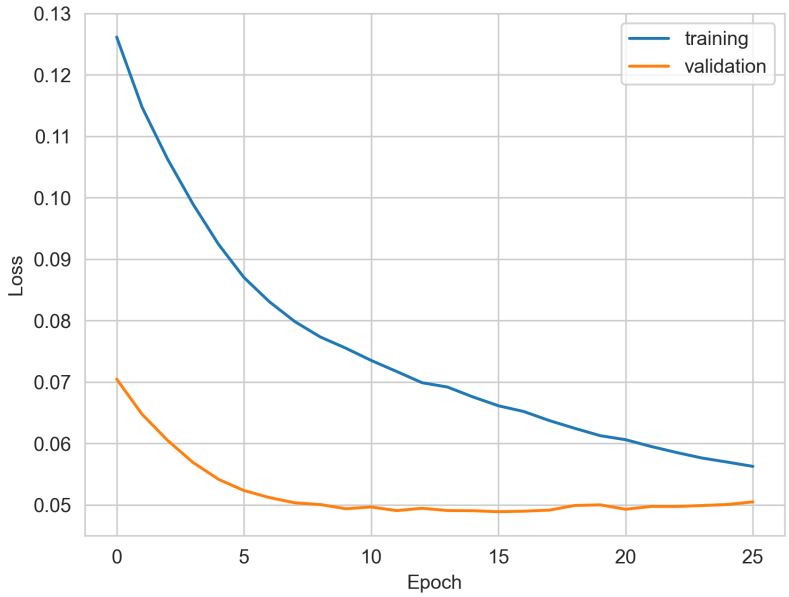

Figure C.1.1. The loss curve (mean absolute error) for training and validating the CNN model.